Abstract

Title of Dissertation: Observing and Controlling Chaotic Systems
and Wave Chaos Statistics

Paul Tze-Man So, Doctor of Philosophy, 2005

Dissertation directed by: Professor Edward Ott
Department of Physics

In chapter two, a method is proposed whereby the full state vector of a chaotic system can be reconstructed and tracked using only the time series of a single observed scalar. Assuming that an accurate mathematical description of the system is available, this nonlinear observer is able to successfully track chaotic orbits in spite of noise and periodic perturbations. Then in chapter three, using time delay coordinates and assuming *no a priori* knowledge of the dynamical system, we introduce a method which stabilizes a desired periodic orbit embedded in a chaotic attractor. Similar to the original control algorithm introduced by Ott, Grebogi, and Yorke [*Phys. Rev. Lett.* **64** (1990)], the stabilization is done via small time dependent perturbations of an accessible control parameter. Both the nonlinear observer and the control method are numerically illustrated using both the Ikeda map, which describes the dynamics of a nonlinear laser cavity and the double rotor map which describes a periodically kicked dissipative mechanical system.

Lastly, in chapter four, we examine the quantum manifestations of classically chaotic systems. In particular, we are interested in the universal short wavelength behaviors of quantum systems in relation to the classical solutions of Hamiltonians in the same symmetry class. It has been predicted that in the semi-classical regime, the level statistic of a classically chaotic

system corresponds to that of the Gaussian Unitary Ensemble (GUE) of random matrices when time reversal symmetry is broken. The system employed in our experiment is a microwave cavity containing a thin ferrite strip adjacent to one of the walls. When a sufficiently large magnetic field is applied to the ferrite (thus breaking the time-reversal symmetry) good agreement with GUE statistics is obtained. The transition from GOE (which applies in the absence of the applied field) to GUE is also investigated.

Observing and Controlling Chaotic Systems and Wave Chaos Statistics

by

Paul Tze-Man So

Dissertation submitted to the Faculty of the Graduate School
of the University of Maryland in partial fulfillment
of the requirements for the degree of
Doctor of Philosophy
2005

Advisory Committee:

Professor Edward Ott, Chairman/Advisor
Professor Steven M. Anlage
Professor Celso Grebogi
Professor Thomas M. Antonsen
Professor W. P. Dayawansa

Dedication

To my parents:

Mr. Yuen Sang So

and

Mrs. Yu Yuen Kit So

Acknowledgements

I am deeply indebted to Prof. Ott for his guidance during my years as his PhD. student. As my teacher, he was patient and as my advisor, he was inspirational and insightful. His directness and clarity in scientific persuits will continue to be my guide throughout my professional career.

I would also like to thank Prof. Anlage for helping me to understand and to appreciate the experimental aspects of my research. Furthermore, I thank Prof. Grebogi, Prof. Dayawansa, and Prof. Antonsen for their numerous helpful suggestions during the course of my research.

Moreover, my deepest gratitude goes to Dr. Mattos and Mary Murphy Mattos for their encouragement in a time when I still felt uncertain in this new land of opportunity.

And, last but not least, I thank my brother for his understanding and all the help which he has given me all through the years. I can count on the fact that he will always be his brother's keeper.

Wait! How can I forget the friendship and help from my colleagues and friends: Allan, Anna, Barbara, Chagarn, Charles, Ditza, Ernie, Leo, Leon, Max, Pat, and Robb.

Contents

List of Tables

List of Figures

Observing and Controlling Chaotic Systems
and Wave Chaos Statistics

Paul Tze-Man So

March 19, 2005

Just do it!
check for bib numbers, fig numbers, equation numbers
and move some bib into footnotes

This comment page is not part of the dissertation.

Typeset by LaTeX using the `dissertation` style by Pablo A. Straub, University of Maryland.

Chapter 1

Introduction

The secrets of the hoary Deep–a dark
Illimitable ocean, without bound,
Without dimension; where length, breadth, and height,
And time, and place, are lost; where eldest Night
And Chaos, ancestors of Nature, hold
Eternal anarchy, amidst the noise...
John Milton - *Paradise Lost*

The study of chaos has matured to a new stage. Both theoretical and experimental researchers have come to accept that systems ranging from a simple periodically forced pendulum to complex systems such as turbulence in a fluid system possess exponential sensitivity to initial conditions. However, most importantly, we realize that this "deterministic randomness" from chaotic systems is not always uninviting, but it might actually be desirable. A large body of work has been accumulated in the endeavor to apply what we have learned from chaos theory to the utilization of experimental chaotic data[1]. With their broad application to the analysis of time series from physical, biological, and economic systems, techniques in predicting chaotic time series and methods of noise reduction using knowledge of the local linear dynamics have gained considerable attention. At the same time, with encouragement from successful physical experiments, control techniques utilizing the sensitive dependence of chaotic systems have been shown to be more flexible than conventional schemes. In addition, the ability to

[1] A comprehensive collection of these results can be found in the book by Ott, *et al.*[1]

manipulate chaotic signals also opens the door for synchronism among chaotic systems and the possible usage of chaotic signals for secure communication. The results presented in this thesis represent my contributions to this growing body of work.

In the following chapter, I first introduce a new technique to track and to reconstruct the full state of a chaotic system from the time series of an observed scalar. As a simple example, consider a mechanical system with interconnected gears, levers, springs, etc. that is behaving chaotically on an attractor of finite dimension. Can one deduce the positions of all the parts of the system from the time series of the position of just one of the levers? This tracking technique is commonly referred to as an observer. In linear control theory, a reconstructed system state is directly feedback to the system with an appropriate gain matrix so as to steer the system toward a desired equilibrium state. Thus, the nonlinear observer developed here is a logical first step in designing a nonlinear direct-feedback control scheme for chaotic systems. Furthermore, from a different point of view, one can consider the nonlinear observer and the actual chaotic system as a pair of driven-response system. In this perspective, the nonlinear observer technique can then be viewed as a *tunable* synchronizer between two chaotic systems.

Then, our discussion shifts to the development of a parametric control method using time delay coordinates. Unlike direct-feedback control schemes which require a knowledge of the full system state, our parameteric control method affects the chaotic system through an accessible system parameter such as the kicking strength of a periodically kicked pendulum. We wish to make only small controlling perturbations to the system. We do not envision creating new orbits with very different properties from the already existing orbits. Thus we seek to exploit the already existing unstable periodic orbits that are embedded in the chaotic attractor. The use of time delay coordinates in a higher dimensional control scheme introduces additional features which are lacking in the original control technique proposed by Ott *et al.*[11] In the presence of parametric variations, delay coordinate embedding leads to a map which in general depends on a history of past parametric variations as well as the current parameter value. As noted by Dressler and Nitsche[12], these dependencies on past parametric variations if not taken into consideration will lead to an instability of the control scheme.

The last topic of my thesis deals with the following question: what are the quantum manifestations of a classically chaotic system in the situation when time reversal symmetry is

absent. In particular, we are interested in the spectral statistics of classical chaotic systems without time reversal symmetry in the semi-classical limit. It has been conjectured that in the semi-classical regime, the spectral statistics of classically chaotic systems without time reversal symmetry follows the "Gaussian Unitary Ensemble" (GUE) while the spectral statistics of classically chaotic systems with time reversal symmetry follows the "Gaussian Orthogonal Ensemble" (GOE). Experimental results showing the GUE statistics in the time irreversible case are presented using a two dimensional microwave cavity with magnetized ferrite. Since this formalism applies to a general wave equation as well as to the Schrödinger equation, an understanding of these universal short wavelength behaviors might help to further our understanding in other wave systems such as scattering problems in solid state devices, the design of mesoscopic systems, acoustic systems, and electromagnetic wave in cavities and waveguides.

Not chaos-like together crush'd and bruis'd
But, as the world, harmoniously confused:
Where order in variety we see,
And where, tho'all things differ, all agree.

Alexander Pope - *Windsor Forest*

Chapter 2

Observing Chaotic Systems

2.1 Introduction

Consider the situation where there is some experimental system behaving chaotically, and one is able to accurately observe a single scalar measure of the system state. Formally, the system state is given by some vector $\mathbf{X}$ which is a function of time. The observed scalar can be expressed as some function of the system state, $O = g(\mathbf{X})$. The question we ask is the following: Assuming that an accurate mathematical description of the system is available, how can we deduce the system state $\mathbf{X}$ from measurements of O?

One way of addressing this general problem is via the delay coordinate embedding technique. Takens [2] shows that, generically, a delay coordinate vector $(O_n, O_{n-1}, ..., O_{n-(N-1)})$ of sufficiently large N uniquely determines the system state $\mathbf{X}_n$. Thus, by using a computer to solve the known mathematical description of the system (assumed here to be a discrete time system), one can build up a mapping at each point on the attractor from an N-dimensional delay coordinate vector $(O_n, O_{n-1}, ..., O_{n-(N-1)})$ to the system state, $\mathbf{X}_n$ at time n. This procedure could require the generation, storing and searching of a large amount of data. Another way to address this problem is by utilizing the so called "extended Kalman filter," [3] which is a generalization to nonlinear systems of the usual linear Kalman filter for linear systems (see Sec. 2.6). By taking the statistics of noise into consideration, it can be shown that the Kalman Filter for a *linear* system is optimal in the sense that the error variance between the actual state and the estimated state is minimal. However, since the implementation of the extended Kalman filter requires, at each iterate, the manipulation of matrix equations which

have the same dimension as the full dynamical system, the calculation can get quite cumbersome when the dimension of the system is large. In addition, when the Kalman filter is extended to a nonlinear system, the sense in which this method is optimal becomes unclear (c.f. Sec. 2.6)[1]. Thus, while the embedding method and the extended Kalman filter may be useful for the purpose we address, they have drawbacks that motivate us to investigate other approaches[2]. Here, we propose a tracking technique for relatively high dimensional chaotic systems but with low dimensional attractors. The stability of our technique to the addition of small noise will also be investigated. Unlike the Kalman filter, which requires manipulation of matrix equations whose dimension is the full dimensionality of the system, the number of calculations in our method is of the order of the number of expanding directions, which may be much smaller than the system dimensionality.

The organization of this chapter is as follows. In Sec. 2.2, we will briefly review the construction of a linear observer in the standard feedback scheme. This provides the conceptual foundation for our nonlinear observer developed in Sec. 2.3. In Sec. 2.3, we derive the full-order observer for chaotic systems (full-order observer estimates all components of the state vector from a given scalar time-series). In Sec. 2.4, we introduce the kicked double rotor map example and use it to examine the characteristic convergence time and the basin of attraction for a single observer. Then, in Sec. 2.5, we will introduce the reduced-order observer for chaotic systems. As its name suggests, the reduced-order observer is a more efficient special case of the full-order observer. We also apply this reduced-order observer to the kicked double rotor map example to demonstrate the effect of the addition of noise to the system and/or to the output function. Next, Sec. 2.6 will compare the performance of the extended Kalman filter with our nonlinear observer technique. Section 2.7 will provide a summary of our chaotic observer technique and a discussion of its advantages and drawbacks. The appendix in Sec. 2.8 provides some generalizations of the discussion in this chapter. Finally, we note that, since we wish this chapter to be understandable to researchers in chaotic dynamics, we have not

[1] We will initially be interested in noiseless situations, and it should be noted that the Kalman filter procedure also applies in these situations.

[2] Another common situation arises when the system is acted upon by external time-dependent inputs β_n. In that case, one seeks $\mathbf{X}_n$ given knowledge of β_n and O_n. Now, the embedding technique becomes inapplicable, but the alternative which we shall discuss still applies.

assumed prior knowledge of control theory or signal processing. The reader possessing such knowledge should skip the background material (e.g. Sec. 2.2) provided in these fields.

2.2 Linear Observers

In linear control theory, it is possible to estimate unmeasured state variables using a "state observer". To be specific, consider a linear time independent d-dimensional system,

$$\begin{aligned} \mathbf{X}_{n+1} &= \mathbf{A}\mathbf{X}_n, \\ O_n &= \mathbf{G}\mathbf{X}_n, \end{aligned} \tag{2.1}$$

where $\mathbf{X}$ is a d-dimensional column vector, $\mathbf{A}$ is a constant $d \times d$ matrix, and $\mathbf{G}$ is a constant d dimensional row vector. The scalar function O_n is the observed physical output of the system. This system is observable at time n if it is possible to determine the system state $\mathbf{X}_n$ from the observation of outputs over a finite time interval. From a series of d measurements, $(O_n, \cdots, O_{n+(d+1)})$, one can determine all the d components of the state vector $\mathbf{X}_n$ by solving the following matrix equation,

$$\begin{bmatrix} O_n \\ \vdots \\ O_{n+(d-1)} \end{bmatrix} = \mathbf{J} \begin{bmatrix} X_n^1 \\ \vdots \\ X_n^d \end{bmatrix},$$

where

$$\mathbf{J} = \begin{bmatrix} \mathbf{G} \\ \mathbf{GA} \\ \vdots \\ \mathbf{GA}^{n-1} \end{bmatrix}.$$

This equation has an unique solution if and only if the observability matrix $\mathbf{J}$ is of rank d. This is the observability condition introduced by Kalman for a linear time invariant system. Assuming the system to be observable, then one can reconstruct the actual state $\mathbf{X}_n$ of the system from a time series of the scalar output O_n using a state observer, defined by

$$\begin{aligned} \hat{\mathbf{X}}_{n+1} &= \mathbf{A}\hat{\mathbf{X}}_n + \mathbf{C}[O_{n+1} - \hat{O}_{n+1}], \\ \hat{O}_{n+1} &= \mathbf{GA}\hat{\mathbf{X}}_n. \end{aligned} \tag{2.2}$$

The idea of this technique is to choose the control vector $\mathbf{C}$ such that the numerically generated state $\hat{\mathbf{X}}_n$ will converge to the actual state $\mathbf{X}_n$ with increasing n. To derive the necessary condition for this to happen, one can look at the dynamics of the error equation,

$$\mathbf{X}_{n+1} - \hat{\mathbf{X}}_{n+1} = [\mathbf{A} - \mathbf{CGA}](\mathbf{X}_n - \hat{\mathbf{X}}_n), \tag{2.3}$$

obtained by subtracting Eq. (2.2) form Eq. (2.1). If the control vector $\mathbf{C}$ can be chosen so that the magnitudes of the eigenvalues of $[\mathbf{A} - \mathbf{CGA}]$ are all less than one, then the error will exponentially decrease to zero as n approaches infinity. A standard technique exists for choosing the control vector $\mathbf{C}$ to do this, and can be found in many control theory textbooks (e.g., see Ref.[4]).

2.3 Chaotic Observers - Full Order

The general procedure for our chaotic observer technique is similar in spirit to the design of an observer in *linear* control theory. Conceptually, the observer is built upon a numerical copy of the actual system but with an additional time dependent correction term which compares the actual output of the chaotic system and the estimated output of the observer. Depending on the difference between the actual and the estimated output, the time dependent parameters in the correction term are adjusted so that the difference will exponentially decay to zero with time (Kalman filters also have this structure; see Sec. 2.6). In this section, we shall present a general procedure for doing this in the case of *nonlinear chaotic* systems.

We assume that the chaotic system that we want to observe is given by the following equations:

$$\begin{aligned} \mathbf{X}_{n+1} &= \mathbf{M}(\mathbf{X}_n), \\ O_n &= g(\mathbf{X}_n). \end{aligned} \tag{2.4}$$

Here $\mathbf{M}$ and g are nonlinear functions of the d-dimensional vector $\mathbf{X}_n$. The corresponding state observer is taken to be

$$\hat{\mathbf{X}}_{n+1} = \mathbf{M}(\hat{\mathbf{X}}_n) + \mathbf{X}_n[O_{n+1} - \hat{O}_{n+1}], \tag{2.5}$$

where $\hat{O}_{n+1} = g(\mathbf{M}(\hat{\mathbf{X}}_n))$ and $\mathbf{C}_n$ is a time dependent d-dimensional control column vector which we need to adjust at each iterate. Subtracting the equations for $\mathbf{X}_{n+1}$ and $\hat{\mathbf{X}}_{n+1}$ yield

the error equation,

$$\mathbf{X}_{n+1} - \hat{\mathbf{X}}_{n+1} = \mathbf{M}(\mathbf{X}_n) - \mathbf{M}(\hat{\mathbf{X}}_n) - \mathbf{C}_n[g(\mathbf{M}(\mathbf{X}_n)) - g(\mathbf{M}(\hat{\mathbf{X}}_n))]. \tag{2.6}$$

Linearizing about $\hat{\mathbf{X}}_n$ gives

$$\delta\mathbf{X}_{n+1} = [\mathbf{DM}(\hat{\mathbf{X}}_n) - \mathbf{C}_n\mathbf{D}g(\mathbf{M}(\hat{\mathbf{X}}_n))\mathbf{DM}(\hat{\mathbf{X}}_n)]\delta\mathbf{X}_n, \tag{2.7}$$

where $\delta\mathbf{X}_n = \mathbf{X}_n - \hat{\mathbf{X}}_n$ is a differential, and $\mathbf{DM}(\hat{\mathbf{X}}_n)$ and $\mathbf{D}g(\mathbf{M}(\hat{\mathbf{X}}_n))$ are the derivatives of $\mathbf{M}(\hat{\mathbf{X}}_n)$ and $g(\mathbf{M}(\hat{\mathbf{X}}_n))$, respectively, with $\mathbf{DM}$ a d by d matrix and $\mathbf{D}g$ a d-dimensional row vector. Looking back at our discussion of observers for linear time independent systems, the matrix $[\mathbf{A} - \mathbf{CGA}]$ was a constant, and the long term evolution of the observer error is determined by $[\mathbf{A}-\mathbf{CGA}]^n$. This converges to zero with increasing n if the eigenvalues of $[\mathbf{A}-\mathbf{CGA}]$ have magnitudes less than one. In the chaotic case, however, the long term behavior of the error is governed by the product of matrices of the form $[\mathbf{DM}(\hat{\mathbf{X}}_n) - \mathbf{C}_n\mathbf{D}g(\mathbf{M}(\hat{\mathbf{X}}_n))\mathbf{DM}(\hat{\mathbf{X}}_n)]$ which change at each iterate,

$$\delta\mathbf{X}_{n+1} = \prod_{m=0}^{n} [\mathbf{DM}(\hat{\mathbf{X}}_m) - [\mathbf{C}_m\mathbf{D}g(\mathbf{M}(\hat{\mathbf{X}}_m))\mathbf{DM}(\hat{\mathbf{X}}_m)]\delta\mathbf{X}_0. \tag{2.8}$$

While one can adjust each individual matrix at each iterate to have eigenvalues with magnitudes less than one, that does not guarantee that the product goes to zero as n goes to infinity[3]. Below we give a procedure which yields convergence of our observer in the chaotic case.

For specificity of the discussion, we will assume the chaotic attractor of our system to be hyperbolic and to have two positive Lyapunov exponents with the rest negative. Thus, the tangent space at each point on the attractor can be decomposed into the sum of a two dimensional unstable subspace and a $(d-2)$ dimensional stable subspace. Noting that $\mathbf{DM}(\hat{\mathbf{X}}_n)$ maps the unstable subspace at $\hat{\mathbf{X}}_n$ into the unstable subspace at $\mathbf{M}(\hat{\mathbf{X}}_n)$ and similarly maps the stable subspace at $\hat{\mathbf{X}}_n$ into the stable subspace at $\mathbf{DM}(\hat{\mathbf{X}}_n)$, we see that,

[3] As an example, the product of the following sequence of matrices:

$$\begin{bmatrix} 1/2 & 2 \\ 0 & 1/2 \end{bmatrix} \begin{bmatrix} 1/2 & 0 \\ 2 & 1/2 \end{bmatrix} \begin{bmatrix} 1/2 & 2 \\ 0 & 1/2 \end{bmatrix} \cdots$$

will be infinite while the eigenvalues of each individual matrix are less than one, i.e., $1/2$.

if $\mathbf{C}_n$ is chosen to lie in the unstable subspace at $\hat{\mathbf{X}}_n$, then the matrix representation of $[\mathbf{DM}(\hat{\mathbf{X}}_n) - \mathbf{C}_n\mathbf{D}g(\mathbf{M}(\hat{\mathbf{X}}_n))\mathbf{DM}(\hat{\mathbf{X}}_n)]$ can be put in the following block form:

$$\begin{bmatrix} \mathbf{U}_n & \mathbf{W}_n \\ \mathbf{0} & \mathbf{S}_n \end{bmatrix}$$

In this representation, $\mathbf{U}_n$ is a 2×2 submatrix acting on the unstable subspace, $\mathbf{S}_n$ is a $(d-2) \times (d-2)$ submatrix acting on the stable subspace, and $\mathbf{W}_n$ is a $2 \times (d-2)$ submatrix taking vectors from the stable subspace into the unstable subspace. One should note that $\mathbf{U}_n$ and $\mathbf{W}_n$ are functions of the yet to be determined control vector $\mathbf{C}_n$, and that $\mathbf{S}_n$ is known [it is given by $\mathbf{DM}(\hat{\mathbf{X}}_n)$ restricted to the stable subspace].

We now can analyze the convergence of Eq. (2.8) by examining the product of n of these block matrices, which is given by the following formula:

$$\begin{bmatrix} \mathbf{U}_n\mathbf{U}_{n-1}\cdots\mathbf{U}_1 & \sum_{i=1}^{n}\left[\prod_{j=i+1}^{n}\mathbf{U}_j\mathbf{W}_i\prod_{k=1}^{i-1}\mathbf{S}_k\right] \\ \mathbf{0} & \mathbf{S}_n\mathbf{S}_{n-1}\cdots\mathbf{S}_1 \end{bmatrix}. \tag{2.9}$$

Since the product $\mathbf{S}_n\mathbf{S}_{n-1}\cdots\mathbf{S}_1$ goes to zero as $n \to \infty$, the convergence of the product matrix, Eq. (2.9), depends on the product $\mathbf{U}_n\mathbf{U}_{n-1}\cdots\mathbf{U}_1$ and on the off diagonal term $\sum_{i=1}^{n}\left[\prod_{j=i+1}^{n}\mathbf{U}_j\mathbf{W}_i\prod_{k=1}^{i-1}\mathbf{S}_k\right]$. It is demonstrated in Sec. (5.1) that if one chooses the control vector $\mathbf{C}_n$ so that the product $\mathbf{U}_n\mathbf{U}_{n-1}\cdots\mathbf{U}_1$ goes to zero as $n \to \infty$, then the whole matrix, Eq. (2.9), will go to zero as well.

To make the product $\mathbf{U}_n\mathbf{U}_{n-1}\cdots\mathbf{U}_1 \to 0$ as $n \to \infty$, first consider each matrix $\mathbf{U}_n$ to be lower triangular (i.e., with $U_{ij} = 0$ for $i < j$); then we have the following: (i) the product of two or more such matrices will still be lower triangular; (ii) the eigenvalues are just the diagonal elements; and most importantly, (iii) the eigenvalues of the product of such matrices will be the product of their respective eigenvalues taken from their diagonals. Thus, if we choose $\mathbf{C}_n$ so that $\mathbf{U}_n$ is lower triangular with eigenvalues of magnitude less than one, then the product of the $\mathbf{U}_n$'s will also be lower triangular with eigenvalues of magnitude less than one. Most importantly, it can be shown that the product $\mathbf{U}_n\mathbf{U}_{n-1}\cdots\mathbf{U}_1 \to 0$ as $n \to \infty$ (see Sec. (5.1)). Thus, we want to choose a basis for the unstable subspace, such that each of the $\mathbf{U}_n$ will be lower triangular, while simultaneously choosing $\mathbf{C}_n$, such that the eigenvalues of $\mathbf{U}_n$ will have magnitudes less than one.

The first step in our procedure is to define two numbers, $\lambda_n^{(1)}$ and $\lambda_n^{(2)}$, and two basis unit column vector, $\mathbf{e}_n^{(1)}$ and $\mathbf{e}_n^{(2)}$, for the unstable subspace at $\hat{\mathbf{X}}_n$ according to the following iterative procedure:

$$\lambda_n^{(1)}\mathbf{e}_{n+1}^{(1)} = \left[\mathbf{DM}(\hat{\mathbf{X}}_n)\right]\mathbf{e}_n^{(1)}, \tag{2.10}$$

$$\lambda_n^{(2)}\mathbf{e}_{n+1}^{(2)} = \left[\mathbf{DM}(\hat{\mathbf{X}}_n) - \{C_n^{(1)}\mathbf{e}_{n+1}^{(1)}\}\mathbf{D}g(\mathbf{M}(\hat{\mathbf{X}}_n))\mathbf{DM}(\hat{\mathbf{X}}_n)\right]\mathbf{e}_n^{(2)}, \tag{2.11}$$

with $\mathbf{e}_0^{(1)}$ and $\mathbf{e}_0^{(2)}$ initialized from any two linearly independent column vectors in the unstable subspace of $\mathbf{DM}(\mathbf{X}_0)$. Here, $\lambda_n^{(1)}$ and $\lambda_n^{(2)}$ are the normalization factors associated with $\mathbf{e}_{n+1}^{(1)}$ and $\mathbf{e}_{n+1}^{(2)}$, respectively. We want to remind the reader that in this non orthogonal basis, the components of $\mathbf{U}_n$ are given by the "inner product," $(\mathbf{U}_n)_{ij} = \mathbf{f}_{n+1}^{(i)}\mathbf{U}_n\mathbf{e}_n^{(j)}$, where the contravariant row vectors $\mathbf{f}_{n+1}^{(i)}$ are defined by $\mathbf{f}_{n+1}^{(i)}\mathbf{e}_{n+1}^{(j)} = \delta_{ij}$. With this basis representation, $\mathbf{U}_n$ will be in a lower triangular form with two free parameters $C_n^{(1)}$ and $C_n^{(2)}$:

$$\mathbf{U}_n = \begin{bmatrix} \lambda_n^{(1)} - C_n^{(1)}Dh_n^{(1)} & 0 \\ -C_n^{(2)}Dh_n^{(1)} & \lambda_n^{(2)} - C_n^{(2)}Dh_n^{(2)} \end{bmatrix}, \tag{2.12}$$

where

$$Dh_n^{(i)} = \mathbf{D}g(\mathbf{M}(\hat{\mathbf{X}}_n))\mathbf{DM}(\hat{\mathbf{X}}_n)\mathbf{e}_n^{(i)}$$

and $C_n^{(i)} = \mathbf{f}_{n+1}^{(1)}\mathbf{C}_n$. If we adjust $C_n^{(1)}$ and $C_n^{(2)}$ so that the eigenvalues (i.e., the diagonal elements of Eq. (2.12)) of $\mathbf{U}_n$ are less than one, then the product of the matrices in Eq. (2.9) will converge to zero as n increases.

A possible concern with our method, as outlined above, is that, as time n increases, the vectors $\mathbf{e}_n^{(1)}$ and $\mathbf{e}_n^{(2)}$ might tend to become more and more nearly parallel. (This would invalidate our procedure since we assume that $\mathbf{e}_n^{(1)}$ and $\mathbf{e}_n^{(2)}$ span the two-dimensional unstable subspace.) We note, however, that we have the freedom of choosing the eigenvalues of $\mathbf{U}_n, \Lambda_n^{(i)} = \lambda_n^{(i)} - C_n^{(i)}Dh_n^{(i)}$. If we choose $\Lambda_n(1)$ to be zero, then the collapse of $\mathbf{e}_n^{(1)}$ and $\mathbf{e}_n^{(2)}$ to a common direction can be prevented (see next paragraph), still leaving open one degree of freedom in choosing $\Lambda_n^{(2)}$. For definiteness and faster convergence, we set $\Lambda_n^{(1)}$ as well as $\Lambda_n^{(2)}$ to zero, in which case we have,

$$\begin{aligned} \mathbf{C}_n &= C_n^{(1)}\mathbf{e}_{n+1}^{(1)} + C_n^{(2)}\mathbf{e}_{n+1}^{(2)} \\ &= (\lambda_n^{(1)}/Dh_n^{(1)})\mathbf{e}_{n+1}^{(1)} + (\lambda_n^{(2)}/Dh_n^{(2)})\mathbf{e}_{n+1}^{(2)}. \end{aligned} \tag{2.13}$$

The expression in Eq. (2.13) for the control vector $\mathbf{C}_n$ is valid as long as the denominators $Dh_n^{(i)}$ are not zero. In our numerical program, we set a minimum value such that whenever $Dh_n^{(i)}$ falls below that value, we set the control vector to zero. Thus, when $Dh_n^{(i)}$ are small, we do not attempt to bring $\mathbf{X}$ and $\hat{\mathbf{X}}$ together. But, if they were already close, they will still be close one iterate later. Hence, little is lost by turning the control off for one iterate, provided that this is done only infrequently.

To see that $\mathbf{e}_n^{(1)}$ and $\mathbf{e}_n^{(2)}$ do not typically approach a common direction as n increases, we assume that they are nearly parallel at time n, and then demonstrate that Eqs. (2.10),(2.11) and the expression for $C_n^{(1)}$ in Eq. (2.13) imply that they are not nearly parallel at time $n+1$. Setting $\mathbf{e}_n^{(2)} = \mathbf{e}_n^{(1)} + \delta\mathbf{e}_n$ with $|\delta\mathbf{e}_n| \ll 1$, Eqs. (2.10),(2.11) and (2.13) yield

$$\lambda_n^{(2)}\mathbf{e}_{n+1}^{(2)} = \mathbf{DM}(\hat{\mathbf{X}}_n)\delta\mathbf{e}_n - \lambda_n^{(1)}\mathbf{e}_{n+1}^{(1)}\{\Big[\mathbf{D}g(\mathbf{M}(\hat{\mathbf{X}}_n))\mathbf{DM}(\hat{\mathbf{X}}_n)\delta\mathbf{e}_n\Big]/Dh_n^{(1)}\}.$$

Thus $\mathbf{e}_{n+1}^{(2)}$ consists of two terms which are both typically of order $\delta\mathbf{e}_n$. The first term points in the direction $\mathbf{DM}(\hat{\mathbf{X}}_n)\delta\mathbf{e}_n$, which is different from the direction of $\mathbf{e}_{n+1}^{(1)}$ because $\delta\mathbf{e}_n$ is approximately perpendicular to $\mathbf{e}_n^{(1)}$ by assumption. The second term points in the direction of $\mathbf{e}_n^{(1)}$ [which is the direction of $\mathbf{DM}(\hat{\mathbf{X}}_n)\mathbf{e}_n^{(1)}$]. Normally, since both terms are of order $\delta\mathbf{e}_n$, $\mathbf{e}_{n+1}^{(2)}$ will in general point in a different direction than $\mathbf{e}_{n+1}^{(1)}$. However, one can see a problem in the rare cases when $Dh_n^{(1)}$ is small. In these cases, the second term dominates the first term and we will have $\mathbf{e}_{n+1}^{(2)}$ nearly parallel to $\mathbf{e}_{n+1}^{(1)}$, but we avoid these "glitches" anyway by turning off the control vector, i.e., $\mathbf{C}_n \equiv \mathbf{0}$.

Although the above discussion is in the context of a two dimensional unstable subspace, we note that no essential change is produced in the case where the unstable subspace has an arbitrary dimension d_u. In particular, Eqs. (2.10),(2.11) generalizes in a natural way to d_u equations for the d_u basis vectors $\mathbf{e}^{(i)}$. This generalization is given in the Sec. 5.2). Also treated is the generalization to the case where the observation is a vector $\mathbf{O} = \mathbf{g}(\mathbf{X})$ of dimension $1 < d_0 < d$.

Since our method reconstructs the full state vector of the system, i.e., all d components of the d-dimensional vector $\mathbf{X}_n$, it is called the full-order observer. Computationally, since our method requires the manipulation of only d_u equations for the d_u basis vectors $\mathbf{e}^{(i)}$ at each iterate, the calculation for the control vector is relatively simple when $d \ll d_u$. In contrast, the extended Kalman filter requires the manipulation of $d \times d$ matrices at each iterate. See

Sec. (2.6) for a comparison of our technique with a extended Kalman filter.

2.4 Convergence Characteristics and the Kicked Double Rotor Example

To access the convergence characteristics of our chaotic observer technique, we will use a four dimensional map which describes the time evolution of a mechanical system, called the kicked double rotor[5, 6]. As shown in the illustration, Fig. (2.1), the kicked double rotor consists of two massless rods of lengths L_1 and L_2 connected at the pivot p_2 and with the other end of rod 1 connected to a fixed pivot at p_1. Point masses m_1 and $m_2/2$ are attached at the end of rod 1 and the two ends of rod 2 as shown. At one of the ends of rod 2, an impulse force, $\mathbf{f}(t) = f_0 \sum n = 0, \infty \delta(t - nT)\hat{\mathbf{y}}$, is applied at times $t = 0, T, 2T, ...$ The kicked double rotor is governed by the following set of equations:

$$\mathbf{X}_{n+1} = \begin{bmatrix} \theta_{n+1} \\ \dot{\theta}_{n+1} \end{bmatrix} = \begin{bmatrix} \mathbf{K}\dot{\theta}_n + \theta_n \\ \mathbf{L}\dot{\theta}_n + \mathbf{G}(\theta_{n+1}) \end{bmatrix}, \tag{2.14}$$

where $\theta = (\theta_1, \theta_2)^\dagger, \dot{\theta} = (\dot{\theta}_1, \dot{\theta}_2)^\dagger$, and $\mathbf{G}(\theta) = (a_1 \sin\theta_1, a_2 \sin\theta_2)^\dagger$ (here †denotes transpose). θ_1 and θ_2 are angle variables giving the positions of the rotor arms, and $\dot{\theta}_1$ and $\dot{\theta}_2$ are the angular velocities of the rotor arms at the instant immediately after the nth kick. $a_{1,2} = (f_0/I)L_{1,2}$ are constants proportional to the strength of the periodic kick $\mathbf{f}(t)$. The moments of inertia about pivots 1 and 2 are chosen to be equal, $I = (m_1 + m_2)L_1^2 = m_2 L_2^2$. $\mathbf{K}$ and $\mathbf{L}$ are constant matrices defined by

$$\mathbf{L} = \sum_{i=1}^{2} \mathbf{W}_i e^{\zeta_i T}, \mathbf{K} = \sum_{i=1}^{2} \mathbf{W}_i \frac{e^{\zeta_i T} - 1}{\zeta_i},$$

$$\mathbf{W}_1 = \begin{bmatrix} \alpha & \beta \\ \beta & \sigma \end{bmatrix}, \mathbf{W}_2 = \begin{bmatrix} \sigma & -\beta \\ -\beta & \alpha \end{bmatrix},$$

$$\alpha = \frac{1}{2}\left(1 + \frac{\nu_1}{\Delta}\right), \sigma = \frac{1}{2}\left(1 - \frac{\nu_2}{\Delta}\right), \beta = -\frac{\nu_2}{\Delta},$$

$$\zeta_{1,2} = -\frac{1}{2}(\nu_1 + 2\nu_2 \pm \Delta), \Delta = (\nu_1^2 + 4\nu_2^2)^{1/2},$$

where ν_1 and ν_2 are the friction coefficients at the pivots (see Fig. (2.1) and Ref. [5, 6]). In our numerical experiment, we used $g(\mathbf{X}) = \theta_2$ and have chosen a particular set of values for

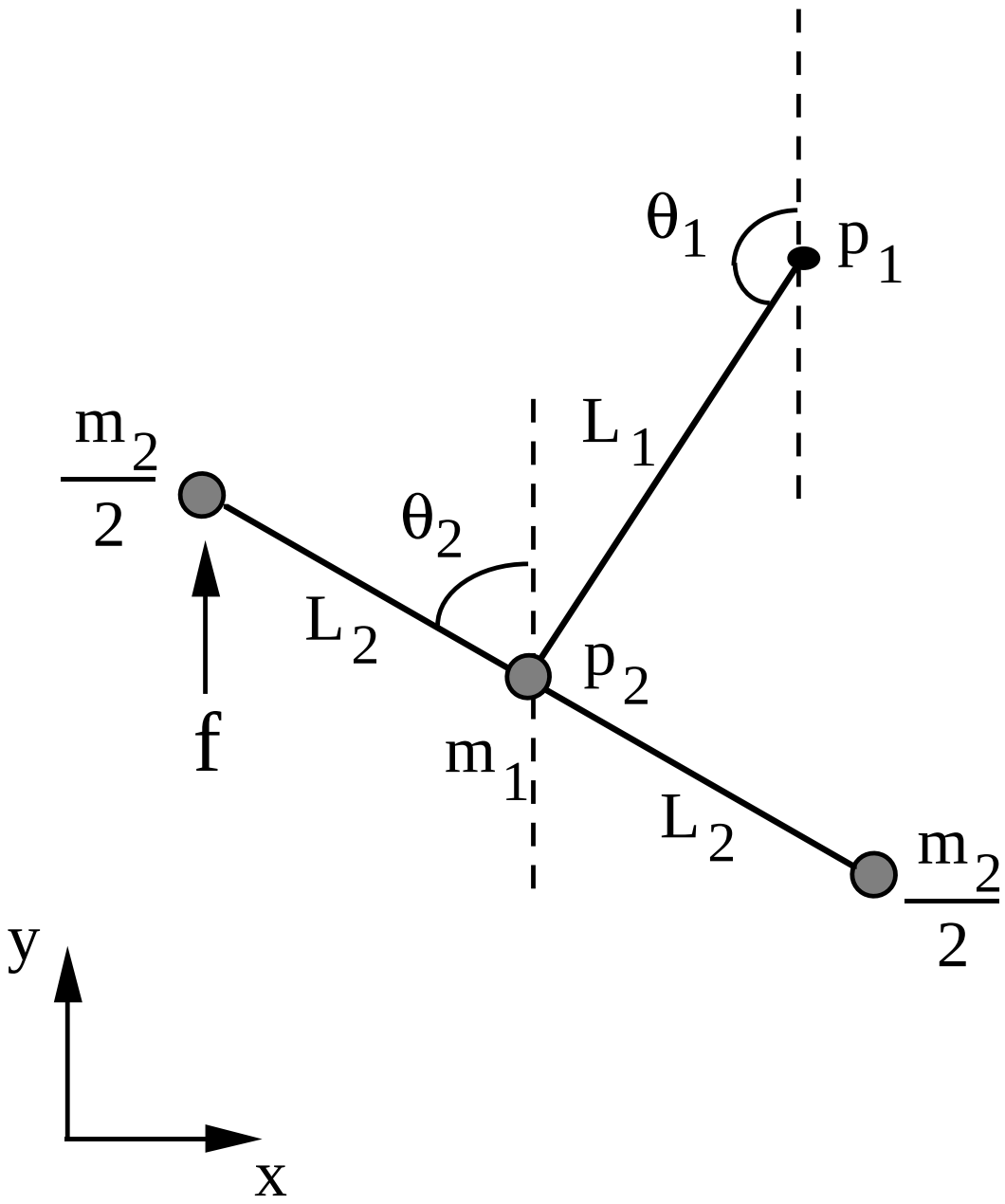

Figure 2.1: The double rotor.

the physical parameters[4]. The resulting chaotic attractor has one positive Lyapunov exponent ($\Lambda_L^{(1)} = 0.670, \Lambda_L^{(2)} = -0.4040, \Lambda_L^{(3)} = -1.192, \Lambda_L^{(4)} = -2.074$). Hence $\Lambda_L^{(1)} + \Lambda_L^{(2)} > 0$ while $\Lambda_L^{(1)} + \Lambda_L^{(2)} + \Lambda_L^{(3)} < 0$, and the Lyapunov dimension[8] of the attractor is thus given by

$$d_L = 2 + (\Lambda_L^{(1)} + \Lambda_L^{(2)})/\Lambda_L^{(3)},$$

which approximately yields 2.22. It is interesting to note that, although the attractor has only one positive Lyapunov exponent, there exist periodic orbits on the attractor with two dimensional unstable tangent spaces, and other periodic orbits on the attractor with one dimensional unstable tangent spaces[9]. Thus, the kicked double rotor map is not globally hyperbolic as assumed in the previous theoretical discussion. Nevertheless, we find that our method still works , and the performance is better if we use two basis vectors [as in Eqs. (2.10)-(2.13)].

First, we examine the behavior of the observer if the observer test orbit starts inside the linear region of the true orbit. The characteristic time for this case will, in principle, be dependent upon the chosen eigenvalues of $\mathbf{U}_n$. Ideally (i.e., if the dynamics were truly described by Eq. (2.7)), if we choose the eigenvalues of $\mathbf{U}_n$ to all be zero and neglect nonlinear effects, then the observer error along the unstable direction should vanish in two steps[5]. However, since the action of the U's is only a linear approximation of the true dynamics of the chaotic system, the average number of iterates[6] needed to bring the separation between the observer orbit and the true orbit from 5.0×10^{-3} down to 1.0×10^{-7} in a normalized unit is about 10. Furthermore, when we increase the magnitude of the eigenvalue[7], Λ_n^2, the number of iterates needed to bring the separation down increases as expected. Figure 2.2 is a graph showing

[4]In terms of the notation used in Fig. (2.1) (see also Romeiras *et al.*, the parameters used in our numerical example are: $L_1 = 1, L_2 = 1.1, m_2 = (1.1)^{-2}, m_1 = 1 - m_2, \nu_1 = \nu_2 = 1$; the time interval between successive kicks is $T = 1$; the impulse strength of a kick is $f_0 = 6$ (which gives $a_1 = 6$ and $a_2 = 6.6$). For this case, synchronism as defined by Pecora and Carroll[7] does not occur.

[5]In our numerical experiment, $\mathbf{U}_n$ is in the following form, $\begin{bmatrix} 0 & 0 \\ X & 0 \end{bmatrix}$. The product of two of these matrices is identically zero. In general, when the dimension of $\mathbf{U}_n$ is d_u (see Sec. (5.2)), if $\mathbf{U}_n$ is lower triangular with zeros on the diagonal, then the product of these $\mathbf{U}'s$ will go to zero in d_u iterates.

[6]The average is determined from 5000 randomly chosen initial observer test orbits within the linear region of the true orbit.

[7]As mentioned earlier, we are only free to choose $\Lambda_n^{(2)}$ because we need to keep the basis vectors in Eqs. (2.10)

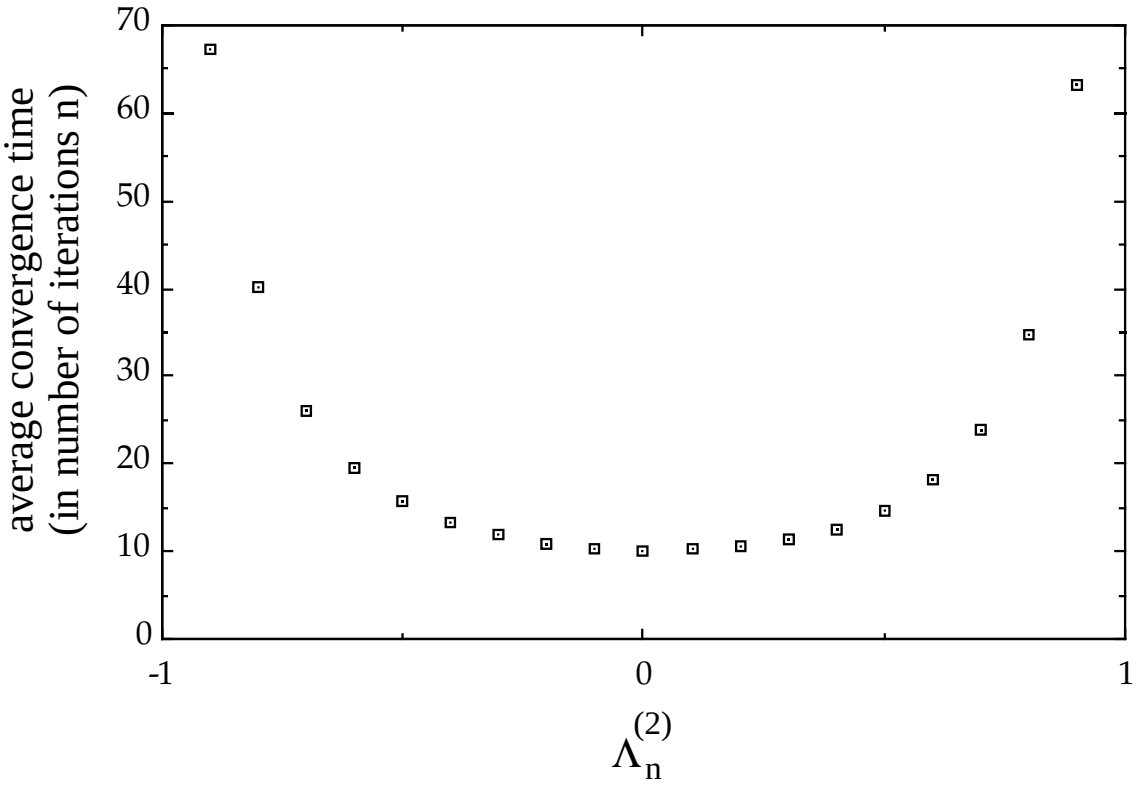

Figure 2.2: Averaged convergence time (in numbers of iteration steps n) vs. the magnitude of the second eigenvalue of $\mathbf{U}_n, \Lambda_n^{(2)}$. The convergence time is defined to be the number of iterates that the observer takes to reduce $|\mathbf{X}_n - \hat{\mathbf{X}}_n|$ ten thousands times (from 5.0×10^{-3} to 1.0×10^{-7}) and the average value is taken over five thousands randomly chosen observers.

the average converging time of this chaotic observer as a function of Λ_n^2. For the fastest convergence time, it is in principal desirable to choose all eigenvalues of $\mathbf{U}_n$ to be zero as done in Eq. (2.13).

We now discuss the convergence characteristics of our observer technique for observer initial conditions outside the linear region. Typically, an observer orbit $\hat{\mathbf{X}}_n$ begins to track the true orbit $\mathbf{X}_n$ when $\hat{\mathbf{X}}_n$ is located within the linear region of the map $\mathbf{M}(\mathbf{X}_n)$. Furthermore, if we wait long enough, an initially non tracking observer orbit $\hat{\mathbf{X}}_n$ will typically and eventually fall within the linear region of $\mathbf{M}(\mathbf{X}_n)$ at some future time n. In our numerical experiments, we

and (2.11) from collapsing by setting $\Lambda_n^{(1)} = 0$. Recall that in Eq. (2.13), we set $\Lambda_n^{(2)} = 0$ also for faster convergence rate. (Also, we use $\Lambda_n^{(2)} = 0$ in our numerical experiments, Figs. (2.3)-(2.6).)

found that the average transient time before tracking sets in could be quite long. To remedy this problem, we use many observer test points with randomly chosen initial conditions on the attractor, and we continuously test each one to see if it has locked onto the true orbit $\mathbf{X}_n$. We do this by calculating $g(\mathbf{X}_n) - g(\hat{\mathbf{X}}_n)$ and declaring the orbits $\mathbf{X}_n$ and $\hat{\mathbf{X}}_n$ locked if this quantity is small for several successive iterates. We then take the observer state as $\hat{\mathbf{X}}_n$ for such a locked orbit. We can estimate the typical number of observer test orbits needed by determining the average convergence time $\langle\tau\rangle$ of a single observer. To determine this average time $\langle\tau\rangle$, we begin with a large number of randomly chosen observer test orbits. Then, a semi-log plot of the number $\hat{N}$ of orbits which are still not tracking the true orbit after a time interval n is generated. Since the number of such orbits typically decays exponentially with n, i.e., $\hat{N}(n) = N_0 e^{-n/\langle\tau\rangle}$, the inverse of the slope of this graph defines an average time $\langle\tau\rangle$ needed for an observer orbits to converge to the true orbit. In Figure 2.3, we used five thousands randomly chosen observer test orbits and we estimated $\langle\tau\rangle \quad 1500$. This value also gives a reasonable number of observer test orbits to be used so that at least one observer orbit will be tracking the true orbit after the first few time steps.

2.5 Chaotic Observer - Reduced Order

A variant of our technique discussed in Sec. (2.3) can be formulated if there exists an invertible coordinate transformation

$$\mathbf{T} : \mathbf{X} \equiv (X^1, \cdots, X^{d-1}, X^d) \rightarrow (\mathbf{Y}|Z) \equiv (Y^1, \cdots, Y^{d-1}, Z),$$

where Z is the observed quantity $g(\mathbf{X}_n)$. In this case, the observer only needs to estimate a $(d-1)$-dimensional vector, $\mathbf{Y}$, since Z is known from direct measurement. The state equation $\mathbf{X}_{n+1} = \mathbf{M}(\mathbf{X}_n)$ under this coordinate transformation $\mathbf{T}$, can be written as

$$\mathbf{Y}_{n+1} = \mathbf{M}_Y(\mathbf{Y}_n, Z_n) \text{and} Z_{n+1} = M_Z(\mathbf{Y}_n, Z_n), \tag{2.15}$$

where $(\mathbf{M}_Y(\bullet), M_Z(\bullet))$ is the representation of $\mathbf{M}(\bullet)$ in the new coordinate system. The reduced-order observer for the the unmeasured part of the state vector $\mathbf{Y}_n$ can then be defined as

$$\hat{\mathbf{Y}}_{n+1} = \mathbf{M}_Y(\hat{\mathbf{Y}}_n, Z_n) + \mathbf{C}_n \left[Z_{n+1} - M_Z(\hat{\mathbf{Y}}_n, Z_n) \right], \tag{2.16}$$

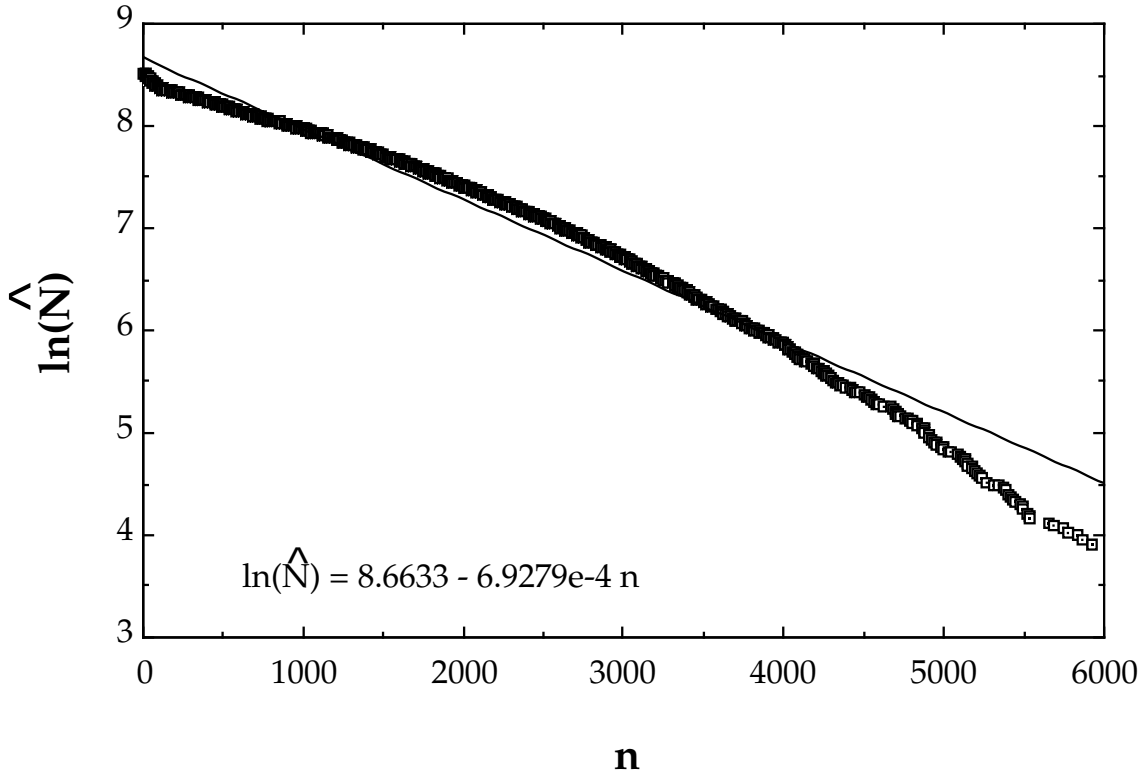

Figure 2.3: $\ln(\hat{N})$ vs. n with 5000 randomly chosen initial observer test points. An observer test orbit is said to be tracking the true orbit when $|\mathbf{X}_n - \hat{\mathbf{X}}_n| < 1.0 \times 10^{-6}$.

where $\mathbf{C}_n$ is the $(d-1)$-dimensional control vector corresponding to the reduced order observer. Forming the error equation, we have

$$\delta\mathbf{Y}_{n+1} = [\mathbf{D}\mathbf{M}_Y(\mathbf{Y}_n, Z_n) - \mathbf{C}_n\mathbf{D}M_Z(\mathbf{Y}_n, Z_n)]\,\delta\mathbf{Y}_n, \tag{2.17}$$

which can be treated using exactly the same techniques as already discussed. A similar expression for the control vector $\mathbf{C}_n$ can be derived as before [Eq. (2.13)], but with $\mathbf{D}g(\mathbf{M}(\hat{\mathbf{X}}_n))\mathbf{D}\mathbf{M}(\hat{\mathbf{X}}_n)$ replaced by $\mathbf{D}M_Z(\mathbf{Y}_n, Z_n)$. The main obvious advantage achieved by doing this is that the dimensionality of the observer is reduced by one.

From a different viewpoint, the reduced-order observer and the actual system can be considered as a pair of coupled systems with the actual system providing the driving signal and the observer as the response function. This pair of driven-response systems reduce to the one studied by Pecora and Carroll[7] when the feedback control in our reduced-order observer is turn off ($\mathbf{C}_n \equiv \mathbf{0}$). The resultant observer in this case has also been called a "trivial reduced-order observer." The convergence of this trivial reduced-order observer will obviously depend on the Lyapunov exponents of the system $\mathbf{Y}_{n+1} = \mathbf{M}_Y(\mathbf{Y}_n, Z_n)$. Since $\mathbf{M}_Y(\bullet)$ is basically a subsystem of the full dynamical system $\mathbf{M}(\bullet)$, the number of positive Lyapunov exponents of $\mathbf{M}_Y(\bullet)$ cannot be larger than the number of positive Lyapunov exponents of $\mathbf{M}(\bullet)$. Pecora and Carroll[7] discuss the case where a physically constructed subsystem $\mathbf{M}_Y(\bullet)$ has no positive Lyapunov exponents, and it is then possible to synchronize $\mathbf{M}_Y(\bullet)$ with the chaotic signal generated by $\mathbf{M}(\bullet)$.

Returning now to our discussion of our reduced-order observer and using the double rotor map example (with the same set of parameters as in the full-order observer), we calculated the Lyapunov spectrums for the four different choices of the observed quantity, $g(\mathbf{X}_n) = \theta_1, \theta_2, \dot{\theta}_1, \text{and} \dot{\theta}_2$. In all these cases, $\mathbf{T}_Y(\mathbf{X})$ will simply be a projection onto the unmeasured components of $\mathbf{X}$. The results are given in Table 2.5. For our numerical experiment, we have chosen $g(\mathbf{X}_n) = \theta_2$. In this case, the subsystem has one positive Lyapunov exponent so that synchronism as defined by Pecora and Carroll does not apply. However, as mentioned earlier, since the double rotor map is nonhyperbolic, we found the performance of the reduced order observer is better if we used two basis vectors (rather than one) in our calculation for the control vector $\mathbf{C}_n$.

Noise arises naturally in any real physical systems. For example, the strength of the kick

Table 2.1: Table of sub-Lyapunov exponents for the reduced rotor map with the observed quantity $g(\mathbf{X}_n) = \theta_1, \theta_2, \dot{\theta}_1, \dot{\theta}_2$. The sub-Lyapunov exponents are calculated from a single orbit over 10^6 iterates.

Quantity	$\lambda_L^{(1)}$	$\lambda_L^{(2)}$	$\lambda_L^{(3)}$
$g(\mathbf{X}) = \theta_1$	0.6716	-0.3414	-1.4209
$g(\mathbf{X}) = \theta_2$	0.5916	-0.4437	-1.4473
$g(\mathbf{X}) = \dot{\theta_1}$	0.6603	0.0000	-1.3258
$g(\mathbf{X}) = \dot{\theta_2}$	0.0000	-0.3036	-1.1176

in our double rotor might fluctuate because of nonuniformity of the motor output or there might be imprecision in the measuring device for the scalar time series. The simplest way to model noise into our system is to put an additive term $\varepsilon_a \boldsymbol{\varphi}_n$ to the right hand side of the double rotor map Eq. (2.4) to denote noise in the actual system and another additive term to the output function $O_n = g(\mathbf{X}_n) + \varepsilon_b \nu_n$ to denote noise in the measurement of the observed quantity. Here, $\varepsilon_{a,b}$ are the maximum magnitude of the noise. The components of $\boldsymbol{\varphi}_n$ and ν_n are uncorrelated random variables with a given noise statistics. In our numerical example, both of these random variables are chosen to have zero mean and uniform distribution in $|\nu| < 1, |\boldsymbol{\varphi}| < 1$. In addition, we assume that the observer system has no knowledge of the noise. We expect the method to work well when $|\varepsilon_a \boldsymbol{\varphi}_n|$ and $|\varepsilon_b \nu_n|$ are less than the typical radius of the linear region of the map. Since the chaotic system is nonlinear, the size of the linear region at each point $\mathbf{X}_n$ varies. Near those points where the linear region is smaller, the observer will be more sensitive to noise. In our numerical experiment, we found that for a sufficiently small value of $\varepsilon (< 10^{-4})$, the observer was able to track the actual state continuously. However, as ε increases, the probability of the observer being kicked out of the linear region of the map, $\mathbf{M}(\mathbf{X}_n)$, increases. When this happens, the observer orbit might temporary lose track of the true system state but we can quickly lock back onto the actual orbit again by first going back a few iterates to a point where the observer and the actual state are still close together. Then, we activate a set of N observer test points randomly chosen within an neighborhood centered on that past iterate of the observer. When one of these N observer test points begins to lock onto the actual state, we pick that particular observer test

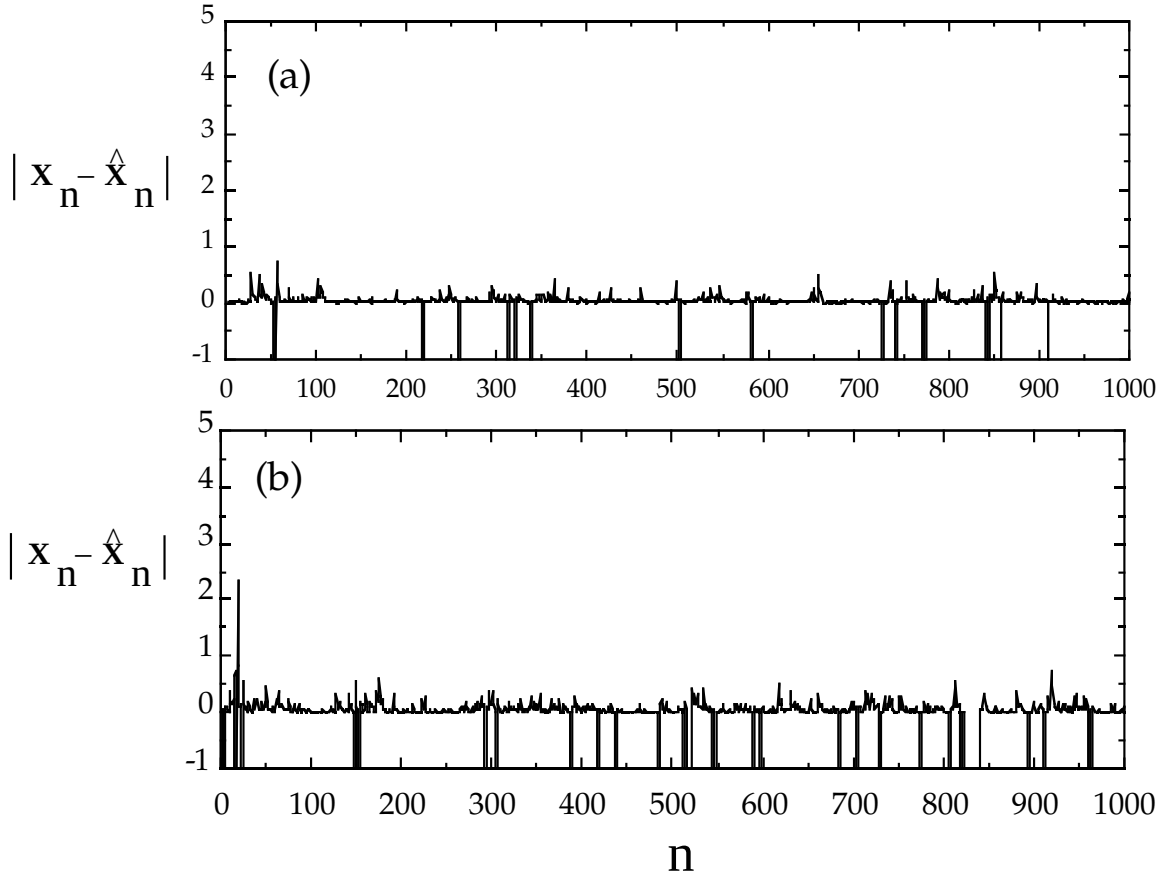

Figure 2.4: $|\mathbf{X}_n - \hat{\mathbf{X}}_n|$ vs. n with $N = 1500, \varepsilon = 2 \times 10^{-2}$. Spikes with negative magnitude indicate the moments when multiple observer test points were initiated. (a) Additive noise in actual system. (b) Additive noise in output measurements.

point as our new observed orbit and drop the rest of the N test points. On the other hand, if none of the N observer test points locks back onto the actual orbit within a given short time limit, we reinitiate the procedure with another set of N randomly chosen observer test points. Figure 2.4 shows a plot of $|\mathbf{X}_n - \hat{\mathbf{X}}_n|$ versus n with $N = 1500$ and $\varepsilon = 2 \times 10^{-2}$. (Figure 2.4a is the result for additive noise to the actual system and Figure 2.4b is the result for additive noise to the output function.) We see that our observer technique successfully tracks $\mathbf{X}_n$ even when ε is relatively large (signal to noise ratio ≈ 150) provided that N is sufficiently large.

One should note that our chaotic observer technique has an advantage over delay coordinate embedding in the situation where the system is driven by an observed time dependent variable

input which may be temporally irregular. In the presence of a time dependent variable input, delay coordinate embedding will not work simply because the correlation between the delayed vector $(O_n, O_{n-1}, \cdots, O_{n-(N-1)})$ and the system state vector $\mathbf{X}_n$ will be lost. However, since the chaotic observer tracks the actual system in real time, the observer technique will still work. In order to examine the behavior of the chaotic observer for a system driven by a time dependent variable input, we replace the fixed strength of the kick to the double rotor at time $t = nT$ by $f_n = f_0 + \beta_n$ where β_n defines the time dependent driving force to the rotor. Since we compute the control vector $\mathbf{C}_n$ in real time, the time variation in f_n will not affect our calculation provided that we have knowledge of the function β_n. In our numerical experiment, we choose $\beta_n = \varepsilon \sin[(2\pi/T)n]$, where ε is the amplitude of the perturbation and T is the period of the perturbation. When the observer orbit starts within the linear region of the map, it converge readily to the actual orbit as in the previous examples without time-dependent variable input [see Figure 2.5(a)]. However, when the observer orbit begins outside the linear region, it typically takes a much long time to converge to the actual orbit [see Figure 2.6(a)]. This behavior is similar to the previous situation when the kick strength is a fixed value. In addition, we also varied the values of ε and T for a number of different trials but there were no significant difference in the convergence characteristic of the observer in all those cases [see Figure 2.5(b) and 2.6(b)].

2.6 Extended Kalman Filter

The Kalman filter and the extended Kalman filter basically have the same mathematical structure as our nonlinear observer. This is to say that they all have the following form:

$$\hat{\mathbf{X}}_{n+1} = \mathbf{M}(\hat{\mathbf{X}}_n) + \mathbf{C}_n \left[O_{n+1} - g(\mathbf{M}(\hat{\mathbf{X}}_n)) \right], \tag{2.18}$$

where $\hat{\mathbf{X}}_n$ is the estimated state of the system, $O_n = g(\mathbf{X}_n)$ is the observed output of the system and $\mathbf{C}_n$ is the control vector which will be adjusted according to the methods used. As we have stated earlier, the fundamental consideration in choosing $\mathbf{C}_n$ in our method is stability while the fundamental consideration in choosing $\mathbf{C}_n$ in the Kalman filter is noise minimization. To be concrete, let say we have a noisy system:

$$\mathbf{X}_{n+1} = \mathbf{M}(\mathbf{X}_n) + \mathbf{H}_n \mathbf{w}_n, O_n = g(\mathbf{X}_n) + \nu_n, \tag{2.19}$$

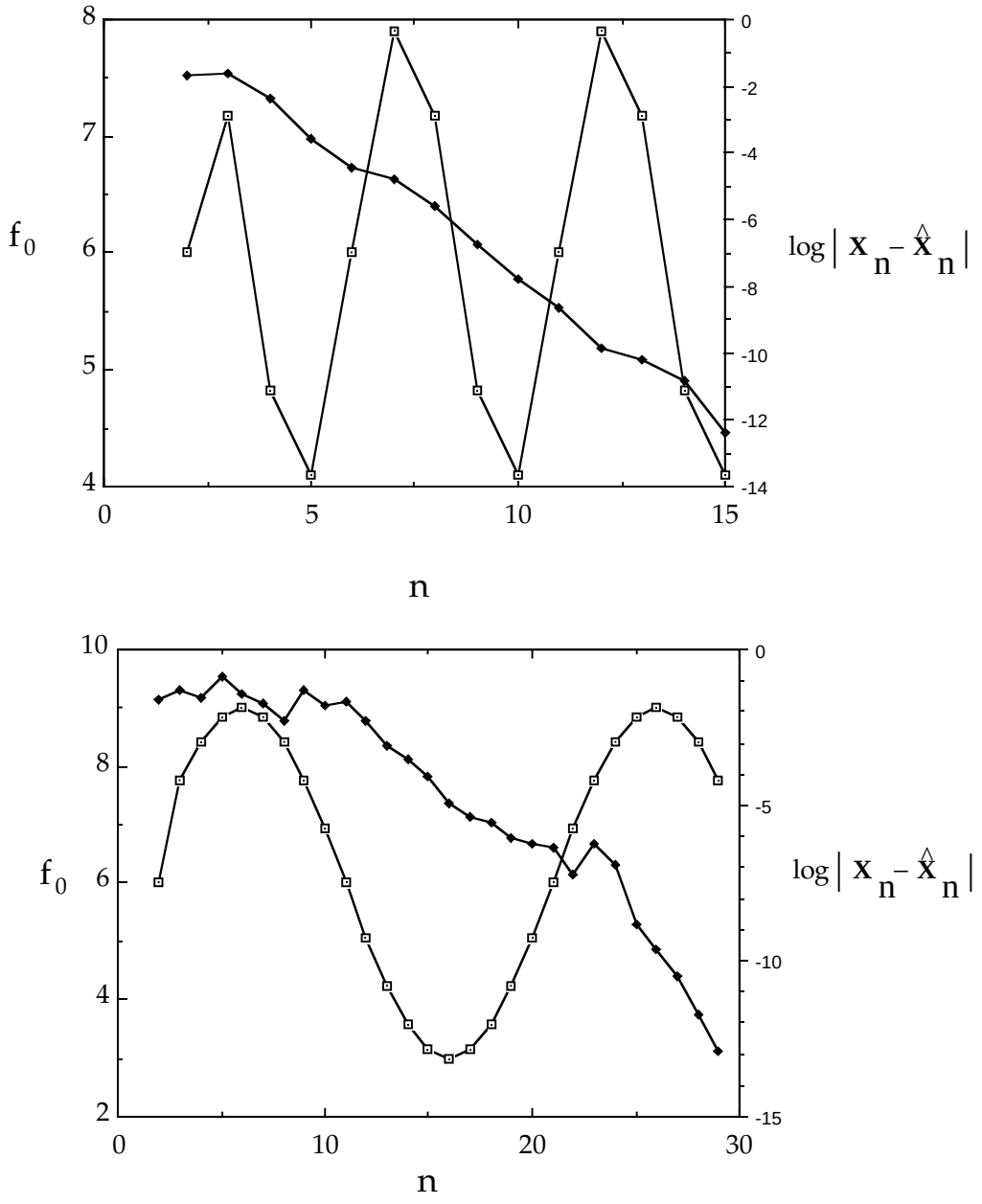

Figure 2.5: $\log_{10}|\mathbf{X}_n - \hat{\mathbf{X}}_n|$ vs. n with $\beta_n = \varepsilon\sin[(2\pi/T)n]$ and $f_0 = 6.0$. The observer orbit begins within the linear region of the actual orbit. (a) $\varepsilon = 2; T = 5$. (b) $\varepsilon = 3; T = 20$. Solid squares denote $\log_{10}|\mathbf{X}_n - \hat{\mathbf{X}}_n|$ and empty squares denote f_0.

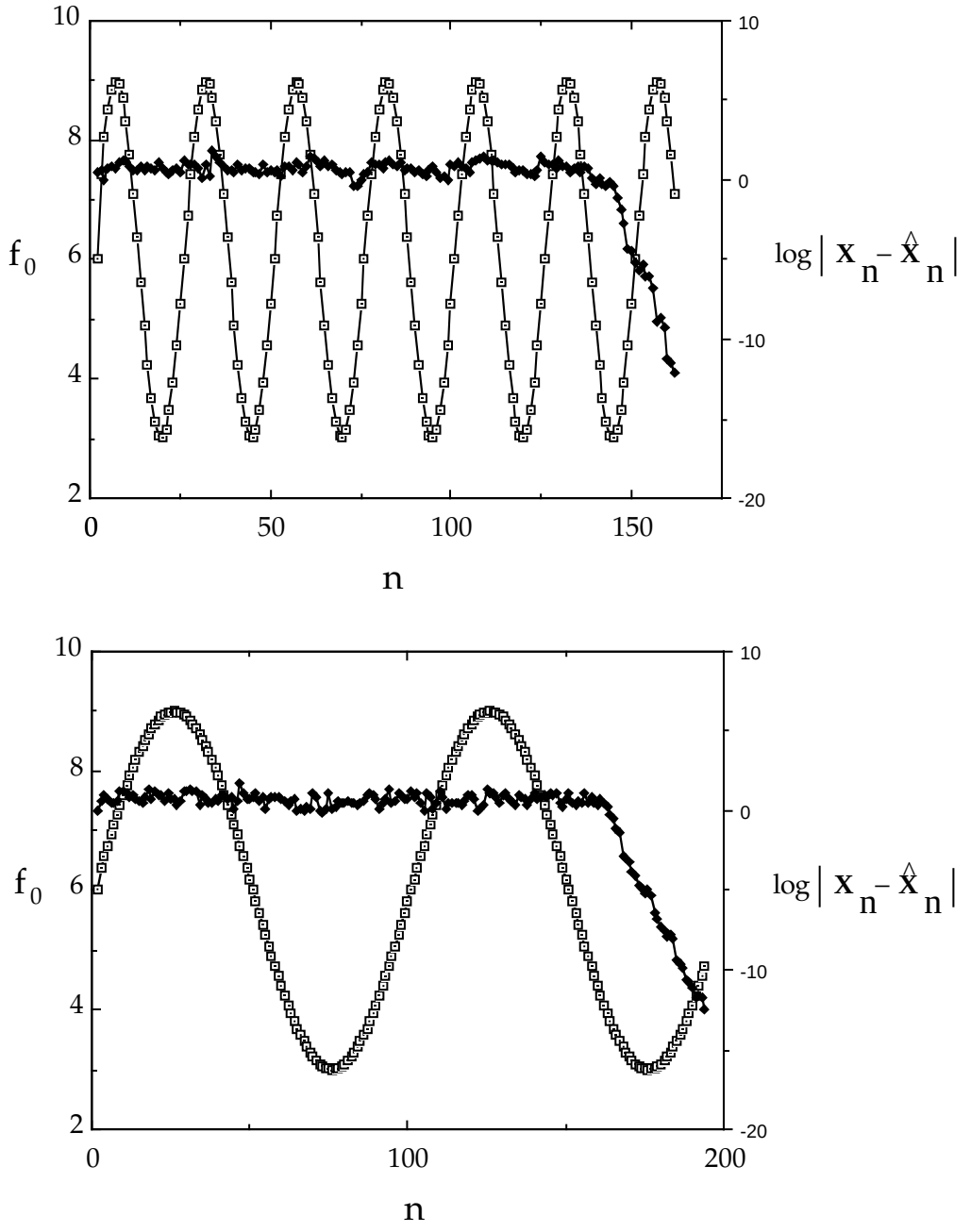

Figure 2.6: $\log_{10}|\mathbf{X}_n - \hat{\mathbf{X}}_n|$ vs. n with $\beta_n = \varepsilon\sin[(2\pi/T)n]$ and $f_0 = 6.0$. The observer orbit begins within the linear region of the actual orbit. (a) $\varepsilon = 3; T = 25$. (b) $\varepsilon = 3; T = 100$. Solid squares denote $\log_{10}|\mathbf{X}_n - \hat{\mathbf{X}}_n|$ and empty squares denote f_0.

with $E[\mathbf{w}_n\mathbf{w}_m^\dagger] = R_n\delta_{nm}$ and $E[\nu_n\nu_m^\dagger] = Q_n\delta_{nm}$ ($E[]$ denotes the expected value). We further assume that the two random processes $\{\mathbf{X}_n\}$ and $\{O_n\}$ are jointly distributed. Then, the extended Kalman filter is defined by the following set of equations:

$$\hat{\mathbf{X}}_{n+1} = \mathbf{M}(\hat{\mathbf{X}}_n) + \mathbf{C}_n[O_{n+1} - g(\mathbf{M}(\hat{\mathbf{X}}_n))], \tag{2.20}$$

$$\mathbf{C}_n = \mathbf{\Gamma}_n\mathbf{D}g_n[\mathbf{D}g_n^\dagger\mathbf{\Gamma}_n\mathbf{D}g_n + R_n]^{-1}, \tag{2.21}$$

$$\mathbf{\Sigma}_{n+1} = \mathbf{\Gamma}_n[\mathbf{1} - \mathbf{D}g_n(\mathbf{D}g_n^\dagger\mathbf{\Gamma}_n\mathbf{D}g_n + R_n)^{-1}\mathbf{D}g_n^\dagger\mathbf{\Gamma}_n], \tag{2.22}$$

$$\mathbf{\Gamma}_n = \mathbf{D}\mathbf{M}_n\mathbf{\Sigma}_n\mathbf{D}\mathbf{M}_n^\dagger + \mathbf{H}_nQ_n\mathbf{H}_n^\dagger. \tag{2.23}$$

These equations in general are initialized by setting $\hat{\mathbf{X}}_0$ to the mean value of the initial orbit $\mathbf{X}_0$ and setting $\mathbf{\Sigma}_0$ to the initial error covariance matrix $E[(\mathbf{X}_0-\hat{\mathbf{X}}_0)(\mathbf{X}_0-\hat{\mathbf{X}}_0)^\dagger]$. In the special case when the system is *time invariant* and *linear*, the corresponding linear Kalman filter can be directly derived by considering the time evolution of the means and covariance of the jointly distributed random variables $\{\mathbf{X}_n\}$ and $\{O_n\}$[10]. Actually, $\hat{\mathbf{X}}_n = E[\mathbf{X}_n|O_n]$ is the conditional mean and $\mathbf{\Sigma}_n = E[(\mathbf{X}_0 - \hat{\mathbf{X}}_0)(\mathbf{X}_0 - \hat{\mathbf{X}}_0)^\dagger|O_n]$ is the conditional error covariance of the state estimate. In the time invariant linear case, the control vector $\mathbf{C}_n$ and $\mathbf{\Sigma}_n$ are independent of the observed variable $\{O_n\}$ and there exist limiting values $\bar{\mathbf{C}}$ and $\bar{\mathbf{\Sigma}}$ for Eq. (2.21) and Eq. (2.22) respectively if the system is completely observable (see Sec. 2.2). Furthermore, it can be shown that the linear Kalman filter is optimal in the sense that $\bar{\mathbf{\Sigma}}$ for the linear Kalman filter is a minimum with respect to all other estimators in the form described by Eq. (2.18).

It is important to note that the extended Kalman filter (Eqs. (2.20) and (2.21)) is a nonlinear filter and its construction is based on the natural extension of the Kalman filter for the linearized system,

$$\mathbf{X}_{n+1} = \mathbf{D}\mathbf{M}(\hat{\mathbf{X}}_n)\mathbf{X}_n + \mathbf{H}_n\mathbf{w}_n, O_n = \mathbf{D}g(\hat{\mathbf{X}}_n)\mathbf{X}_n + \nu_n, \tag{2.24}$$

at $\hat{\mathbf{X}}_n$. Recall that the question of optimality in the linear case is well defined because $\lim_{n\to\infty}\mathbf{\Sigma}_n = \bar{\mathbf{\Sigma}}$ exists and it is reasonable to say that $\bar{\mathbf{\Sigma}}$ obtained from the Kalman filter is a minimum within a class of possible filters. However, when the extended Kalman filter is applied to the actual nonlinear system [Eq. (2.19)], $\lim_{n\to\infty}\mathbf{\Sigma}_n$ in general does not exist and the question of optimality becomes less clear. Since the optimality of the extended Kalman filter with respect to noise is not a well defined concept, we will try to compare the convergence characteristic of the extended Kalman filter and our nonlinear observer technique in the

noiseless case. It should be noted that although noise is an essential part in the construction of the standard linear Kalman filter and the extended Kalman filter, they still function as estimators in the noiseless case. Setting $\mathbf{R}_n$ and Q_n to zero, Eqs. (2.20)-(2.23) reduces to the following form,

$$\hat{\mathbf{X}}_{n+1} = \mathbf{M}(\hat{\mathbf{X}}_n) + \mathbf{C}_n[O_{n+1} - g(\mathbf{M}(\hat{\mathbf{X}}_n))], \tag{2.25}$$

$$\mathbf{C}_n = \mathbf{\Gamma}_n \mathbf{D}g_n[\mathbf{D}g_n^\dagger \mathbf{\Gamma}_n \mathbf{D}g_n + R_n]^{-1}, \tag{2.26}$$

$$\mathbf{\Sigma}_{n+1} = \mathbf{\Gamma}_n[\mathbf{1} - \mathbf{D}g_n(\mathbf{D}g_n^\dagger \mathbf{\Gamma}_n \mathbf{D}g_n)^{-1}\mathbf{D}g_n^\dagger \mathbf{\Gamma}_n], \tag{2.27}$$

$$\mathbf{\Gamma}_n = \mathbf{D}\mathbf{M}_n \mathbf{\Sigma}_n \mathbf{D}\mathbf{M}_n^\dagger. \tag{2.28}$$

A discussion of the convergence characteristic for the nonlinear full order observer can be found in Sec. (2.3) (see Figs. (2.2) and (2.3)). We have determined the average convergence time $\langle\tau\rangle$ for the extended Kalman filter using the same method as in our nonlinear observer. We begin with a large number of randomly chosen initial points for the extended Kalman filter. Then, we determine the number $\hat{N}$ of filters which are still not following the true orbit after a time interval n. From the graph of $\ln(\hat{N})$ vs. n, we estimated $\langle\tau\rangle$ to be approximately 500 (Fig. (2.7)). Comparatively, for this parameter set of the double rotor map, the extended Kalman filter has a faster convergence rate than our nonlinear observer. However, the computation for the control vector $\mathbf{C}_n$ in the extended Kalman filter requires the manipulation of matrix equations with the same dimension as the full system while our nonlinear full order observer technique requires only the manipulation of d_u basis vectors. In the case of the double rotor map ($d_u = 2$), the number of computations required in our nonlinear observer technique is about half the number of computations needed in the extended Kalman filter. Another factor of two in the number of computations can be saved if we use only one basis vector in our reduced-order observer. While our example yields a factor of three in the average convergence rate, the comparative saving in the number of computations using our method will in general improve linearly with the ratio d/d_u. We can see this by comparing Eqs. (5.15) and (5.16) for our nonlinear observer technique and Eqs. (2.25)-(2.28) for the extended Kalman filter. Assuming that we are observing only a time series of scalar output (i.e., $d_o = 1$), there will be d_u equations for the d_u basis vectors in Eq. (5.15). Since each basis vector is d dimensional, the numbers of computations needed will roughly be proportional to $d \times d_u$. On the other hand,

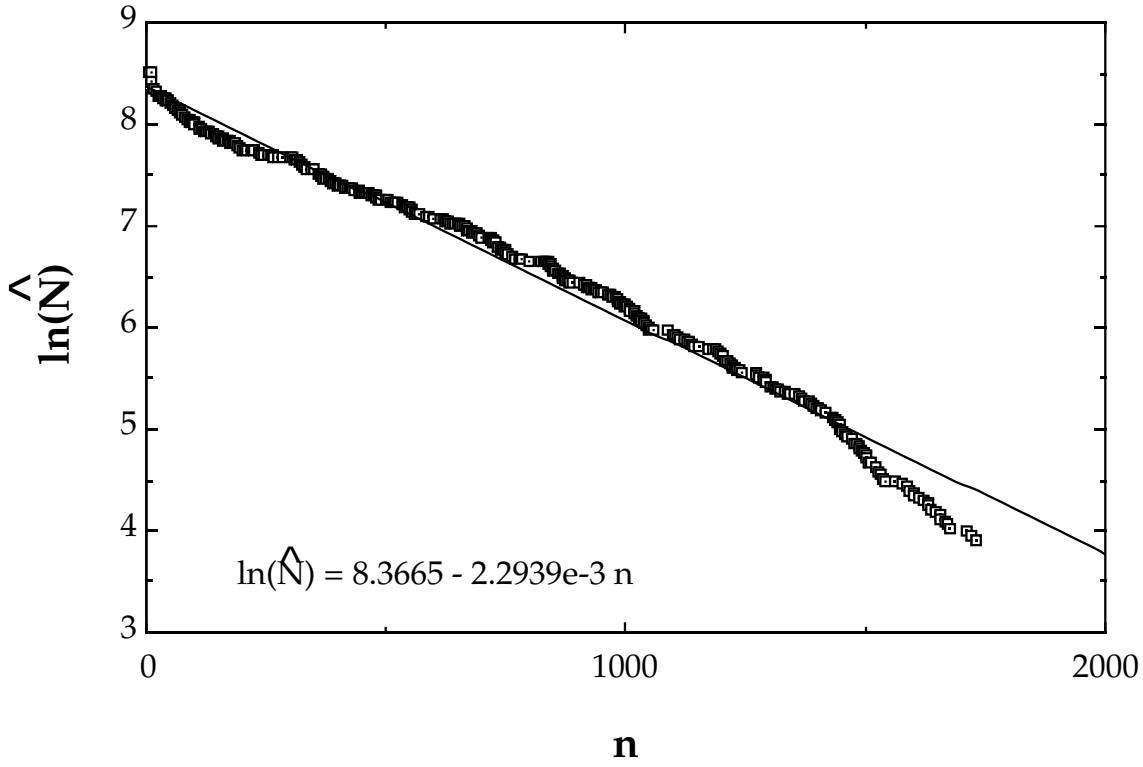

Figure 2.7: $\ln(\hat{N})$ vs. n with 5000 randomly chosen initial test points for the extended Kalman filter in the special noiseless case. A particular filter is said to be effectively working if $|\mathbf{X}_n - \hat{\mathbf{X}}_n| < 1.0 \times 10^{-6}$.

the iteration equation for the error covariance matrix $\mathbf{\Sigma}_n$ in Eq. (2.27) and Eq. (2.28) involves manipulations of $d \times d$ matrices and the number of computations needs will roughly be proportional to $d \times d$. Lastly, Eq. (5.16) and Eq. (2.26) for the control vector $\mathbf{C}_n$ in both methods are comparable in complexity. Therefore, the overall ratio of computation time between the two methods will roughly be d/d_u.

2.7 Conclusion

In this chapter, we have introduced a method for observing chaotic system from a time series of a scalar function of the system state. Our observer technique will in general be more efficient than delay coordinate embedding in terms of computation time. This is also true as compared to an extended Kalman filter in cases where $d \gg d_u$. The reduction of computational steps further improves if a reduced order observer can be constructed for the system. We have found in an example that the our observer technique can be effective in a noisy environment (with signal to noise level 150) provided we used the multiple observer technique discussed in Sec. (2.5). In addition, our observer technique still applies when the input to the system is time dependent (this situation would in general prevent utilization of embedding). Although our discussion is limited to discrete time systems, this method can be extended to continuous time cases.

Chapter 3

Controlling Chaotic Systems Using Time Delay Coordinates

3.1 Introduction

In experimental studies of chaotic dynamical systems, it is often the case that the only accessible information is a time series of some scalar function $\xi(\mathbf{X}(t)) = \xi(t)$ of a d-dimensional state variable $\mathbf{X}(t)$. Using delay coordinate embedding technique, Takens[2] shows that a delay coordinate vector,

$$\mathbf{Z}(t) = (\xi(t), \xi(t - T_D), \xi(t - 2T_D), ..., \xi(t - MT_D)), \tag{3.1}$$

with a conveniently chosen delay time T_D and a sufficiently large M, is generically a global one-to-one representation of the system state $\mathbf{X}(t)$. Using a Poincarè surface of section, we obtain a set of discrete state variables $\mathbf{Z}_n = \mathbf{Z}(t_n)$, where $t = t_n$ denotes the time at the nth orbit crossing of the surface of section. As pointed out by Dressler and Nitsche[12], in the presence of parametric variation, delay coordinate embedding leads to a map which in general will depend on all parametric changes that were in effect in the time interval $t_n \leq t \leq t_n - MT_D$. The question which we address is the following: Given a chaotic system reconstructed from time delay coordinates, how can we incorporate dependencies of past parametric variations in a control scheme so that a desired attracting time-periodic motion can be attained. This problem was previously addressed by Dressler and Nitsche[12] for the case of a period one orbit of the Poincarè map in which there was a one-dimensional stable manifold and a one-dimensional

unstable manifold.

Similar to the control method originally purposed by Ott *et al.*[11], we wish to make only small controlling perturbations to the system. We do not envision creating new orbits with very different properties from the already existing orbits. Thus we seek to exploit the already existing unstable periodic orbits that are embedded in the chaotic attractor. Controlled chaotic systems offer an advantage in flexibility that any one of a number of different orbits can be stabilized by the small control, and the choice can be switched from one periodic orbit to another without drastically altering the system configuration. The present paper extends previous work[5] to the case when the future system state of a chaotic system depends on the current parametric variation as well as the previous parametric variations.

To numerically illustrate our method, we apply it to both a two dimensional example, the Ikeda map and a four dimensional example, the double rotor map. Physically, the Ikeda map describes the dynamics of a nonlinear optical cavity and the double rotor map describes a periodically forced mechanical system, the kicked double rotor. In the case of the Ikeda map, the stabilization is achieved by small variations of the amplitude of the light pulses entering the optical cavity. To control the double rotor map, stabilization is achieved by small variations of the strength of the periodic forcing.

3.2 Description of the Method

To be specific, we concentrate our discussion on a periodically forced system and use a stroboscopic surface of section, $t_n = nT_F + t_0$, where T_F is the forcing period. Assume that the orbit of this periodically forced system pierces the experimental surface of section r times in the time interval, $t_n < t \leq t_n - MT_D$, when the delay coordinate vector $\mathbf{Z}_n$ is being formed. Then, at the next piercing of the surface of section, the discrete state variable $\mathbf{Z}_{n+1}$ must depend not only on the current value of the forcing p_n, but also on the r previous forcings, $p_{n-1}, ..., p_{n-r}$. (We assume that the time-dependent parameter $p(t)$ is constant in each forcing period, $p(t) = p_n$ for $t_n \geq t > t_{n-1}$.) Thus, the relevant surface of section map will in general be of the following form,

$$\mathbf{Z}_{n+1} = \mathbf{G}(\mathbf{Z}_n, p_n, p_{n-1}, ..., p_{n-r}). \tag{3.2}$$

The most direct way to control a nontrivial period T orbit of the map is to take the Tth iterate of the map and apply the method developed in Sec. 2.6 of Ref.[5]. However, this method will be overly sensitive to noise, especially when long period periodic orbits are involved. The following is a method which we think in general will be better. Control is applied at each iterate of the map instead of each period T. This reduces the chance of the orbit being kicked out of the control region by noise while we are waiting for the orbit to cycle through the T periodic points.

Given a period T periodic orbit $\mathbf{Z}_n^*$ with $\mathbf{Z}_{n+T}^* = \mathbf{Z}_n^*$, and with $p(t) \equiv \bar{p}$ for all t, we can define the following set of $(d \times d)$-dimensional matrices, $\mathbf{A}_n$ and a collection of d-dimensional column vectors, $\mathbf{B}_n^1, ..., \mathbf{B}_n^{r+1}$, to describe the effect of small control parameter perturbations on the linear dynamics of the surface of section map Eq. (3.2) near the periodic orbit:

$$\mathbf{A}_n = \mathbf{A}_{n+T} = \mathbf{D}_{\mathbf{Z}}\mathbf{G}(\mathbf{Z}, p_n, p_{n-1}, ..., p_{n-r}), \tag{3.3}$$

$$\mathbf{B}_n^1 = \mathbf{B}_{n+T}^1 = \mathbf{D}_{p_n}\mathbf{G}(\mathbf{Z}, p_n, p_{n-1}, ..., p_{n-r}), \tag{3.4}$$

$$\mathbf{B}_n^2 = \mathbf{B}_{n+T}^2 = \mathbf{D}_{p_{n-1}}\mathbf{G}(\mathbf{Z}, p_n, p_{n-1}, ..., p_{n-r}), \tag{3.5}$$

$$\vdots$$

$$\mathbf{B}_n^{r+1} = \mathbf{B}_{n+T}^{r+1} = \mathbf{D}_{p_{n-r}}\mathbf{G}(\mathbf{Z}, p_n, p_{n-1}, ..., p_{n-r}). \tag{3.6}$$

The partial derivatives defined above are all evaluated at $\mathbf{Z} = \mathbf{Z}_n^*(\bar{p})$ and $p_n = p_{n-1} = ... = p_{n-r} = \bar{p}$ which is the unperturbed parameter value of the system. For values of p close to $\bar{p}$ and for $\mathbf{Z}_n$ close to the periodic orbit $\mathbf{Z}_n^*(\bar{p})$, the surface of section map Eq. (3.2) can then be approximated by its linearization,

$$\begin{aligned} \mathbf{Z}_{n+1} - \mathbf{Z}_{n+1}^*(\bar{p}) &= \mathbf{A}_n[\mathbf{Z}_n - \mathbf{Z}_n^*(\bar{p})] \\ &+ \mathbf{B}_n^1(p_n - \bar{p}) + \mathbf{B}_n^2(p_{n-1} - \bar{p}) \\ &+ ... + \mathbf{B}_n^{r+1}(p_{n-r} - \bar{p}). \end{aligned} \tag{3.7}$$

We emphasize that the location of the periodic orbit and the partial derivatives Eq. (3.3) can be obtained directly from experimental time series. In particular, the location of the periodic orbit and the associated Jacobians, $\mathbf{A}_n$, can be extracted from experimental time series using standard method described in Ref.[13, 14, 15, 16, 17, 18]. The collection of matrices, $\mathbf{B}_n^j, 1 \leq j \leq r+1$, which describes the variations of the map Eq. (3.2) with respect to the

different past parametric perturbations can also be obtained experimentally from time series generated by intermittently turning on the parametric perturbations, $\delta p = p - \bar{p}$, at each $(r+1)$th piercing of the surface of section, (i.e., $\delta p_n = \delta p_{max} \neq 0$ for every n divisible by $r+1$ and $\delta p_n = 0$ otherwise.) (We assume δp_{max} to be small enough that the linear approximation is valid.) The next step in finding the matrices $\mathbf{B}_n^j$ is to extract sequences of data points $\{\mathbf{Z}_n\}$ which are in the neighborhood of the periodic orbit $\mathbf{Z}_n^*$ (see Ref.[13]). Since we are keeping track of the history of the parametric perturbations, we can classify these sequence of data points into $r+1$ groups according to the time of the parametric perturbations with respect to n. As an example, let us consider all pairs of points $(\mathbf{Z}_n, \mathbf{Z}_{n+1})$ with $\delta p_n \neq 0$. (The other r groups of data pairs corresponds to cases with $\delta p_{n-1} \neq 0, ...,$ or $\delta p_{n-r} \neq 0$.) Since we have chosen $\delta p_{n-1} = ... = \delta p_{n-r} = 0$ for this data set, Eq. (3.7) reduces to the following form,

$$\mathbf{Z}_{n+1} - \mathbf{Z}_{n+1}^*(\bar{p}) = \mathbf{A}_n[\mathbf{Z}_n - \mathbf{Z}_n^*(\bar{p})] + \mathbf{B}_n^1 \delta p_n.$$

Then, the d-dimensional column vector $\mathbf{B}_n^1(\mathbf{Z}_n^*, \bar{p})$ can be estimated by least-square fitting the data pairs $(\mathbf{Z}_n, \mathbf{Z}_{n+1})$ to the above equation. The other $\mathbf{B}_n^j$, $2 \leq j \leq r+1$, can be obtained in a similar fashion using the other r groups of data pairs.

In order to take the dynamical dependence of past parametric variations in Eq. (3.2) into consideration of the control law, we first incorporate both the delay coordinate vector $\mathbf{Z}_n$ and the r past parametric values into a new $(d+r)$-dimensional state vector $\mathbf{Y}_n$,

$$\mathbf{Y}_n = \begin{pmatrix} \mathbf{Z}_n \\ p_{n-1} \\ p_{n-2} \\ \vdots \\ p_{n-r} \end{pmatrix}. \tag{3.8}$$

With this new $(d+r)$-dimensional state vector $\mathbf{Y}_n$, we can utilize Eq. (3.7) to obtain the following matrix equation for the linearized dynamics of the combined "state-plus-parameters" system,

$$\mathbf{Y}_{n+1} - \mathbf{Y}_{n+1}^*(\bar{p}) = \tilde{\mathbf{A}}_n[\mathbf{Y}_n - \mathbf{Y}_n^*(\bar{p})] + \tilde{\mathbf{B}}_n(p_n - \bar{p}), \tag{3.9}$$

where

$$\mathbf{Y}_n^* = \mathbf{Y}_{n+T}^* = \begin{pmatrix} \mathbf{Z}_n^*(\bar{p}) \\ \bar{p} \\ \vdots \\ \bar{p} \end{pmatrix}.$$

Here, the set of $(d+r)\times(d+r)$-dimensional matrices $\tilde{\mathbf{A}}_n$ and the set of $(d+r)$-dimensional column vectors $\tilde{\mathbf{B}}_n$ are defined in terms of the partial derivatives given in Eq. (3.3):

$$\tilde{\mathbf{A}}_n = \begin{pmatrix} \mathbf{A}_n & \mathbf{B}_n^2 & \mathbf{B}_n^3 & \cdots & \mathbf{B}_n^r & \mathbf{B}_n^{r+1} \\ \mathbf{0} & 0 & 0 & \cdots & 0 & 0 \\ \mathbf{0} & 1 & 0 & \cdots & 0 & 0 \\ \mathbf{0} & 0 & 1 & \cdots & 0 & 0 \\ \vdots & \vdots & \vdots & \vdots & \vdots & \vdots \\ \mathbf{0} & 0 & 0 & \cdots & 1 & 0 \end{pmatrix} \tag{3.10}$$

$$\tilde{\mathbf{B}}_n = \begin{pmatrix} \mathbf{B}_n^1 \\ 1 \\ 0 \\ \vdots \\ 0 \end{pmatrix} \tag{3.11}$$

where $\mathbf{0}$ is the d-dimensional row vector of zeros. Because of the periodicity of the partial derivatives Eq. (3.3), the $(d+r)\times(d+r)$-dimensional matrices $\tilde{\mathbf{A}}_n$ and the $(d+r)$-dimensional column vectors $\tilde{\mathbf{B}}_n$ are also periodic with a period T. One should note that this new "state-plus-parameters" dynamical equation reduces to the original linearized dynamics Eq. (3.7) if we consider only the first d components of Eq. (3.9). In particular, say that the periodic orbit $\mathbf{Z}_n^*$ is a saddle point with u unstable directions, s stable directions and $d = u + s$. Then, in this "state-plus-parameters" representation, the u-dimensional linearized unstable subspace $E_u(\mathbf{Y}_n^*)$ in $\Re^{(d+r)}$ is equivalent to the u-dimensional linearized unstable subspace $E_u(\mathbf{Z}_n^*)$ in $\Re^d$, while the $(s+r)$-dimensional linearized stable subspace $E_s(\mathbf{Y}_n^*)$ in $\Re^{(d+r)}$ is the direct sum of the equivalent s-dimensional linearized stable subspace $E_s(\mathbf{Z}_n^*)$ in $\Re^d$ and the r-dimensional null space of $\tilde{\mathbf{A}}_{n-1}\tilde{\mathbf{A}}_{n-2}\cdots\tilde{\mathbf{A}}_{n-T}$ in $\Re^{(d+r)}$.

The basic idea of our control algorithm is as follows. Given a periodic orbit, $\mathbf{Y}_n^* = \mathbf{Y}_{n+T}^*$, with period T and u unstable directions, we either wait for the system trajectory to come close to the control region (which we will define later) of the desired periodic orbit $\mathbf{Y}_n^*$, or we can use the various targeting techniques[19, 20, 21, 22] to bring the system trajectory near the control region of $\mathbf{Y}_n^*$. When the system state is in the control region, we will try to use u small parametric perturbations, $p_n, p_{n+1}, \cdots, p_{n+(u-1)}$, to control the u unstable directions of the combined "state-plus-parameters" dynamics. In other words, with the u parametric controls in u iterates, we attempt to bring the deviation, $\delta\mathbf{Y}_{n+u} = \mathbf{Y}_{n+u} - \mathbf{Y}_{n+u}^*$, to lie on the linearized stable subspace, $E_s(\mathbf{Y}_{n+u}^*)$, of $\tilde{\mathbf{A}}_{n+u-1}\tilde{\mathbf{A}}_{n+u-2}\cdots\tilde{\mathbf{A}}_{n+u-T}$. After this is accomplished, the control can be set to $\bar{p}$ and the orbit will naturally approach the desired periodic orbit.

To get an explicit expression for the control parameters, let us consider u iterates of Eq. (3.9),

$$\begin{aligned} \mathbf{Y}_{n+u} \quad - \quad & \mathbf{Y}_{n+u}^* = \mathbf{\Phi}_{n,0}[\mathbf{Y}_n - \mathbf{Y}_n^*] \\ + \quad & \mathbf{\Phi}_{n,1}\tilde{\mathbf{B}}_n(p_n - \bar{p}) + \mathbf{\Phi}_{n,2}\tilde{\mathbf{B}}_{n+1}(p_{n+1} - \bar{p}) \\ + \quad & \cdots + \tilde{\mathbf{B}}_{n+(u-1)}(p_{n+(u-1)} - \bar{p}), \end{aligned} \tag{3.12}$$

where

$$\mathbf{\Phi}_{n,j} = \tilde{\mathbf{A}}_{n+u-1}\tilde{\mathbf{A}}_{n+u-2}\cdots\tilde{\mathbf{A}}_{n+j+1}\tilde{\mathbf{A}}_{n+j}, \tag{3.13}$$

for $j = 1, 2, \cdots, (u-1)$, and $\mathbf{\Phi}_{n,u} \equiv \mathbf{I}$. We wish to place the deviation of the state vector, $\delta\mathbf{Y}_{n+u}$, on the linearized stable subspace $E_s(\mathbf{Y}_{n+u}^*)$ at $\mathbf{Y}_{n+u}^*$. Assuming that this is accomplished, there exist $(s+r)$ coefficients, $\alpha_1, \alpha_2, \cdots, \alpha_{s+r}$, such that

$$\begin{aligned} \mathbf{Y}_{n+u} \quad - \quad & \mathbf{Y}_{n+u}^* = \alpha_1\mathbf{v}_{n+u,1} + \alpha_2\mathbf{v}_{n+u,2} \\ + \quad & \cdots + \alpha_{s+r}\mathbf{v}_{n+u,s+r} \end{aligned} \tag{3.14}$$

where $\mathbf{v}_{n+u,1}, \mathbf{v}_{n+u,2}, \cdots, \mathbf{v}_{n+u,s+r}$ is any set of linearly independent unit vectors in $\Re^{d+r}$ which spans $E_s(\mathbf{Y}_{n+u}^*)$ (Recall that $E_s(\mathbf{Y}_{n+u}^*)$ is the sum of the linearized stable subspace of $\mathbf{Z}_{n+u}^*$ and an r-dimensional null space.) Combining Eq. (3.12) and (3.14), we then have $(d+r)$ equations with $(d+r)$ unknowns, $p_n, \cdots, p_{n+(u-1)}, \alpha_1, \cdots, \alpha_{s+r}$. This can be solved to obtain an expression for the required control parameter,

$$p_n = \bar{p} - \mathbf{K}_n^T[\mathbf{Y}_n - \mathbf{Y}_n^*] \tag{3.15}$$

where

$$\mathbf{K}_n^T = \kappa \mathbf{C}_n^{-1} \mathbf{\Phi}_{n,0}, \tag{3.16}$$

and κ denotes an $(d+r)$-dimensional row vector whose first entry is one and whose remaining entries are all zeros. The $(d+r) \times (d+r)$ dimensional matrix,

$$\begin{aligned} \mathbf{C}_n = (&\mathbf{\Phi}_{n,1}\tilde{\mathbf{B}}_n \vdots \mathbf{\Phi}_{n,2}\tilde{\mathbf{B}}_{n+1} \vdots \cdots \vdots \mathbf{\Phi}_{n,u-1}\tilde{\mathbf{B}}_{n+u-2} \\ &\vdots \tilde{\mathbf{B}}_{n+u-1} \vdots \mathbf{v}_{n+u,1} \vdots \mathbf{v}_{n+u,2} \vdots \cdots \vdots \mathbf{v}_{n+u,s+r}) \end{aligned} \tag{3.17}$$

is the "controllability" matrix with a similar meaning as in linear control theory such that the invertiblity of $\mathbf{C}_n$ implies the controllability of the periodic point $\mathbf{Y}_n^*$.

The construction of our control law Eq. (3.15) is based on the linearized Eq. (3.9) and in general we expect it to apply in the local neighborhood, $N(\mathbf{Y}_n^*)$, near $\mathbf{Y}_n^*$. On the other hand, since we envision applying only small parametric perturbations, $|p_n - \bar{p}| < \delta p_{max}$ in our control algorithm, we shall define the control region to be the set of all points $\mathbf{Y}_n$ within the slab,

$$\left|\mathbf{K}^T[\mathbf{Y}_n - \mathbf{Y}_n^*]\right| < \delta p_{max}. \tag{3.18}$$

For a given value of δp_{max}, the slab defined above intersects the local neighborhood $N(\mathbf{Y}_n^*)$ and its pre-images. Points in the local neighborhood $N(\mathbf{Y}_n^*)$ will in general be controlled by Eq. (3.15), and we expect that, under forward applications of the control law Eq. (3.15), points in the pre-images of $N(\mathbf{Y}_n^*)$ will eventually fall into the local neighborhood $N(\mathbf{Y}_n^*)$ and be controlled also. In our following numerical experiments, we have chosen to activate control according to Eq. (3.15) only when the values of $\mathbf{Y}_n$ are within the slab defined by Eq. (3.18) and the control parameter is left at its nominal value $\bar{p}$ otherwise. However, because of nonlinearity not included in the linearized Eq. (3.9), the control might not be able to bring the orbit to the desired periodic point for all points in the slab. In this case, the orbit will leave the slab and continue to wander chaotically as if there was no control. Since the orbit on the uncontrolled chaotic attractor is ergodic, after a chaotic transient[5], the orbit will once again enter the slab and may also be sufficiently close to $N(\mathbf{Y}_n^*)$ so that control is achieved.

In our derivation of the control law Eq. (3.15), although we only gave an explicit expression for the required parametric perturbation p_n at time n, we can, in principle, once and for all, solve for all the control parameter values to be applied in the next u iterates,

$p_n, p_{n+1}, \cdots, p_{n+u-1}$, from Eq. (3.12) and (3.14). In the presence of noise, however, this is not a good idea (assuming $u > 1$), since it does not take advantage of the opportunity to correct for the noise on each iterate. Therefore, we believe that, in the presence of noise, it is best to perform the calculation of p_n via Eq. (3.15) on each iterate.

In the paper by Dressler and Nitsche (see Ref.[12]), past parametric dependence ($r = 1$ in their work) in the dynamical equation using delay coordinates embedding introduces a possible instability in their proposed control laws. For certain instances, it is possible that the required perturbations δp_n will grow in time even when the system state is arbitrary close to the periodic orbit. This instability will eventually force the orbit to exit the control region. Their solution is to apply controls only at every other steps instead of at every step so that δp_n can be reset to zero every other step. This is equivalent to eliminating the term in the control law which depends on the previous parameter. By utilizing the stable subspace $E_s(\mathbf{Y}_n^*)$ of the combined "state-plus-parameters" system, the required perturbations in our control law are linearly related to the deviations of the system state $\mathbf{Y}_n$ from the periodic orbit $\mathbf{Y}_n^*$. Thus, the instability related to the blowing up of δp_n as in Dressler and Nitsche's method will not occur here.

3.3 Numerical Results

As a demonstration of our control method, we will use the Ikeda map as our first example. The Ikeda map describes the dynamics of a nonlinear optical cavity and is given by the following two dimensional map in state space,

$$\mathbf{X}_{n+1} = \begin{pmatrix} u_{n+1} \\ v_{n+1} \end{pmatrix} = \begin{pmatrix} a_n + 0.9(u_n \cos\ s_n - v_n \sin\ s_n) \\ 0.9(u_n \sin\ s_n + v_n \cos\ s_n) \end{pmatrix}, \tag{3.19}$$

where $s_n = 0.4 - 6.0/(1 + u_n^2 + v_n^2)$. The magnitude and angle of the complex quantity $u_n + iv_n$ defines the amplitude and phase of the nth light pulse inside the cavity and a_n is the amplitude of the light pulse entering the cavity at time n. We will be using a_n as our control parameter in this numerical example. (For a detailed physical description of this map, refer to Hammel *et al.*[23].) At the nominal value of $a_n = \bar{a} = 1$, this dynamical system possesses a chaotic attractor with a Lyapunov dimension of 1.71. Embedded in this attractor, we have chosen the

following three unstable periodic orbits for our numerical experiment[24],

$$\mathbf{X}^*_{p2} = (u^*_{p2}, v^*_{p2}) = \begin{cases} (0.50984, -0.60837) \\ (0.62160, 0.60593) \end{cases}$$

$$\mathbf{X}^*_{p3} = (u^*_{p3}, v^*_{p3}) = \begin{cases} (0.085797, -0.88323) \\ (0.77797, 0.76717) \\ (1.0140, -0.98324) \end{cases}$$

$$\mathbf{X}^*_{p5} = (u^*_{p5}, v^*_{p5}) = \begin{cases} (1.0447, 0.8002) \\ (1.4917, -1.0775) \\ (0.96244, -1.6557) \\ (0.39462, -1.6138) \\ (-0.22133, -0.86258) \end{cases} .$$

As indicated by their subscripts, $\mathbf{X}^*_{p2}, \mathbf{X}^*_{p3}$, and $\mathbf{X}^*_{p5}$, are periodic points of Eq. (3.19) with period $2, 3$, and 5 respectively.

To generate our time series $\{\xi_n\}$, we have chosen

$$\xi_n = u_n. \tag{3.20}$$

as our experimental output[1]. In this case, the dynamical equation in delay coordinates Eq. (3.2) depends on a_n as well as on a_{n-1} ($r = 1$ in this case). Since we know the exact map, Eq. (3.19), and the scalar output function Eq. (3.20), we can directly calculate the matrices $\mathbf{A}_n, \mathbf{B}^1_n$, and $\mathbf{B}^2_n$, appearing in Eq. (3.7). (As we have mentioned earlier, we can also obtain these matrices from time series using methods described in Ref. [13, 14, 15, 16, 17, 18]. There is a good description in Ref. [12] to calculate the matrices $\mathbf{B}^1_n$, and $\mathbf{B}^2_n$, explicitly from experimental time series.) Choosing the maximal allowed perturbation δa_{max} to be 0.01, Fig. 3.1 and 3.2 summarize our main results for the Ikeda map.

We plot the values of the scale output ξ_n as a function of time n in Fig.3.1a and we plot the applied parametric perturbations δp_n as a function of time n in the accompanying Fig.3.1b. In these figures, we turned on the control for the first periodic orbit $\mathbf{X}^*_{p2}$ at $n = 0$. After a chaotic transient (lasting until $n \cong 3700$), the orbit $\mathbf{X}^*_{p2}$ was stablized. Then, we successive switched

[1]Other linear combinations of u_n and v_n, e.g., $\xi_n = u_n + v_n$, were also considered. Results were similar as long as the controllability matrix C_n is not too close to being singular.

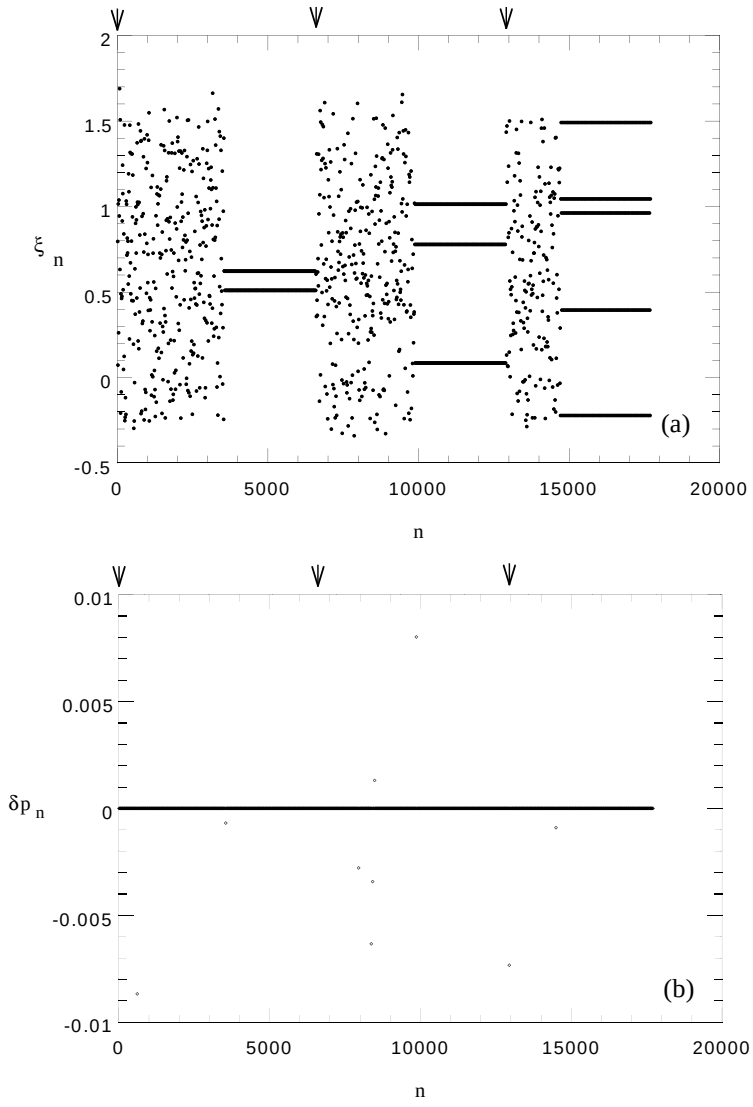

Figure 3.1: Ikeda map: successive control of periodic points $\mathbf{X}^*_{p2}, \mathbf{X}^*_{p3}$, and $\mathbf{X}^*_{p5}$. (a) ξ vs. n. (b) δp vs. n. The arrows indicate the times of switching. [$\bar{a} = 1$ and $\delta a_{max} = 0.01$]

our control to the other two periodic orbits $\mathbf{X}^*_{p3}$ and $\mathbf{X}^*_{p5}$. The times at which the control was switched so as to stablize $\mathbf{X}^*_{p3}$ and $\mathbf{X}^*_{p5}$ are indicated in the figure by arrows. In this figure, one can clearly see the flexibility offered by this method in controlling different periodic orbits embedded in a chaotic attractor reconstructed from time delay coordinates. Although the time to achieve control varied from case to case, in all cases, the parametric control was able to bring the orbit close to the desired periodic point within a couple thousands of iterations.

This brings us to the issue of chaotic transient between the time when control is activated and the time when control is achieved. To study the time to achieve control, we begin with a large number, $M_0 = 20000$, of random initial orbits uniformly chosen on the attractor and we calculate the number of orbits remaining uncontrolled, $M(n)$, as a function of time n. An orbit is considered to be under control when the required parametric perturbations δa_n remains within the range $[0, \delta a_{max}]$ for at least ten consecutive iterations. We expect the quantity $M(n)$ to decrease according to an exponential law,

$$M(n) = M_0 e^{n/<n>}, \tag{3.21}$$

where $< n >$ is the average time to achieve control[5]. In Fig.3.2a, the periodic orbit being controlled is $\mathbf{X}^*_{p5}$ and we have plotted $\ln(M(n)/M_0)$ (denoted by "+") as a function of n. From this graph, one can clearly see the expected exponential behavior for the time to achieve control. The slope of this graph gives the expected average time to achieved control, $< n >$, for a randomly chosen orbit on the attractor to be approximately 2500 iterations. To illustrate the effect of noise on this average time to achieve control, we plot three additional graphs, Fig.3.2b, 3.2c and 3.2d showing again $\ln(M(n)/M_0)$ vs. n for the cases where the output function Eq. (3.20) has an additional noise term,

$$\xi_n = u_n + \epsilon\delta_n \tag{3.22}$$

where δ_n is a random variable distributed uniformly between 0 and 1 and ϵ is the magnitude of the noise. Fig.3.2b shows data ("$\diamond$") with $\epsilon = 10^{-5}$, Fig.3.2c shows data ("$\circ$") with $\epsilon = 10^{-4}$ and Fig.3.2d shows data ("$\triangle$") with $\epsilon = 10^{-3}$. In these graphs, we can see that except for the case when $\epsilon = 10^{-3}$ ("$\triangle$"), all other three data sets: "+", "$\diamond$", and "$\circ$", within expected errors, gives the same average time to achieve control. The much slower convergence and the non-exponential behavior exhibited in the case with $\epsilon = 10^{-3}$ indicates that the noise is

large enough so that many probably controllable orbits are being kicked away from the control region by noise.

To appreciate the importance of past parametric consideration in controlling systems using delay time coordinates, we now blindly assume that the surface of section map Eq. (3.2) depends only on the current parametric perturbation. Then, the required control parametric perturbation δa_n, for the Ikeda map in delay time coordinates with the output function given by $\xi_n = u_n$, would be

$$a_n - \bar{a} = -(1\ 0)[\mathbf{B}_n^1 \vdots \mathbf{v}_n^s]^{-1}\mathbf{A}_n[\mathbf{Z}_n - \mathbf{Z}_n^*], \tag{3.23}$$

where the two dimensional column vector $\mathbf{B}_n^1$ and the two dimensional matrix $\mathbf{A}_n$ are defined as in Eq. (3.3), $\mathbf{v}_n^s$ is the stable eigenvector of $\mathbf{A}_n\mathbf{A}_{n-1}\cdots\mathbf{A}_{n-(T-1)}$, and the delay vector $\mathbf{Z}_n$ equals to $(\xi_n, \xi_{n-1}) = (u_n, u_{n-1})$. Figure 3.3 shows a section of the history of ξ_n for the two control methods: (a) Eq. (3.15) and (b) Eq. (3.23). In both cases, all parameters in the dynamical system were the same and we started the procedures with the same initial condition. The initial condition was chosen such that the initial orbit was within a distance of 10^{-4} away from the desired periodic orbit $\mathbf{X}_{p5}^*$. While our control method was able to further decrease the measured deviation $\xi_n - \xi_n^*$ down to the machine accuracy ($\approx 10^{-15}$), the control method without past parametric consideration was not able to stabilize the orbit. This result tells us that in typical cases when delay time coordinates are involved, parametric control methods must take past parametric dependencies into consideration.

To demonstrate our method in a high dimensional system, we will apply it to a periodically kicked mechanical system known as the kicked double rotor[5]. On the "stroboscopic surface of section," this mechanical system can be represented in state space by a four dimensional map in the following form,

$$\mathbf{X}_{n+1} = \begin{pmatrix} \mathbf{\Theta}_{n+1} \\ \dot{\mathbf{\Theta}}_{n+1} \end{pmatrix} = \begin{pmatrix} \mathbf{W}_1\dot{\mathbf{\Theta}}_n + \mathbf{\Theta}_n \\ \mathbf{W}_2\dot{\mathbf{\Theta}}_n + f_n\mathbf{H}(\mathbf{\Theta}_{n+1}) \end{pmatrix}, \tag{3.24}$$

where $\mathbf{\Theta} = (\theta^1, \theta^2)^T$ are the two angular position coordinates, $\dot{\mathbf{\Theta}} = (\dot{\theta}^1, \dot{\theta}^2)^T$ are the corresponding angular velocities, and $\mathbf{H}(\mathbf{\Theta})$ is a nonlinear function. $\mathbf{W}_1$ and $\mathbf{W}_2$ are two constant matrices defined by the friction coefficients and moments of inertia of the rotor. We take as the control parameter of this system the strength of the kick f_n. Setting the nominal value of

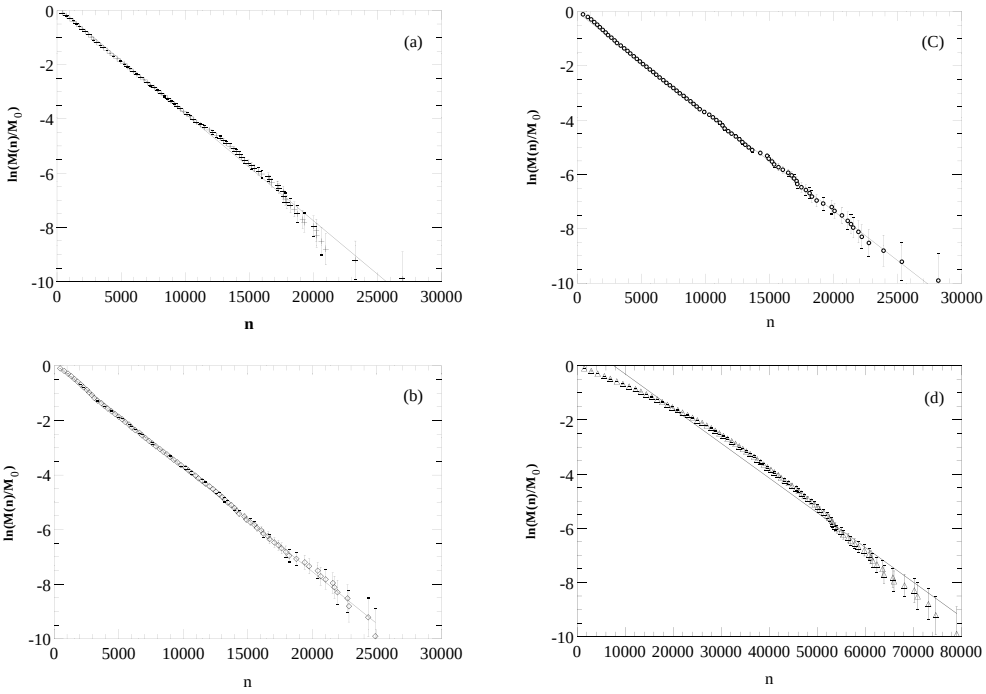

Figure 3.2: Ikeda map: The natural logarithm of the fraction of uncontrolled orbits verse time. A sample of 20000 initial orbits were chosen randomly over the attractor. An orbit is said to be controlled if $0 < \delta a_n < \delta a_{max}$ for at least 10 consecutive iterations. The periodic point controlled is $\mathbf{X}^*_{p5}$. (a) "+" denotes data calculated with $\epsilon = 0$, (b) "$\diamond$" denotes data calculated with $\epsilon = 10^{-5}$, (c) "$\circ$" denotes data calculated with $\epsilon = 10^{-4}$ (d) "$\triangle$" denotes data calculated with $\epsilon = 10^{-3}$.

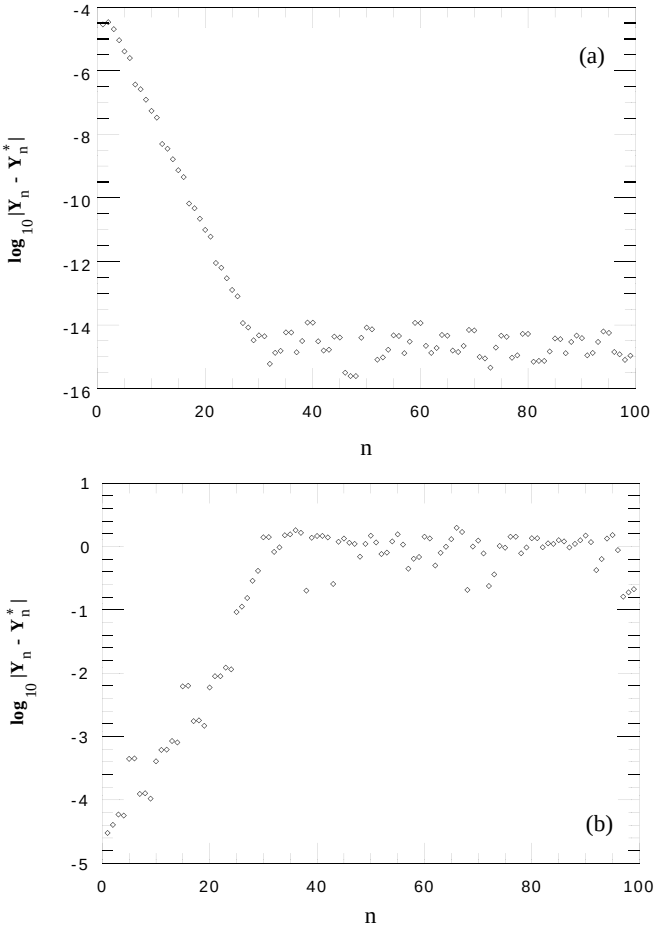

Figure 3.3: Ikeda map: $\log_{10}|\mathbf{Y}_n - \mathbf{Y}_n^*|$ vs. n. The periodic orbit being controlled is $\mathbf{X}_{p5}^*$. Test orbit was initialized within a radius of 10^{-4} away from the periodic point. (a) Control method introduced in this paper. (b) Control method without past parametric consideration.

f_n to $\bar{f} = 9$ and the other parameters of the system to the ones in Ref.[5], the system processes a chaotic attractor with a Laypunov dimension of 2.838. To generate a scalar time series $\{\xi_n\}$, we will use,

$$\xi_n = \theta_n^1. \tag{3.25}$$

With the choice of this output function, the corresponding dynamical equation in delay time coordinates Eq. (3.2) will depend on δf_n as well as on the three past parametric perturbations: $\delta f_{n-1}, \delta f_{n-2}$, and δf_{n-3} where $\delta f_n = f_n - \bar{f}$ ($r = 3$ in this case). The unstable periodic orbit

$$\mathbf{X}_R^* = (\theta_1^*, \theta_2^*, \dot{\theta}_1^*, \dot{\theta}_2^*) = \begin{cases} (3.1402, 0.48105, -2.0364, 0.74249) \\ (2.3090, 0.56580, 4.4182, 4.6514) \\ (-0.83474, -1.5220, -2.3818, -5.3938) \end{cases} \tag{3.26}$$

which we are attempting to control, is a period 3 orbit embedded in the attractor and it has two unstable directions and two stable directions. In our control algorithm, we have set the maximum allowed parameter perturbation δf_{max} to be 1×10^{-4}. Figure 3.4 shows a history of the observed scalar output from the map as a function of time n. At time $n = 0$, the orbit first enters a neighborhood of radius 10^{-4} around the periodic point $\mathbf{X}_R^*$ and parametric control is activated at this time. One can see that the orbit quickly converges to the desired periodic orbit as n increases. As indicated by the small size of the neighborhood within which the orbit converges, we expected the average time to achieve control in this case to be quite large (on the order of 10^{12} iterations). This decrease in the size of the controllable region is mainly the consequence of using delay time embedding. In general, to uniquely determine a state of the system, we need to wait at least d iterations (d is the dimension of the system) to form the delay vector. Thus, even if the orbit is at a distance δ away from the periodic orbit at time n, the orbit will be at a distance of $\Lambda^d \delta$ away from the periodic orbit when the orbit can be represented uniquely by the delay vector. (Here, Λ is the largest multiplier of the periodic point.) Thus, typically, we should expect the size of the controllable region in delay time coordinates to be a factor of $(1/\Lambda)^d$ times smaller than the controllable region in regular state space coordinates. This effect will become more evident in higher dimensional systems. With this long chaotic transient time, we believe that some kind of targeting techniques [19, 20, 21, 22] will be essential in controlling these high dimensional systems in delay time coordinates.

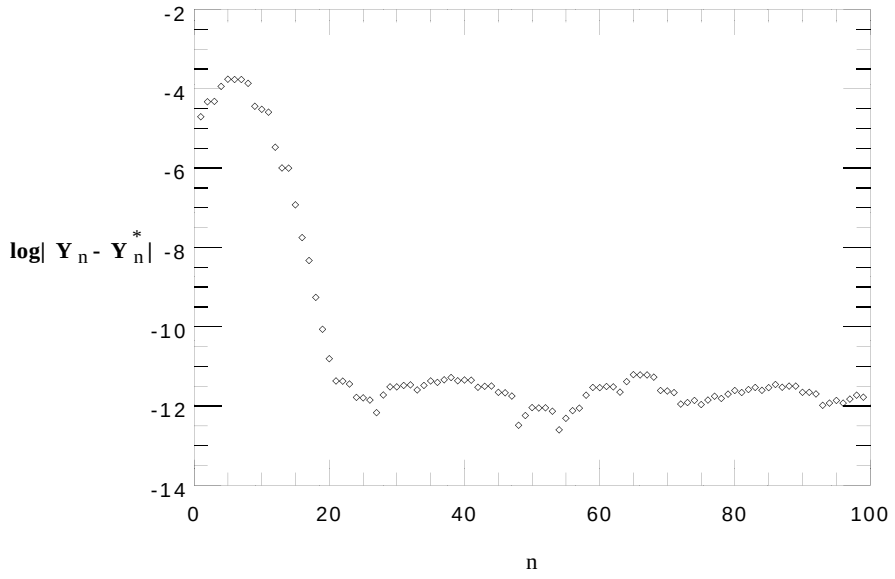

Figure 3.4: Rotor map: $\log_{10}|\mathbf{Y}_n - \mathbf{Y}_n^*|$ vs. n. The periodic orbit being controlled is $\mathbf{X}_R^*$. Parametric control is activated at $n = 0$. [$\bar{f} = 9$ and $\delta f_{max} = 0.1$]

3.4 Conclusion

In this paper, we have presented a method for control of chaotic systems using time delay coordinates. To take the dynamical dependence of past parameters into consideration, our parametric control law is constructed based on the combined dynamics of the "state-plus-parameters" system. In our numerical example using delay time coordinates, we have found that parametric control of unstable periodic points can only be achieved if we take past parametric perturbations into consideration (except the case when past parametric dependencies are absent from the dynamical equation[2]). We found that our method is efficient in controlling and flexible in switching among different unstable periodic points embedded in an attractor of low dimension (Ikeda map). However, while the method is able to control unstable periodic point embedded in a higher dimensional attractor (double rotor map), the chaotic transient time required for the orbit to come near the control region will in general be unacceptably long. While progress is being made in controlling high dimensional systems[25], we believe that targeting and multivariant control[26] (using more than one control parameter) are two key issues in developing control schemes for high dimensional systems with delay time coordinates.

[2]These include the numerous successful implementations of the original OGY method in controlling various experimental time series (see Ref. [29, 30, 31, 32, 33, 34, 35, 36]). In these examples, the relevant dynamics can in general be described by one dimensional return maps which are insensitive to past parametric variations.

Chapter 4

Wave Chaos Statistics

4.1 Introduction

Given a wave equation, the study of wave chaos explores the relation between the behavior of its short wavelength solutions and the solutions of its corresponding ray equations. The corresponding physical system of the wave equation may be electromagnetic, acoustic, or quantum. An example is the quantum wave equation. In this case, the short wavelength behavior is described by solutions to the Schrödinger's equation in the semi-classical limit and the ray solutions are simply the corresponding classical orbits. In particular, we are interested in the quantum manifestations of classically *chaotic* systems in the semi-classical regime. For chaotic systems in the semi-classical limit, it has been conjectured that, the spectral statistics of the Schrödinger equation correspond to that of random matrices with the same symmetry[37, 38]. To be specific, when the system is time reversible, the statistical fluctuations of the energy levels are conjectured to be the same as those for the "Gaussian Orthogonal Ensemble" of random matrices (GOE). As a simple example of this class of systems, consider a charged particle in a scalar potential. By reversing the direction of the momentum of the particle, the classical particle will retrace it own path (see Fig. (4.1)). The wave equation for this particle is real and the corresponding "Gaussian Orthogonal Ensemble" consists of real random symmetric matrices. On the other hand, when a magnetic field $\mathbf{B}$ is applied, the time-reversal symmetry is broken. A classical charged particle will no longer retrace its own path when the direction of its momentum is reversed (see Fig. (4.1)). In this case, the Schrödinger equation is complex, $\mathbf{p} \rightarrow -i\hbar\boldsymbol{\nabla} - q\mathbf{A}(\mathbf{r})$, and (in the absence of special symmetries) the

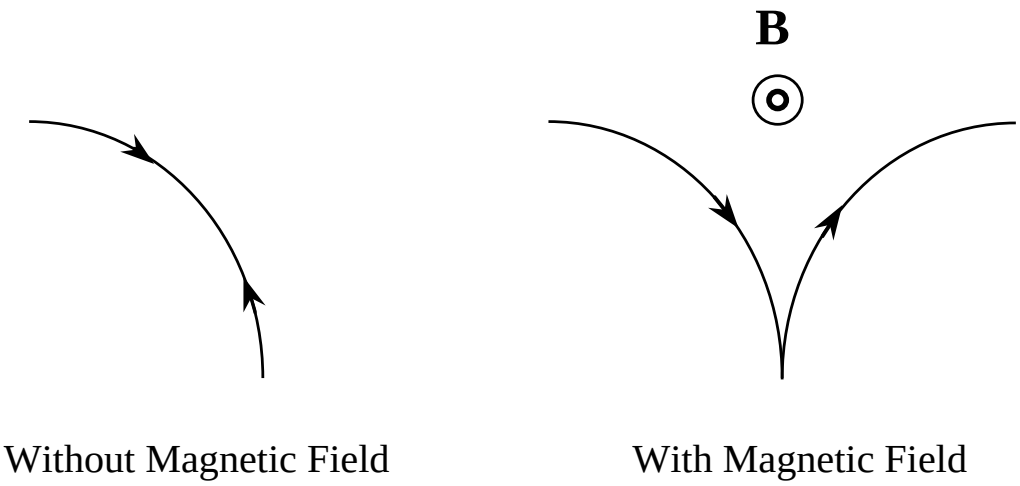

Figure 4.1: Trajectory of a charged particle in free space and in a static magnetic field **B**.

statistical fluctuations of the energy levels are conjectured to be the same as those for the "Gaussian Unitary Ensemble" of random hermitian matrices (GUE)[1]. While the predictions of GOE statistics in actual physical systems have been observed by others[39, 40, 41, 42], the first experimental verification of the GUE predictions was not reported until So *et al.*[43]. Here, we present an extended version of our findings using a two-dimensional microwave cavity with a thin magnetized ferrite strip adjacent to one of the walls. As we will show later, this microwave system is in the same universality class (GUE) as the corresponding quantum system without time reversal symmetry.

[1]In addition to GOE and GUE statistics, there is a third type of ensemble called "Gaussian Symplectic Ensemble" (GSE) which applies to systems with Kramers' degeneracy and without geometric symmetries.

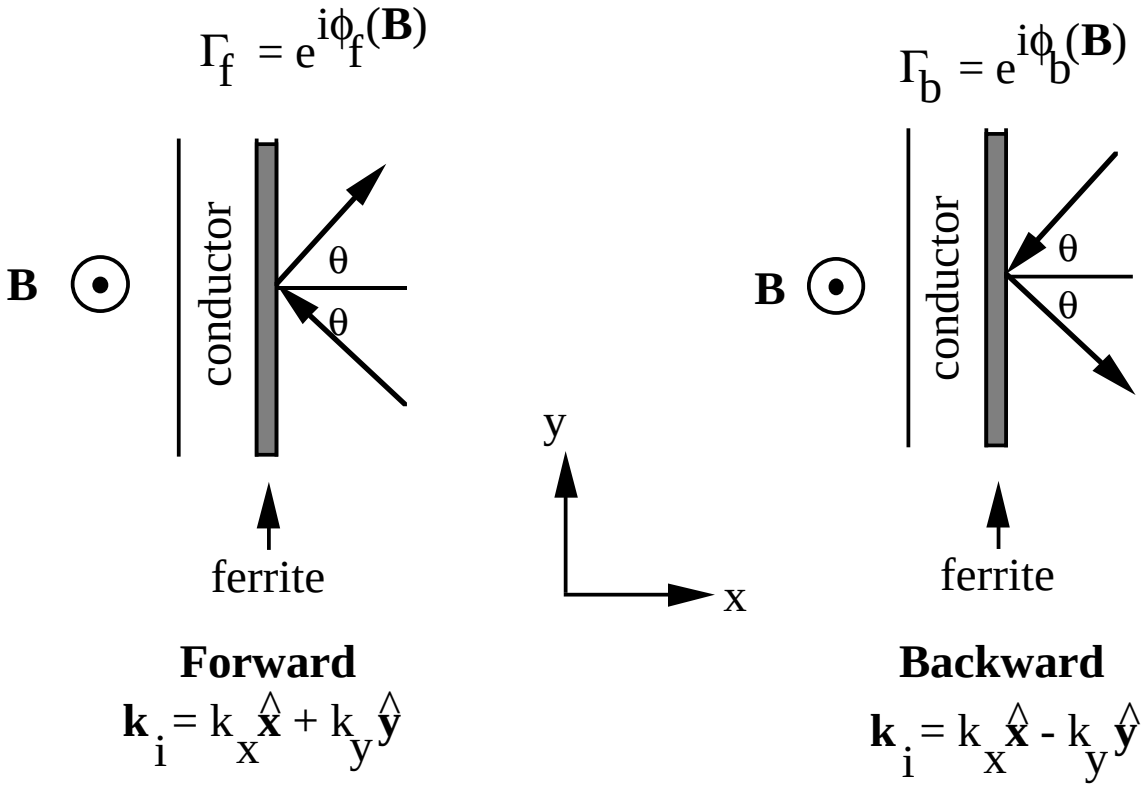

Figure 4.2: The phase of the reflection coefficient for a incident plane wave on a ferrite with a given angle of incidence θ is different for the two situations shown.

4.2 Two Dimensional Microwave Cavity with Magnetized Ferrite

To see how a magnetized ferrite breaks the time reversal symmetry in the electromagnetic wave equation, consider the situation (see Fig. (4.2)) when a plane wave with the electric field $\mathbf{E} = E_z \exp^{(ik_x x + ik_y y)} \hat{\mathbf{z}}$ perpendicular to the plane of incidence is incident from the right ($x > 0$) on a slab of magnetized ferrite ($0 > x > \delta$) which is placed adjacent to a perfect conductor on the right ($x = \delta$). In the presence of a static magnetic field $\mathbf{B} = B\hat{\mathbf{z}}$ perpendicular to the plane of incidence, the magnetic permeability matrix μ of the ferrite, in the absence of losses, is

$$\mu = \begin{bmatrix} \mu_\parallel & -i\kappa & 0 \\ i\kappa & \mu_\parallel & 0 \\ 0 & 0 & \mu_z \end{bmatrix}, \tag{4.1}$$

where $\mu_\parallel$, κ, and μ_z are real quantities and are functions of the static magnetic field B. At the interface between the ferrite and the empty cavity, the boundary conditions require the continuity of both E_z and the tangential component of $\mathbf{H}$, which, in the ferrite, is proportional to $(\mu_\parallel \frac{\partial E_z}{\partial x} + i\kappa \frac{\partial E_z}{\partial y})$. One can then calculate the reflection coefficient $\Gamma = \exp^{i\phi(B)}$ of this plane wave:

$$\begin{aligned} \phi &= 2k_x\delta + \frac{\alpha + i\beta}{\alpha - i\beta}, \\ \alpha &= \frac{k_x}{\mu_\parallel k_x^f \cos(k_x^f \delta) - \kappa k_y \sin(k_x^f \delta)}, \\ \beta &= \frac{1}{\sin(k_x^f \delta)}, \end{aligned} \tag{4.2}$$

where k_x^f is the x-component of the wavenumber inside the ferrite and δ is the thickness of the ferrite[2]. For simplicity, the B dependence of the phase ϕ is implicit in the two quantities $\mu_\parallel$ and κ. One can see from Eq. (4.2) that upon reversal of the direction of the incident wave (i.e., $k_y \to -k_y$), because of the linear term in k_y, the phase $\phi(B)$ is different. That is, unlike the situation with $B = 0$, for the same magnitude of the angle of incidence, the phase shift changes, $\phi(B, k_y) \neq \phi(B, -k_y)$ if $B \neq 0$. Thus, time-reversal symmetry in this electromagnetic system is broken by the static magnetic field $\mathbf{B}$.

These experiments are pertinent to quantum chaos because the electromagnetic wave equation in a thin microwave cavity with magnetized ferrite is in the same universality class (GUE) as the Schrödinger equation without time reversal symmetry. To be specific, in the presence of a time independent applied magnetic field $\mathbf{B}_f = \nabla \times \mathbf{A}$ with the coulomb gauge ($\nabla \cdot \mathbf{A} = 0$), the Schrödinger equation for a particle of mass m and charge q with wavefunction $\psi(x, y)$ in the xy-plane is

$$\nabla^2\psi - 2(iq/\hbar)\mathbf{A} \cdot \nabla\psi + (2m/\hbar^2)[E - (q^2/2m)\mathbf{A}^2]\psi = 0 \tag{4.3}$$

with $\psi = 0$ on the boundary. (This $\mathbf{B}_f$ should not be confused with the static magnetic field $\mathbf{B}$ used to magnetize the ferrite strip.) Eq. (4.3) should be compared with the following

[2]If we consider energy loss in the ferrite, α and β in Eq. 4.2 will be complex.

electromagnetic wave equation in the microwave cavity with magnetized ferrite,

$$\nabla \cdot \left[(1+\mu_{\|})\nabla E_z\right] - i(\hat{\mathbf{z}} \times \nabla\kappa) \cdot \nabla E_z + k^2 E_z = 0 \tag{4.4}$$

with $E_z = 0$ on the boundary and $k^2 = (2\pi f)^2/c^2$. In the case, with $\nabla\mu_{\|} = 0$, Eq. (4.3) and Eq. (4.4) give the same eigenvalue equation[3] if one identifies E_z with ψ and, up to constant factors, $\mathbf{B}_f$ with $\hat{\mathbf{z}}\nabla^2\kappa$. In our experiment, κ changes discontinuously from zero in the empty region of the cavity to its value inside the ferrite strip. Thus, the magnetic field $\mathbf{B}_f$ in the analogous Schrödinger problem is a "double layer" (i.e., the derivative of a delta function on the surface of the ferrite). Even with this rather singular magnetic field, the analogy to the Schrödinger equation is still not perfect in the experiment because $\mu_{\|}$ also changes discontinuously crossing the ferrite boundary. Nevertheless, the relevant point is that the magnetized ferrite problem and the magnetized Schrödinger problem are in the same (GUE) universality class.

The geometry of our microwave cavity is shown in the inset of Fig. (4.3) where the curved boundaries are circular arcs. In this geometry, all typical ray-trajectory orbits are chaotic and all periodic orbits are isolated. (Thus, there are no "bouncing-ball modes" as in the stadium billiard or the Sinai billiard. Previous work has shown that these bouncing-ball modes lead to deviations from the Random Matrix predictions[41, 44, 45].)

The microwave signal is coupled to the cavity electrically through four very small holes drilled in the top plate of the cavity. The coupling is chosen to be as weak as possible so that shifting and broadening of the cavity frequency resonances due to the coupling is minimized. The eigenmodes of the cavity are measured using an HP 8510C vector network analyzer by locating resonance peaks in the transmission spectra between pairs chosen from the four small holes. Since the thickness of our cavity is $d = 0.3125$ in, we could, in principle, perform our frequency sweep up to $f_{max} = c/(2d) \sim 18.9$ GHz while ensuring that the eigenmodes obtained correspond only to the two-dimensional TM modes of the cavity. However, in practice, due

[3]In the absence of the ferrite strip, the microwave cavity system and the quantum mechanical billiard system in two dimensions are both described by the same Helmholtz equation [i.e., $(\nabla^2 + k^2)\Psi = 0$, where $\Psi = E_z$ and $k = 2\pi f/c$ in the electromagnetic case and $\Psi = \psi$ and $k^2 = (2mE/\hbar^2)$ in the quantum mechanical case] with $\Psi = 0$ on the boundary.

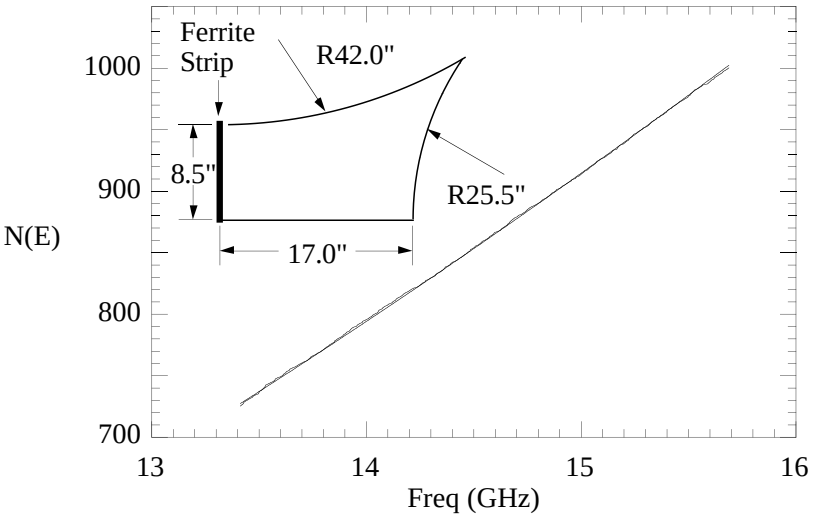

Figure 4.3: Experimental cumulative level density $N(E)$ vs. $f(E = (2\pi f/c)^2)$ in the case when the ferrite is magnetized. The theoretical curve for the smooth monotonic part $N_0(E)$ is superimposed on top. The inset shows the geometry of our microwave cavity.

to the finite Q of the cavity[4] (on the order of several thousand), we found that we could only reliably identify resonance peaks up to approximately 16 GHz. Furthermore, since we are interested in the semi-classical behavior of the system, our experiment will examine the spacing statistics of eigenmodes in the regime where the wavelength is small compared to the cavity size. Correspondingly, in our experiment, we only consider frequencies above 7 GHz, which corresponds to mode numbers above $\sim$200. Within this frequency range, we could identify up to 800 eigenmodes. In studying the GUE statistics, however, it is necessary to consider smaller frequency ranges since the ferrite properties are strongly frequency dependent, and κ in Eq. (4.2) may not be sufficiently large to achieve full GUE statistics far from the gyromagnetic resonant frequency of the ferrite. In general, we expect that the phase difference, $\Delta\phi(B) = |\phi(B, k_y) - \phi(B, -k_y)|$, between the forward going and backward going wave to be large enough to yield GUE statistics when it is at least two orders of magnitude greater than $\Delta k\lambda$, where Δk is the average spacing between modes in k-space and λ is the wavelength of a given eigenmode. (Note that, $\Delta k\lambda \to 0$ as the mode number goes to infinity. Thus, in this limit, the transition from GOE to GUE occurs abruptly for any $|B| > 0$. On the other hand, the transition is continuous when the mode number is finite[46, 47, 48, 49, 50].) Using the values of the ferrite parameters supplied by the manufacturer[51], we plotted in Fig. (4.4) the ratio between $\Delta\phi$ and $\Delta k\lambda$ over the frequency range of interest and we found that only data from the upper range (13.5 - 16 GHz) of our operating frequency span provides sufficiently large phase difference $\Delta\phi$ for GUE statistics. This poses a limit on the number of energy levels ($\sim$ 260) which we used in calculating the GUE statistics. Despite this limitation, we will show below that the quantitative difference between GOE and GUE statistics for the cases with and without magnetic field can still be unambiguously observed.

In our experiment, the magnetic field is provided by a series of Nd-Fe-B magnets placed on both the top and the bottom plates of the cavity in an attracting position. These magnets are able to produce a field of approximately 2500 Gauss in a one inch air gap. In general, the time-irreversibility increases with the saturation magnetization of the ferrite. In our experiment,

[4]Although the ferrite is a lossy material compared to a good conductor like copper, its degradation of the Q factor of the cavity near the gyromagnetic resonance remains relatively small because of the small volume of ferrite employed.

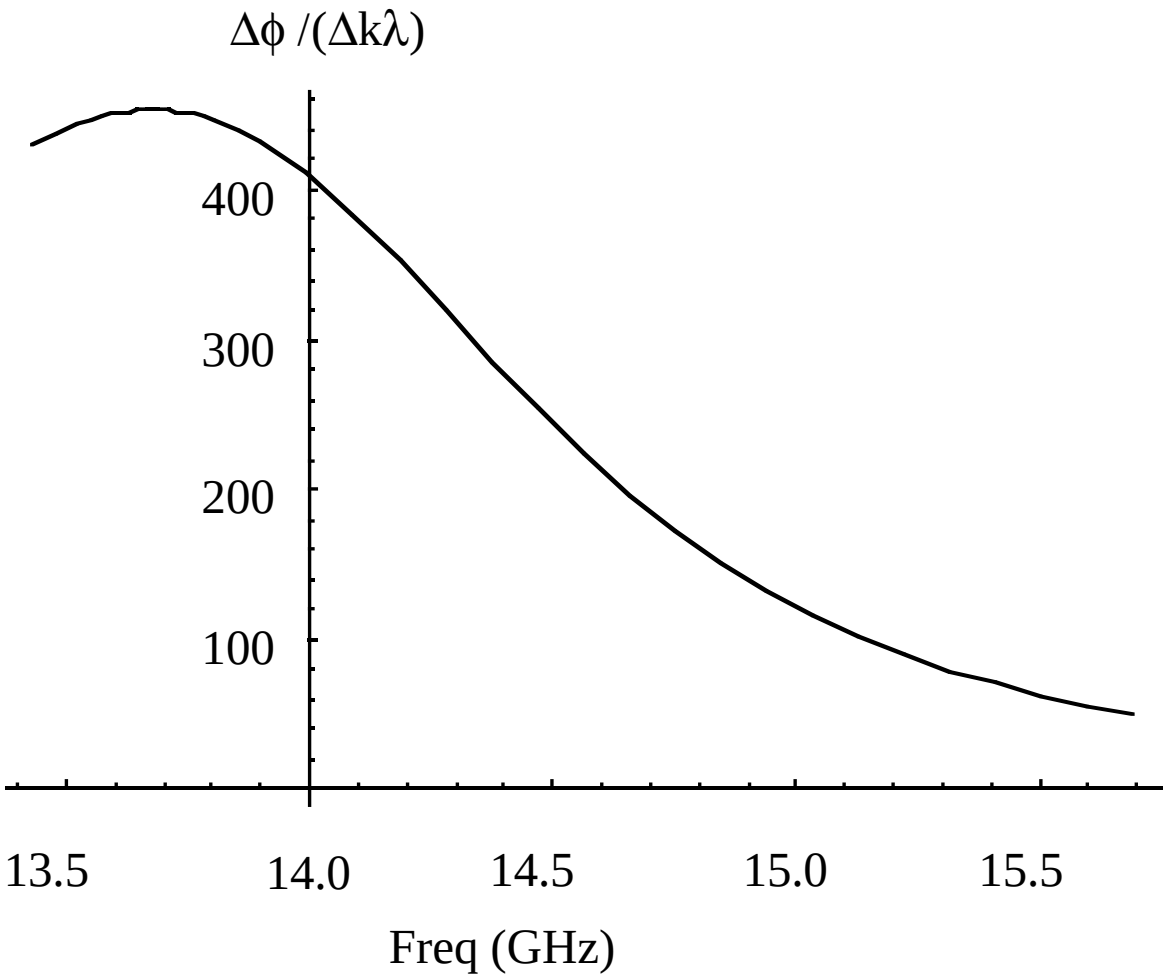

Figure 4.4: The ratio between $\Delta\phi$ and $\Delta k\lambda$ as a function of frequency. Note that $\Delta\phi$ is $\approx 10^2$ times larger than $\Delta k\lambda$ in the frequency range approximately between 13 and 16 GHz.

we have chosen a ferrite with a relatively high saturation magnetization ($4\pi M_s = 1850$ Gauss) and a comparatively small resonance absorption, which is characterized by its resonance line width ($\Delta H = 14$ Oe). We note that the degree of time irreversibility can be adjusted by controlling the amount of the ferrite in the cavity, by changing the magnitude of the applied magnetic field, or by analyzing the data along different frequency windows of a fixed span. In this chapter, we will emphasize our experimental results with pure GUE statistics and the GOE-GUE transition using different frequency windows of a fixed span.

4.3 Wave Chaos Statistics

As the first step in examining the spectral statistics of a given set of energy levels $\{E_i\}$, we construct the cumulative level density of states $N(E)$, which gives the number of "energy levels" with energy less than E (we identify E with $k^2 = (2\pi f)^2/c^2$ where f is the cavity resonant frequency). From a semi-classical calculation, this "staircase" function consists of a smooth monotonic part and a fluctuating part,

$$N(E) = N_0(E) + N_{fluc}(E). \tag{4.5}$$

The smooth monotonic part, $N_0(E)$ is given by[52, 53],

$$N_0(E) = C_1 E + C_2 E^{1/2} + O(E^0). \tag{4.6}$$

In the case of the empty cavity without ferrite, $C_1 = A/4\pi$ where A is the cross-sectional area of the cavity; C_2 depends on the cavity boundary conditions: $C_2 = L/4\pi$ for Neumann boundary conditions and $C_2 = -L/4\pi$ for Dirichlet boundary conditions, where L is the perimeter of the cavity. In the semi-classical regime ($N_0(E) \gg 1$), one should note that the first term, $C_1 E$, is large compared to the second term. Thus, for large E, $N(E)$ is approximately linear in E. Figure 4.3 is a graph of the experimental $N(E)$ as a function of f in the range between 13 and 16 GHz for the case when the ferrite is magnetized by the applied magnetic field. We have also plotted $N_0(E)$ as a solid curve in which we use $C_2 = -L/4\pi$ and an area A that is 5% larger than the physical area of the cavity. This area increase is meant to roughly account for the increased wavenumber in the ferrite: in the relevant frequency range, $k_f \delta / kb$. Here, k_f is the wavenumber in the ferrite calculated using the parameter values provided by the

manufacturer; k is the vacuum wavenumber; δ is the ferrite thickness (0.09 inches); and b is the horizontal length of the cavity (17 inches; see inset of Fig. 4.3).

The fluctuating part, $N_{fluc}(E)$, contains universal behavior which depends only on the symmetry class of the system. To examine these universal features, one makes a change of variables using $e = N_0(E)$, and defines the "unfolded" cumulative energy density as $\hat{N}(e) \equiv N(E)$. Random Matrix Theory provides statistical predictions of the fluctuations of a properly unfolded energy spectrum. In particular, we consider the *spectral rigidity* $\Delta(L)$ and the *level spacing distribution* $P(s)$.

The spectral rigidity, $\Delta(L)$ is defined as follows[54, 55]. Within a given segment of the unfolded spectrum of length L centered at e, one least square fits a straight line to this section of the staircase function $\hat{N}(e)$. Then, the local spectral rigidity $\Delta(e; L)$ is defined as the mean least squared deviation from this best fitted line over the range L. When the spectrum is properly unfolded, $\Delta(e; L)$ is a function independent of the unfolded energy e. $\Delta(L)$ is then evaluated by taking the average over many non-overlapping adjacent segments of length L of the spectrum. Physically, one can interpret the spectral rigidity to be a measure of the long range fluctuations in the energy spectrum. In functional form, the spectral rigidity is defined as

$$\Delta(L) = \langle \Delta(e; L) \rangle = \langle \frac{1}{L} \min_{A,B} \int_e^{e+L} \left[\hat{N}(x) - Ax - B \right]^2 dx \rangle \tag{4.7}$$

where $\langle . \rangle$ indicates the average taken oven many non-overlapping adjacent segments of the spectrum. While the spectral rigidity, $\Delta(L)$, tends to zero as $L \to 0$ for all symmetry classes, it has different logarithmic behavior for different symmetry classes for $L \gg 1$:

$$\Delta_{GOE}(L) = \frac{1}{\pi^2}(\ln(2\pi L) + \gamma - \frac{5}{4} - \frac{\pi^2}{8}) + O(1/L), \tag{4.8}$$

$$\Delta_{GUE}(L) = \frac{1}{2\pi^2}(\ln(2\pi L) + \gamma - \frac{5}{4} + O(1/L), \tag{4.9}$$

where γ is the Euler's constant. One can say that the spectrum of a time irreversible system (GUE) is more rigid in the sense that its fluctuations about its average are smaller than those for the time reversible case (GOE).

Now, we turn to the level spacing distribution $P(s)$. By definition, $P(s)ds$ is the frenquency of finding a given energy separation, $s_i = e_{i+1} - e_i$, in the range $s \leq s_i \leq s + ds$. In two dimensions, depending on the system's symmetry class, time reversible (GOE) or time

irreversible (GUE), the level spacing distribution $P(s)$ is given by the following equations respectively,

$$P_{GOE}(s) \simeq s\frac{\pi}{2}\exp^{-s^2\frac{\pi}{4}}, \tag{4.10}$$

$$P_{GUE}(s) \simeq s^2\frac{32}{\pi^2}\exp^{-s^2\frac{4}{\pi}}. \tag{4.11}$$

As the above equations suggested, the energy spectrum of a classically chaotic quantum system shows the unique behavior of "level repulsion" (i.e., $P(0) = 0$). In contrast with integrable systems, whose energy levels tend to cluster, the probability density for finding levels with zero spacing is zero in chaotic systems, and the degrees of this level repulsion (i.e., the behavior of $P(s)$ as $s \to 0$) depend on the symmetry class of the system. For the purposes of analysizing our level spacing data, we avoid using a histogram (which, due to our small number of levels, has large statistical fluctuations,) by considering the integral $I(s) = \int_0^s P(s)ds$ rather than $P(s)$ itself. This allow us to estimate $I(s)$ from our data by simply counting the number of level spacings less than s, and dividing by the total number of spacings. The most interesting range is for small s where the level repulsion phenomena are distinctly different for GOE and GUE. In particular, the small s behavior is either quadratic or cubic: $I(s) \simeq (\pi/4)s^2$ for GOE and $I(s) \simeq [32/(3\pi^2)]s^3$ for GUE.

4.4 Spectral Statistics from the Experimental Microwave Cavity with Magnetized Ferrite

Two sequences of markers indicating the location of the observed cavity resonant frequencies from a section of our experimental transmission spectrum are shown in Figure 4.5[5]. Both sequences correspond to the same experimental setup. While the crosses on the top gives the sequences of resonances with the magnetic field absent, the crosses on the bottom indicates the sequences of resonances when the magnet field is on. Clearly, the presence of the magnetic field grossly changes the location of the resonances.

[5]As a comparison to our experimental data, we have numerically solved the 2D quantum billiard eigenvalue problem with GOE statistics with the same physical parameters as the analogous microwave cavity without magnetized ferrite. As shown in the appendix (Sec. 5.4), the experimentally found eigenmodes corresponds almost exactly with the numerically solved eigenmodes in the low frequency range ($f \preceq 5\ GHz$).

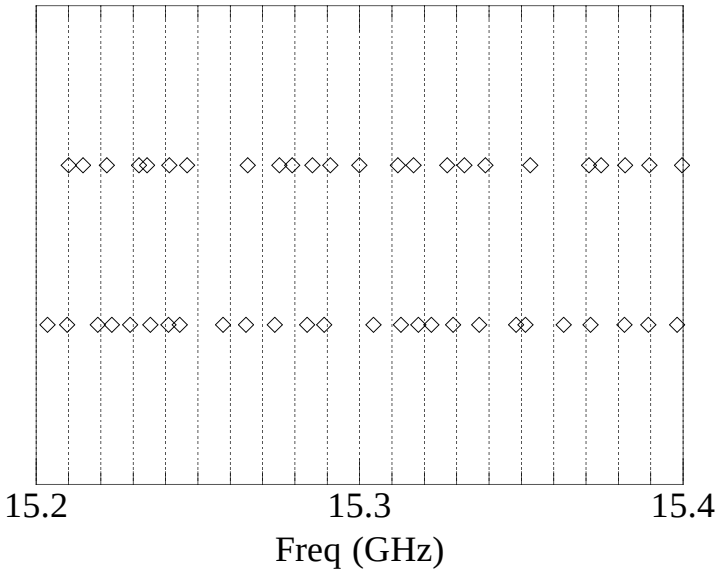

Figure 4.5: Sequences of cavity resonant frequencies from a section of our transmission spectra (a) with (diamonds on the bottom) and (b) without (diamonds on the top) the magnetic field applied to the ferrite strip.

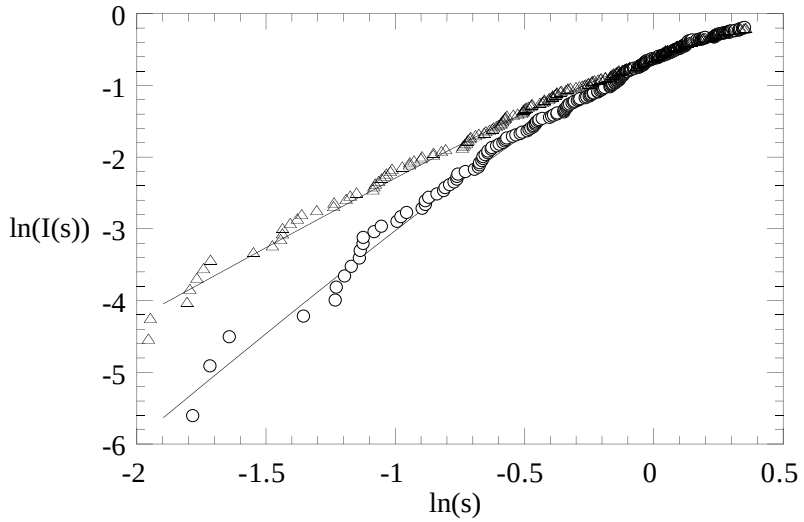

Figure 4.6: Experimental $\ln(I(s))$ vs. $\ln(s)$: circles and triangles correspond to data with and without magnetic filed respectively. Data are from the range: 13.43 - 15.69 GHz. Theoretical curves for the GOE (top solid curve) and the GUE (bottom solid curve) are superimposed.

Figure 4.6 shows experimental plots of $\ln(I(s))$ vs. $\ln(s)$ for the case with no magnetic field (triangles) and with magnetic field (circles) in the GUE regime (13.43-15.69 GHz). The theoretical predictions, the natural logarithm of the integral of Eqs. (4.10) and (4.11) are superposed on top. We note that the agreement between these experimental plots and the theoretical curves is quite good. Moreover, for small s values (Fig. 4.6), the best fitted straight lines to $\ln(I(s))$ give a slope of 2.02 for the time reversible case (GOE), as compared to the theoretical value of 2, and a slope of 2.88 for the time irreversible case (GUE), as compared to the theoretical value of 3.

Better statistical evidence for the GOE/GUE transition is provided by the $\Delta(L)$ plots in

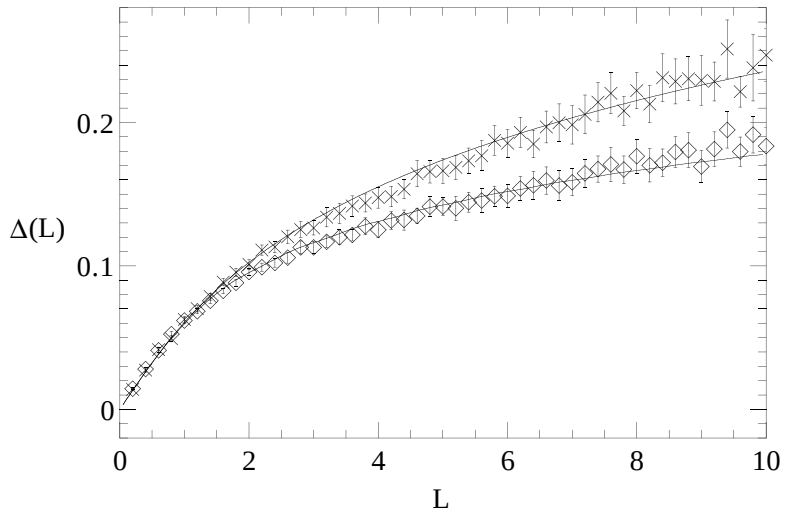

Figure 4.7: Experimental $\Delta(L)$ vs. L: diamonds and crosses correspond to data with and without magnetic filed respectively. Data are from the range: 13.43 - 15.69 GHz. Theoretical curves for the GOE (top solid curve) and the GUE (bottom solid curve) are superimposed. (These curves are from exact integral expressions for $\Delta(L)$, see Refs. [54] and [55])

Figure 4.7. Note that, since $\Delta(L)$ involves averaging over all the levels for each L, fluctuations are reduced, and a clear distinction between the two cases is evident. The lower solid curve of Figure 4.7 is the result of the random matrix GUE prediction for $\Delta(L)$ and the upper solid curve is the GOE prediction. The diamonds show data for the frequency range 13.43-15.69 GHz with the magnets in place. The crosses show data for the same frequency range with the magnets removed. The main qualitative effect of the time-reversal symmetry breaking (viz. a decrease in $\Delta(L)$) is clearly evident in the data; and the agreement between the data and the solid curves is good.

Figure 4.8 gives a sense of the transition from GOE to GUE. The three $\Delta(L)$ plots in Fig. (4.8) are calculated with the static magnetic field held fixed and with approximately the same number of energy levels ($\sim$260). The frequency range used for Fig. (4.8a) is 7-10.71 GHz. In this frequency range, we estimate from our calculations that $\Delta\phi(B, f)$ is not sufficiently large to alter the GOE statistics. For the frequency range for Fig. (4.8c) (13.43-15.69 GHz), we estimate that the difference $\Delta\phi(B, f)$ is sufficiently large to yield GUE statistics. The frequency range for Fig. (4.8b) (9.04-12.15 GHz) represents an intermediate case between GOE and GUE.

4.5 Conclusion

In conclusion, by placing a piece of magnetized ferrite inside a two-dimensional microwave cavity, we have successfully broken the time-reversal symmetry of the system and have shown that the resultant energy spectrum agrees with the one predicted by the Gaussian Unitary Ensemble of random matrices . Furthermore, by analyzing the data from different frequency ranges, we have experimentally observed the transition from GOE to GUE statistics.

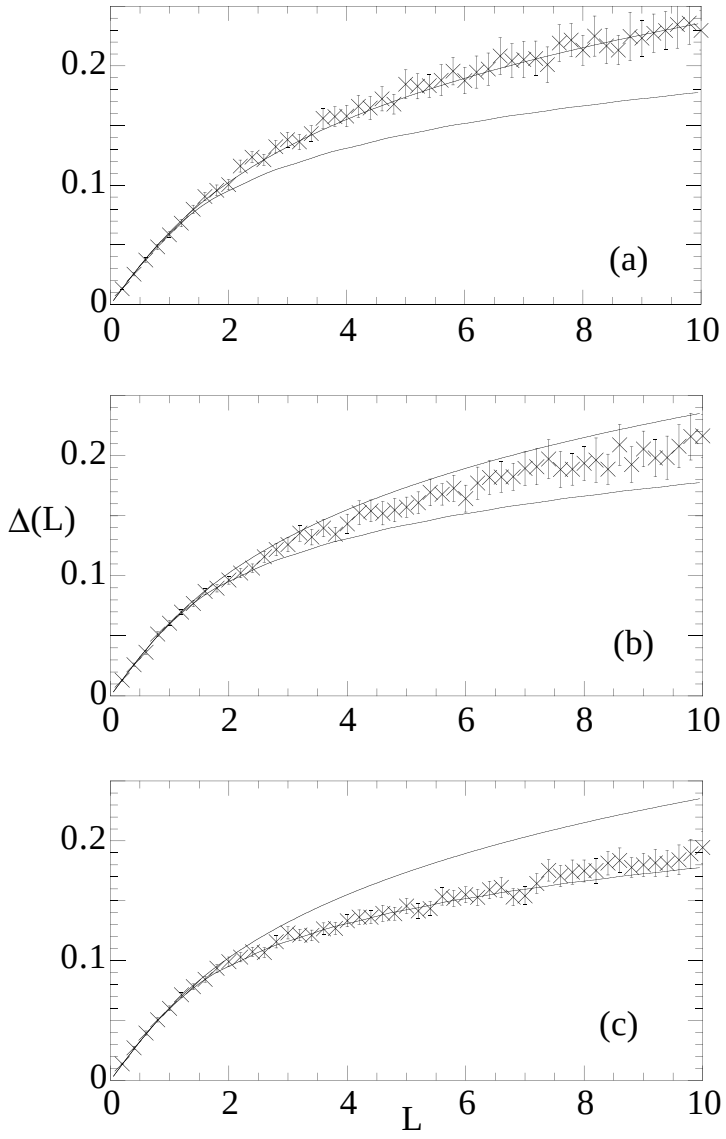

Figure 4.8: Experimental $\Delta(L)$ vs. L for three different frequency ranges with the static magnetic field held fixed. (a) 7 - 10.71 GHz, (b) 9.04 - 12.15 GHz, (c) 13.43 - 15.69 GHz. Theoretical curves for the GOE (top solid curve) and the GUE (bottom solid curve) are superimposed.

Chapter 5

Appendices

5.1 Appendix I to Chapter 2: Proof of Convergence of Observer's Error Matrix

In this section, we will show that by choosing the magnitudes of all the eigenvalues of the matrix $\mathbf{U}_n$ to be less than 1 (recall $\mathbf{U}_n$ is a lower triangular matrix), the product

$$\mathbf{J}_n = \prod_{i=1}^{n} \begin{bmatrix} \mathbf{U}_i & \mathbf{W}_i \\ \mathbf{0} & \mathbf{S}_i \end{bmatrix} = \begin{bmatrix} \prod_{i=1}^{n} \mathbf{U}_i & \mathbf{K}_n \\ \mathbf{0} & \prod_{i=1}^{n} \mathbf{S}_i \end{bmatrix}, \tag{5.1}$$

where

$$\mathbf{K}_n = \sum_{i=1}^{n} \left(\prod_{j=i+1}^{n} \mathbf{U}_j \right) \mathbf{W}_i \left(\prod_{k=1}^{i-1} \mathbf{S}_k \right), \tag{5.2}$$

will converge to zero with increasing n. To be specific, we will show that there exist positive constants $K < \infty$ and $0 < \mu < 1$ such that

$$\| \mathbf{J}_n \| \leq K\mu^n. \tag{5.3}$$

(Here, we have used the following matrix norm: $\| \mathbf{J} \| \equiv \sum_{i,j=1} |J_{ij}|$.)

First, we note that, since $\mathbf{S}_n$ is assumed to be stable, then by definition these exist constants $C_S < \infty$ and $0 < \mu_S < 1$, such that

$$\left\| \prod_{i=1}^{n} \mathbf{S}_i \right\| \leq C_S \mu_S^n. \tag{5.4}$$

In the following, we will show that there also exist positive constants $C_U < \infty, C^* < \infty, 0 < \mu_U < 1$, and $0 < \zeta < 1$, such that

$$\left|\left|\prod_{i=1}^{n} \mathbf{U}_i\right|\right| \leq C_U \mu_U^n \tag{5.5}$$

and

$$\| \mathbf{K}_n \leq C^* \zeta^n, \tag{5.6}$$

provided that we choose the magnitudes of all the eigenvalues of $\mathbf{U}_i$ to be less than 1. From the definition of the matrix norm, we have from Eq. (5.1),

$$\| \mathbf{J}_n \| = \left|\left|\prod_{i=1}^{n} \mathbf{U}_i\right|\right| + \| \mathbf{K}_n \| + \left|\left|\prod_{i=1}^{n} \mathbf{S}_i\right|\right|.$$

Now, utilizing Eqs. (5.4)-(5.6), we have

$$\| \mathbf{J}_n \leq K \mu^n, \tag{5.7}$$

where $K = 3\max\{C_U, C_S, C_*\}$ and $\mu = \max\{\mu_U, \mu_S, \zeta\}$, which is the desired result. In what follows, we derive Eqs. (5.5) and (5.6).

We derive Eq. (5.5) by using mathematical induction. First, we let Ω^{d_u} denote the set of all bounded d_u-dimensional lower triangular matrices whose eigenvalues all have magnitudes less than 1. For $d_u = 1$, the matrices in Eq. (5.5) are just scalars of magnitude less than 1. Thus, Eq. (5.5) is trivially satisfied. Now assume that for a set of matrices $\{\mathbf{Z}_i : \mathbf{Z}_i \in \Omega^{d_u}\}$ there exist $K_\beta < \infty$ and $0 < \beta < 1$ such that Eq. (5.5) is true,

$$\left|\left|\prod_{i=1}^{n} \mathbf{Z}_i\right|\right| \leq K_\beta \beta^n. \tag{5.8}$$

Then, we will use this assumption to show that there also exist $C < \infty$ and $0 < \mu < 1$ such that Eq. (5.5) is true for $\{\mathbf{U}_i : \mathbf{U}_i \in \Omega^{d_u+1}\}$. Let us consider a particular matrix $\mathbf{U}_i \in \Omega^{d_u+1}$. We partition it into the following form:

$$\mathbf{U}_i = \begin{bmatrix} \mathbf{Z}_i & \mathbf{0} \\ \mathbf{b}_i & \Lambda_i \end{bmatrix},$$

where $\mathbf{Z}_i \in \Omega^{d_u}$ and Λ_i is the $(d_u + 1)$th eigenvalue of $\mathbf{U}_i$. With this notation, the product of these $\mathbf{U}_i$ can be written as

$$\prod_{i=1}^{n} \mathbf{U}_i = \begin{bmatrix} \prod_{i=1}^{n} \mathbf{Z}_i & \mathbf{0} \\ \mathbf{L}_n & \prod_{i=1}^{n} \Lambda_i \end{bmatrix},$$

where

$$\mathbf{L}_n = \sum_{i=1}^{n} \left(\prod_{j=1}^{i-1} \Lambda_j \right) \mathbf{b}_i \left(\prod_{k=1}^{n-i} \mathbf{Z}_k \right).$$

Pick a value Λ_{max} satisfying $|\Lambda_i \leq \Lambda_{max} < 1$. Then,

$$\left|\left| \prod_{i=1}^{n} \Lambda_i \right|\right| \leq \Lambda_{max}^n. \tag{5.9}$$

Now consider the norm of $\mathbf{L}_n$:

$$\begin{aligned}
\parallel \mathbf{L}_n \parallel &= \left|\left| \sum_{i=1}^{n} \left(\prod_{j=1}^{i-1} \Lambda_j^{d_u+1} \right) \mathbf{b}_i \left(\prod_{k=1}^{n-i} \mathbf{Z}_k \right) \right|\right| \\
&\leq \sum_{i=1}^{n} \left|\left| \prod_{k=1}^{n-i} \mathbf{Z}_k \right|\right| \parallel \mathbf{b}_i \parallel (\Lambda_{max})^{i-1} \\
&\leq \sum_{i=1}^{n} \left|\left| \prod_{k=1}^{n-i} \mathbf{Z}_k \right|\right| \parallel \mathbf{b}_{max} \parallel (\Lambda_{max})^{i-1} \\
&\leq \sum_{i=1}^{n} K_\beta \beta^{n-i} \parallel \mathbf{b}_{max} \parallel (\Lambda_{max})^{i-1} \\
&\leq \sum_{i=1}^{n} K^{'} (\max\{\beta, \Lambda_{max}\})^{n-1} \\
&= nK^{'}(\mu^{'})^{n-1},
\end{aligned}$$

where $\parallel \mathbf{b}_{max} \parallel$ is the largest of the $\parallel \mathbf{b}_i \parallel, K^{'} = K_\beta \parallel \mathbf{b}_{max} \parallel$, and $\mu^{'} = \max\{\beta, \Lambda_{max}\}$. In order to put the above inequality in the right form, we pick a γ such that $\mu^{'} < \gamma < 1$. We then choose a constant K^* such that

$$nK^{'}(\mu^{'})^{n-1} \leq K^* \gamma^n,$$

for $n \geq 1$ where the constant K^* is any number bigger than the maximum over n of $nK^{'}(\mu^{'})^{n-1}\gamma^{n-1}$, (since $\gamma > \mu^{'}$, this maximum is finite). Thus,

$$\parallel \mathbf{L}_n \leq K^* \gamma^n. \tag{5.10}$$

With the bounds given by Eqs. (5.8)-(5.10), one can choose $C_U = 3\max\{K_\beta, K^*, 1\}$, and $\mu_U = \max\{\beta, \Lambda_{max}, \gamma\}$ so that

$$\left|\left| \prod_{i=1}^{n} \mathbf{U}_i \right|\right| \leq C_U \mu_U^n.$$

To complete our demonstration of Eq. (5.7), we now derive Eq. (5.6).

$$\begin{aligned} \| \mathbf{K}_n \| &= \left\| \sum_{i=1}^{n} \left(\prod_{j=i+1}^{n} \mathbf{U}_j \right) \mathbf{W}_i \left(\prod_{k=1}^{i-1} \mathbf{S}_k \right) \right\| \\ &\leq \sum_{i=1}^{n} \left\| \prod_{k=i+1}^{n} \mathbf{U}_k \right\| \| \mathbf{W}_i \| \left\| \prod_{k=1}^{i-1} \mathbf{S}_k \right\| \\ &\leq \sum_{i=1}^{n} C_U \mu_U^{n-i} \| \mathbf{W}_{max} \| C_S \mu_S^{i-1} \\ &\leq \sum_{i=1}^{n} C^{'} \eta^{n-1} \\ &= n C^{'} \eta^{n-1}, \end{aligned}$$

where $\| \mathbf{W}_{max} \|$ is the largest of the $\| \mathbf{W}_i \|, C^{'} = \| \mathbf{W}_{max} \| \max\{C_U, C_S\}$, and $eta = \max\{\mu_U, \mu_S\} < 1$. Choose $\eta < \zeta < 1$ and C^* such that

$$n C^{'} \eta^{n-1} \leq C^* \zeta^n,$$

for $n \geq 1$, we then yield Eq. (5.6).

5.2 Appendix II to Chapter 2: Generalization of the Full-Order Observer to Systems with Arbitrary Number of Unstable Directions and with Vectoral Output Function

Consider a d-dimensional system,

$$\mathbf{X}_{n+1} = \mathbf{M}(\mathbf{X}_n), \mathbf{O}_n = \mathbf{g}(\mathbf{X}_n), \tag{5.11}$$

where the observed output $\mathbf{O}_n$ is a d_o-dimensional vector. Let us say that the unstable subspace of this dynamical system is d_u dimensional. Then, the full-order nonlinear observer can be defined as

$$\hat{\mathbf{X}}_{n+1} = \mathbf{M}(\hat{\mathbf{X}}_n) + \mathbf{C}_n[\mathbf{O}_{n+1} - \hat{\mathbf{O}}_{n+1}]. \tag{5.12}$$

Here, $\mathbf{C}_n$ is a $d \times d_o$ time-dependent control matrix. The error equation corresponding to this observer and the true system is given by

$$\delta \mathbf{X}_{n+1} = \left[\mathbf{DM}(\hat{\mathbf{X}}_n) - \mathbf{C}_n \mathbf{Dg}(\mathbf{M}(\hat{\mathbf{X}}_n)) \mathbf{DM}(\hat{\mathbf{X}}_n) \right] \delta \mathbf{X}_n, \tag{5.13}$$

where $\delta \mathbf{X}_n = \mathbf{X}_n - \hat{\mathbf{X}}_n$ is a differential, and $\mathbf{DM}(\hat{\mathbf{X}}_n)$ and $\mathbf{Dg}(\mathbf{M}(\hat{\mathbf{X}}_n))$ are the derivatives of $\mathbf{M}(\hat{\mathbf{X}}_n)$ and $\mathbf{g}(\mathbf{M}(\hat{\mathbf{X}}_n))$, respectively, with $\mathbf{DM}$ a $d \times d$ matrix and $\mathbf{Dg}$ a $d_o \times d$ matrix. Now, we will restrict the action of $\mathbf{C}_n$ to the unstable subspace by the following construction:

$$\begin{aligned} \mathbf{C}_n &= \sum_{i=1}^{d_u} \boldsymbol{\beta}_n^{(i)} \\ \text{with } \boldsymbol{\beta}_n^{(i)} &= C_1^{(i)} \mathbf{e}_{n+1}^{(i)} \mathbf{V}_1 + \cdots + C_{d_o}^{(i)} \mathbf{e}_{n+1}^{(i)} \mathbf{V}_{d_o}, \end{aligned} \tag{5.14}$$

where $\{\mathbf{e}_n^{(i)}\}$ [defined in Eq. (5.15)] is a set of column vectors which spans the unstable subspace at $\hat{\mathbf{X}}_n$ and $\{\mathbf{V}_i\}$ can be any complete set of row vectors which spans $\Re^{d_o}$. In this case, $\left[\mathbf{DM}(\hat{\mathbf{X}}_n) - \mathbf{C}_n \mathbf{Dg}(\mathbf{M}(\hat{\mathbf{X}}_n)) \mathbf{DM}(\hat{\mathbf{X}}_n) \right]$ can again be put in a block form:

$$\begin{bmatrix} \mathbf{U}_n & \mathbf{W}_n \\ \mathbf{0} & \mathbf{S}_n \end{bmatrix},$$

with $\mathbf{U}_n$ as a $d_u \times d_u$ submatrix acting on the unstable subspace, $\mathbf{S}_n$ as a $(d - d_u) \times (d - d_u)$ submatrix acting on the stable subspace, and $\mathbf{W}_n$ as a $d_u \times (d - d_u)$ submatrix taking vectors from the stable subspace into the unstable subspace. Then, we define d_u numbers: $\lambda_n^{(1)}, \cdots, \lambda_n^{(d_u)}$, and d_u basis column vector: $\mathbf{e}_n^{(1)}, \cdots, \mathbf{e}_n^{(d_u)}$, for the unstable subspace at $\hat{\mathbf{X}}_n$ according to the following procedure:

$$\begin{aligned} \lambda_n^{(1)} \mathbf{e}_{n+1}^{(1)} &= [\mathbf{DM}(\hat{\mathbf{X}}_n)] \mathbf{e}_n^{(1)}, \\ \lambda_n^{(2)} \mathbf{e}_{n+1}^{(2)} &= \left[\mathbf{DM}(\hat{\mathbf{X}}_n) - \boldsymbol{\beta}_n^{(1)} \mathbf{Dg}(\mathbf{M}(\hat{\mathbf{X}}_n)) \mathbf{DM}(\hat{\mathbf{X}}_n) \right] \mathbf{e}_n^{(2)}, \\ &\vdots \\ \lambda_n^{(d_u)} \mathbf{e}_{n+1}^{(d_u)} &= \left[\mathbf{DM}(\hat{\mathbf{X}}_n) - \sum_{i=1}^{d_u - 1} \boldsymbol{\beta}_n^{(i)} \mathbf{Dg}(\mathbf{M}(\hat{\mathbf{X}}_n)) \mathbf{DM}(\hat{\mathbf{X}}_n) \right] \mathbf{e}_n^{(d_u)}. \end{aligned} \tag{5.15}$$

In this set of basis, $\mathbf{U}_n$ will be in lower triangular form with $d_u \times d_o$ free parameters, $C_j^{(i)}, 1 \leq i \leq d_u, 1 \leq j \leq d_o$ [see Eq. (5.14)]:

$$\mathbf{U}_n = \begin{bmatrix} \lambda_n^{(1)} - \mathbf{f}_{n+1}^{(1)} \boldsymbol{\beta}_n^{(1)} \mathbf{D}h_n^{(1)} & 0 & \cdots & 0 \\ -\mathbf{f}_{n+1}^{(2)} \boldsymbol{\beta}_n^{(2)} \mathbf{D}h_n^{(1)} & \lambda_n^{(2)} - \mathbf{f}_{n+1}^{(2)} \boldsymbol{\beta}_n^{(2)} \mathbf{D}h_n^{(2)} & \cdots & 0 \\ \vdots & \vdots & \vdots & \vdots \\ -\mathbf{f}_{n+1}^{(d_u)} \boldsymbol{\beta}_n^{(d_u)} \mathbf{D}h_n^{(1)} & -\mathbf{f}_{n+1}^{(d_u)} \boldsymbol{\beta}_n^{(d_u)} \mathbf{D}h_n^{(2)} & \cdots & \lambda_n^{(d_u)} - \mathbf{f}_{n+1}^{(d_u)} \boldsymbol{\beta}_n^{(d_u)} \mathbf{D}h_n^{(d_u)} \end{bmatrix}.$$

where $\mathbf{D}h_n^{(d_u)} = \mathbf{Dg}(\mathbf{M}(\hat{\mathbf{X}}_n))\mathbf{DM}(\hat{\mathbf{X}}_n)\mathbf{e}_n^{(d_u)}$ is a d_o-dimensional column vector and $\{\mathbf{f}_{n+1}^{(i)}\}$ is the corresponding set of dual vectors for $\{\mathbf{e}_{n+1}^{(i)}\}$. We can adjust these $d_u \times d_o$ free parameters $C_j^{(i)}$ such that the eigenvalues of $\mathbf{U}_n, \Lambda_n^{(i)} = \lambda_n^{(i)} - \mathbf{f}_{n+1}^{(i)} \boldsymbol{\beta}_n^{(i)} \mathbf{D}h^{(i)}$ will all be less than 1. Since $\mathbf{U}_n$ is d_u-dimensional, by setting all its eigenvalues to be less than 1 will only provide d_u conditions. In other words, we will have $d_u \times (d_o - 1)$ parameters left for our disposal. This is an advantage that is not possible in the case when the observed output is a scalar (i.e., $d_o = 1$). In the simplest case, when we set all eigenvalues of $\mathbf{U}_n$ and the rest of the $d_u \times (d_o - 1)$ parameters (i.e., $C_j^{(i)} = 0, \forall j > 1$) to be zero, the control matrix $\mathbf{U}_n$ is given by the following equation:

$$\mathbf{C}_n = \sum_{i=1}^{d_u} \frac{\lambda_n^{(i)}}{\mathbf{V}_1 \mathbf{D}h_n^{(i)}} \mathbf{e}_{n+1}^{(i)} \mathbf{V}_1. \tag{5.16}$$

5.3 Appendix to Chapter 3: Empirical Proportional Feedback

An alternative route to stabilizing unstable periodic orbits is via empirical proportional feedback (see Ref.[27, 28]). In this method, one attempts to achieve stabilization by an ad hoc feedback perturbation which is proportional to the difference between the state of the system and its desired periodic state (the parameter of the system is assumed to be fixed at its nominal value), i.e.,

$$\mathbf{Z}_{n+1} = \mathbf{G}(\mathbf{Z}_n, \bar{p}) - \mathbf{K}(\mathbf{Z}_n - \mathbf{Z}_n^*), \tag{5.17}$$

where $\mathbf{K}$ is an adjustable gain matrix and $\mathbf{Z}_n^* = \mathbf{Z}_{n+T}^*$ is the desired periodic orbit. The stability of the periodic point $\mathbf{Z}_n^*$ depends on the spectrum of eigenvalues of the following

stability matrix[1],

$$\mathbf{L}(\mathbf{K}) = [\mathbf{A}_{n-1} - \mathbf{K}][\mathbf{A}_{n-2} - \mathbf{K}] \cdots [\mathbf{A}_{n-T} - \mathbf{K}], \tag{5.18}$$

where $\mathbf{A}_n$ is the Jacobian of $\mathbf{G}(\mathbf{Z})$ (see Eq. (3.3)) evaluated at $\mathbf{Z}_n^*$ with p fixed at $\bar{p}$. The periodic orbit can be stabilized if the magnitude of the largest eigenvalue $\lambda_{max}(\mathbf{K})$ of $\mathbf{L}(\mathbf{K})$ is less than one. In most experimental cases, $\mathbf{K}$ is simply a scalar factor K multiplied by a projection operator $\mathbf{P}$. To illustrate this proportional feedback control scheme, we will again use the Ikeda map Eq. (3.19) and the output scalar function $\xi_n = u_n$ to generate our time delay vector $\mathbf{Z}_n$. In Fig. (5.1a,b), the projection operators which we have chosen for $\mathbf{K}$ are: (a) $\mathbf{P}_a = \begin{pmatrix} 1 & 0 \\ 0 & 0 \end{pmatrix}$, (b) $\mathbf{P}_b = \begin{pmatrix} 0 & 0 \\ 0 & 1 \end{pmatrix}$ and the periodic orbit being considered is $\mathbf{X}_{p3}^*$. In this graph, the logarithm of $|\lambda_{max}(K)|$ is plotted as a function of the scalar factor K.. The periodic orbit $\mathbf{X}_{p3}^*$ can be stabilized by the proportional feedback scheme depending on the values of K. In particular, the proportional feedback scheme works for the values of K such that $|\lambda_{max}(K)| < 1$. In our first example, Fig. (5.1a), there exist two small ranges of values of K such that the condition $|\lambda_{max}(K)| < 1$ (or equivalently, $\ln|\lambda_{max}(K)| \leq 0$) is satisfied, while in our second example, Fig. (5.1b), the condition is never satisfied in the range of values of K considered.

5.4 Appendix to Chapter 4: Numerical Method used in Solving the Quantum Billiard Eigenvalue Problem with GOE Statistics and Comparison with Experiment

In the absence of the magnetic field $\mathbf{B}_f$, Eq. (4.3) reduces to the Helmholtz equation,

$$(\nabla^2 + k^2)\psi = 0, \qquad k^2 = 2mE/\hbar^2, \tag{5.19}$$

[1]Since the periodic orbit $\mathbf{Z}_n^*$ is of period T, i.e., $\mathbf{A}_n = \mathbf{A}_{n+T}$, there will be a total of T different L_j's. However, since the determinant of a product of matrices is the product of the determinant of the same matrices, the spectrum of eigenvalues for all $\mathbf{L}_j$ with $1 \leq j \leq T$ are the same.

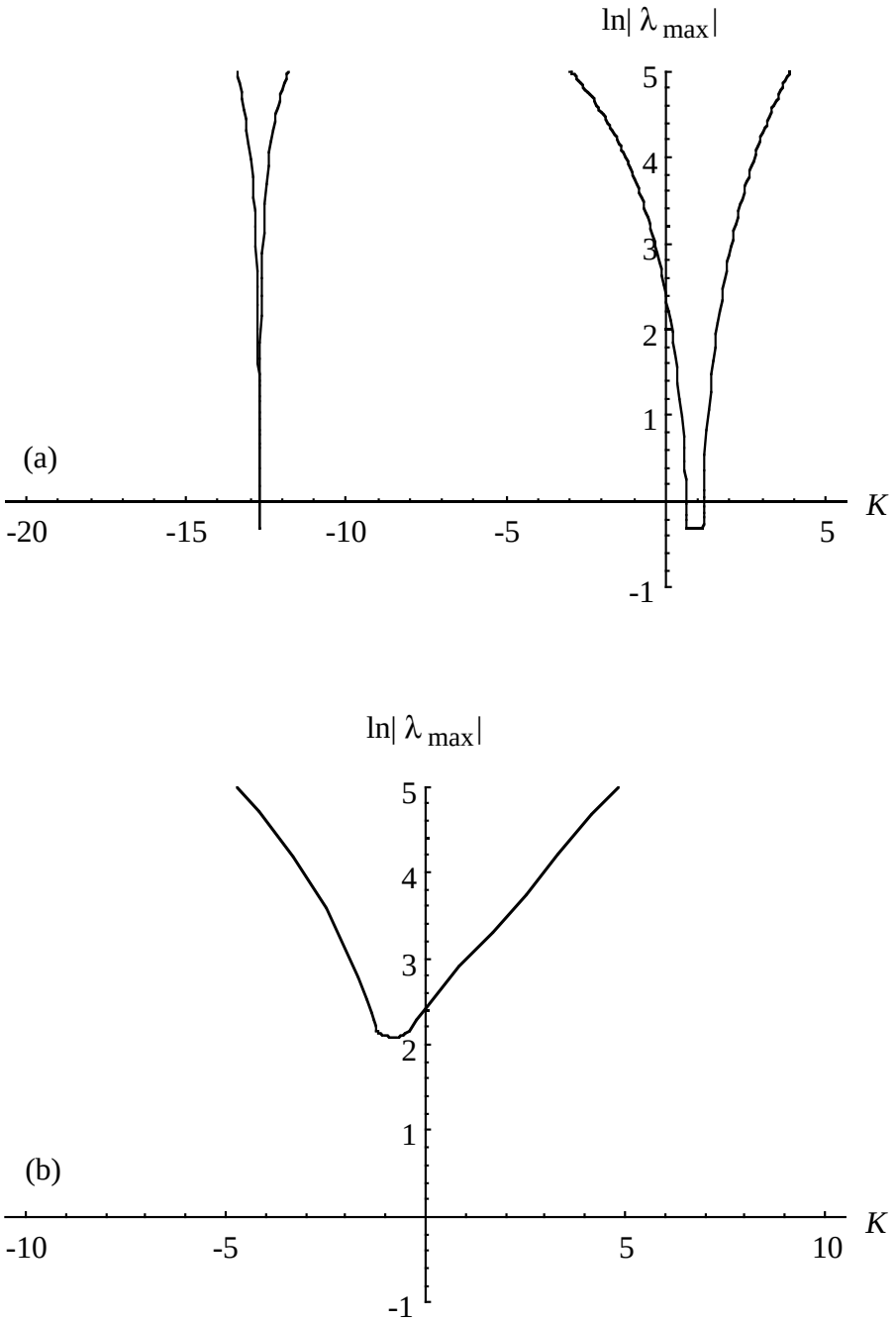

Figure 5.1: Ikeda map: $\ln|\lambda_{max}(K)|$ vs. K. (a) $\mathbf{K} = K\mathbf{P}_a$, (b) $\mathbf{K} = K\mathbf{P}_b$. The periodic orbit being considered is $\mathbf{X}^*_{p3}$ and it can be stabilized by the proportional feedback scheme for the values of K such that $\ln|\lambda_{max}(K)| \leq 0$.

with $\psi = 0$ on the boundary. We solved for the eigenvalues k_n's of this boundary value problem by applying the boundary element method[56]. This numerical method starts with the general integral representation of the wavefunction ψ using an appropriate Green function,

$$\psi(\mathbf{x}) = \int_{\partial} (\psi(\mathbf{x}')\nabla_{\hat{\mathbf{n}}(\mathbf{x}')} G(\mathbf{x}, \mathbf{x}'; k) - G(\mathbf{x}, \mathbf{x}'; k)\nabla_{\hat{\mathbf{n}}(\mathbf{x}')}\psi(\mathbf{x}'))\mathbf{dx}', \tag{5.20}$$

where $\int_{\partial}$ is integrated over the boundary of the domain and $\nabla_{\hat{\mathbf{n}}(\mathbf{x}')}$ is the normal derivative evaluated at the boundary point $\mathbf{x}'$. This integral equation can be solved directly by discretizing Eq. (5.20) along the boundary ∂. Then, by imposing the boundary condition, $\psi(\mathbf{x}_i) = 0, \forall \mathbf{x}_i \in \partial$, one arrives at the following matrix equation for all $\mathbf{x}_i$ on the boundary,

$$\sum_{j=1}^{N} \mathbf{G}_{ij}(k)\mathbf{v}_j = 0, \qquad \forall \mathbf{x}_i \in \partial, \tag{5.21}$$

where N is the resolution of discretization over the boundary and j is summed over all discretized points $\mathbf{x}_j \in \partial$. In this discretization, $\mathbf{G}_{ij}(k) = G(\mathbf{x}_i, \mathbf{x}_j; k)$ are the values of the free space Green function evaluated on the boundary points, $\mathbf{x}_i$ and $\mathbf{x}_j$, while $\mathbf{v}_j = \nabla_{\hat{\mathbf{n}}(\mathbf{x_j})}\psi(\mathbf{x}_j)$ are the yet to be determined values of the normal derivative of ψ at the boundary point $\mathbf{x}_j$. Eq. (5.21) has a nontrivial solution if the determinant of $\mathbf{G}_{ij}(k)$ equals to zero[2]. Thus, the numerical method in solving for the eigenvalues of Eq. (5.19) reduces simply to searching for values of k which gives $\det(\mathbf{G}_{ij}(k)) = 0$.

The above procedure is generally called the "direct" method. From our numerical trials, we found that an alternative "indirect" method is able to produce more accurate results due to its different method in handling the singularity in the Green function. As one can see from Eq. (5.20), the integrand involves both the Green function and its normal derivative. It can be shown that in the coincidence limit $\mathbf{x}' \to \mathbf{x}$, the normal derivative of the Green function is better behaved than the Green function itself. As shown in Eq. (5.21), the "direct" method with $\psi = 0$ on the boundary involves only the value of the Green function. The goal of the "indirect" method is to utilize the normal derivative of the Green function in the calculation instead. One can accomplish this by introducing an auxiliary exterior solution $\tilde{\psi}$ which is by definition equaled to zero inside the domain boundary. By construction, $\tilde{\psi}$ satisfies the same

[2]After the eigenvalues k_n are found, one can solve for the unknown vector $\mathbf{v}_i$ from the matrix equation Eq. (5.21) and the eigenfunctions ψ_n can then be evaluated using the set of $\mathbf{v}_i$ and the discretized version of Eq. (5.20), $\psi_n(\mathbf{x}) = \sum_{j=1}^{N} \mathbf{G}(\mathbf{x}, \mathbf{x}_j; k_n)\mathbf{v}_j$.

Eq. (5.19) as ψ and by subtracting the equations for $\tilde{\psi}$ from those for ψ, we have

$$\int_{\partial} \{D(\mathbf{x}')[\nabla_{\hat{\mathbf{n}}(\mathbf{x}')} G(\mathbf{x}, \mathbf{x}'; k) - 1] - P(\mathbf{x}') G(\mathbf{x}, \mathbf{x}'; k)\} \mathbf{dx}' = 0, \tag{5.22}$$

where $D(\mathbf{x}') = \psi(\mathbf{x}') - \tilde{\psi}(\mathbf{x}')$ and $P(\mathbf{x}') = \nabla_{\hat{\mathbf{n}}(\mathbf{x}')} \psi(\mathbf{x}') - \nabla_{\hat{\mathbf{n}}(\mathbf{x}')} \tilde{\psi}(\mathbf{x}')$[3]. Now, we can set the second term to zero by imposing the following boundary condition on the auxiliary exterior solution $\tilde{\psi}$:

$$P(\mathbf{x}) = \nabla_{\hat{\mathbf{n}}(\mathbf{x})} \psi(\mathbf{x}) - \nabla_{\hat{\mathbf{n}}(\mathbf{x})} \tilde{\psi}(\mathbf{x}) = 0, \qquad \forall \mathbf{x} \in \partial, \tag{5.23}$$

Together with the original boundary condition on ψ, we again arrive at a matrix equation involving the normal derivative of the Green function only,

$$\sum_{j=1}^{N} \mathbf{H}_{ij}(k) \mathbf{w}_j = 0, \qquad \forall \mathbf{x}_i \in \partial, \tag{5.24}$$

where $\mathbf{H}_{ij}(k) = \nabla_{\hat{\mathbf{n}}(\mathbf{x}_j)} G(\mathbf{x}_i, \mathbf{x}_j; k)$ are the values of the normal derivative of the Green function evaluated on the boundary points, $\mathbf{x}_i$ and $\mathbf{x}_j$, and $\mathbf{w}_j = \psi(\mathbf{x}_j) - \tilde{\psi}(\mathbf{x}_j)$ are the yet to be determined values of the discontinuities between the interior solution ψ and the exterior solution $\tilde{\psi}$ on the boundary.

With the two dimensional domain given by the inset of Fig. (4.3), the set of eigenvalues $E_n = \frac{(k_n \hbar)^2}{2m}$ of Eq. (5.19) should follows the GOE statistics. Figure 5.2 shows the locations of both the eigenvalues of Eq. (5.19) found using the above numerical technique and the eigenmodes found experimentally from the microwave cavity without ferrite. One can see that their agreement is good for low frequencies ($\sim$ 3 GHz) and deviations between the numerical and experiment spectra begin to grow as one moves to higher frequency range (¿ 5 GHz). We believe that these deviations are due to the small discrepancies between the parameters in the computer model and the actual experimental cavity.

The numerical data were also used to examine the sensitivity of the spectral statistical measure $\Delta(L)$ with respective to the accuracy and completeness of the eigenvalue spectrum. We performed three different types of perturbations on the section (7 - 15 GHz) of the numerically calculated spectra corresponding to the same section obtained from microwave cavity measurements. In the first case, we first calculate the spacings $S_i = E_{i+1} - E_i$ between all the

[3]Inside the two dimensional domain, because $\tilde{\psi}$ is identically zero, Eq. (5.22) reduces to $\int_{\partial} (D(\mathbf{x}') \nabla_{\hat{\mathbf{n}}(\mathbf{x}')} G(\mathbf{x}, \mathbf{x}'; k) - P(\mathbf{x}') G(\mathbf{x}, \mathbf{x}'; k)) \mathbf{dx}' = \psi(\mathbf{x})$.

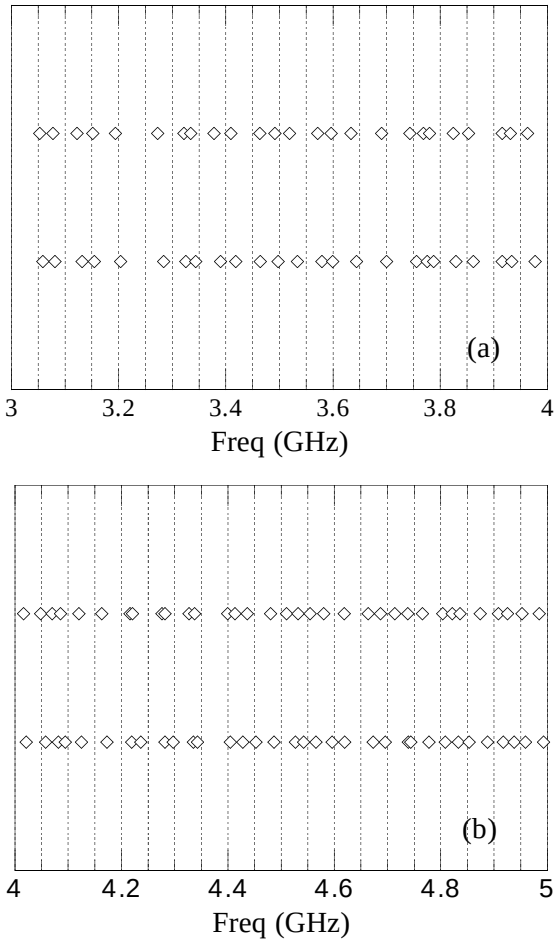

Figure 5.2: Locations of eigenvalues calculated by solving Eq. (5.19) numerically (top diamonds) and eigenmodes found experimentally from the microwave cavity without magnetized ferrite (bottom diamonds): (a) 3 - 4 GHz; (b) 4 - 5 GHz. The two analogous systems have the same physical parameters (see Fig. (4.3)).

eigenvalues and we identify 5% of the smallest spacings. Then, we delete this set of spacings by taking out both eigenvalues on either sides of S_i, namely, E_{i+1} and E_i. We then substitute the average value, $(E_{i+1} + E_i)/2$, back into the spectrum. In the second case, we use the deleted sequence from the former case and randomly add 5% new eigenvalues to the spectrum. In the last case, we again start out with the unperturbed sequence and we randomly move the eigenvalues forward or backward along the spectrum with a maximum magnitude given by 50% of the distance to its closest neighbor. (In this way, the ordering of the eigenvalues will be preserved.) Figure 5.3 compares the spectral rigidities calculated from the three perturbed spectra with the one calculated from the unperturbed one. As expected, the deletion of smallest spacings lowers the spectral rigidity from its unperturbed value and the added randomness in both case 2 and 3 moves the spectral rigidity higher. However, most importantly, the shifts in the spectral rigidities from the three different perturbed spectra are all smaller than the theoretical difference between the GOE and the GUE case. We conclude that even rather large errors on the order of magnitude used in these tests, if present in our experimental data, would not spoil our conclusions.

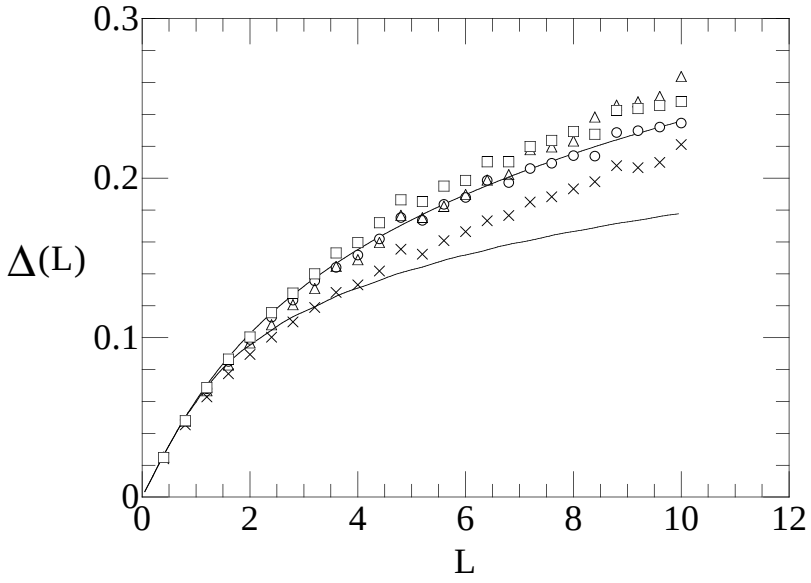

Figure 5.3: Spectral Rigidity $\Delta(L)$ vs. L for the three different perturbed spectra and the unperturbed spectrum. Crosses corresponds to case 1, triangles corresponds to case 2, squares corresponds to case 3, circles corresponds to the unperturbed case. Theoretical curves for the GOE (top solid curve) and the GUE (bottom solid curve) are superimposed.

Bibliography

[1] *Coping With Chaos*, edited by E. Ott, T. Sauer, J. A. Yorke (John Wiley and Sons, Inc, New York, 1994).

paper

[2] F. Takens, in *Dynamical Systems and Turbulence*, edited by D. Rand and L. S. Young (Springer-Verlag, Berlin, 1981), p.230.

[3] D. D. Anderson and J. B. Moore, *Optimal Filtering*, (Prentice-Hall, Englewood Cliffs, NJ 1990), pp. 193-211.

[4] K. Ogata, in *Modern Control Engineering* (Prentice-Hall, Englewood Cliffs, NJ, 1990), pp. 677-886.

[5] F. J. Romeiras, C. Grebogi, E. Ott, and W. P. Dayawansa, Physica D **58,** 165 (1992).

[6] C. Grebogi, E. Kostelich, E. Ott, and J. A. Yorke, Phys. Lett. A, **118**, 448 (1986); **120**, 497(E) (1987).

[7] L. Pecora and T. Carroll, Phys. Rev. Lett. **64**, 821 (1990).

[8] J. D. Farmer, E. Ott, and J. A. Yorke, Physica D **7**, p. 153 (1983).

[9] F. J. Romeiras, E. Ott, C. Grebogi, and W. P. Dayawansa, in *Proceedings of the American Control Conference* (IEEE, Piscataway, NJ, 1991), pp. 1113-1119; and Romeiras *et al.* [5].

[10] D. D. Anderson and J. B. Moore, *Optimal Filtering*, (Ref. [3]), pp.39-45.

[11] E. Ott, C. Grebogi and J. A. Yorke, Phys. Rev. Lett. **64,** 1196 (1990).

[12] U. Dressler and G. Nitsche, Phys. Rev. Lett. **68,** 1 (1992).

[13] J.-P. Eckmann and D. Ruelle, Rev. Mod. Phys. **57,** 617 (1985).

[14] E. J. Kostelich and J. A. Yorke, Phys. Rev. A **38,** 1649 (1988).

[15] E. J. Kostelich and J. A. Yorke, Physica D **41,** 183 (1990).

[16] D. P. Lathrop and E. J. Kostelich, Phys. Rev. A **40,** 4028-4031 (1989).

[17] E. Kostelich, Physica D **58,** 138 (1992).

[18] D. Auerbach, P. Cvitanovič, J.-P. Eckmann, and G. Gunaratne, Phys. Rev. Lett. **58,** 2387 (1987).

[19] T. Shinbrot, E. Ott, C. Grebogi, and J. A. Yorke, Phys. Rev. Lett. **65,** 3215-3218 (1990); Phys. Rev. A **45,** 4165-4168 (1992); Phys. Rev. Lett. **68,** 2863-2866 (1992); Phys. Lett. A **169,** 349-354 (1992).

[20] E. Kostelich, C. Grebogi, E. Ott, and J. A. Yorke, Phys. Rev. E **47,** 305-310 (1993).

[21] E. Bradley, in *Lecture Notes Control and Information Sciences,* No. 165 (ed. G. Jacob and F. Lamnabhi-Lagarrigue) (Springer, Berlin, 1991) pp. 307-325.

[22] E. Barreto, E. Kostelich, E. Ott, C. Grebogi, and J. A. Yorke (to be published).

[23] S. Hammel, C. K. Jones and J. Maloney, J. Opt. Soc. Am. B, **2,** 552 (1985).

[24] The periodic points are found numerically using the program *Dynamics: Numerical Explorations* written by H. E. Nusse, J. A. Yorke and E. Kostelich, (1992).

[25] D. Auerbach, C. Grebogi, E. Ott, and J. A. Yorke, Phys. Rev. Lett. **69,** 3479 (1992).

[26] E. Barreto, *et al.* (to be published).

[27] K. Pyragas, Phys. Lett. A **170,** 421 (1992).

[28] K. Pyragas, Phys. Lett. A **181,** 203 (1993).

[29] W. Ditto, S.N. Rauseo, and M.L. Spano, Phys. Rev. Lett., **65**, 3211 (1990).

[30] J. Singer, Y.-Z. Wang, and H.H. Bau, Phys. Rev. Lett., **66**, 1123 (1991).

[31] A. Garfinkel, M. Spano, W. Ditto, and J. Weiss, Science, **257**, 1230 (1992).

[32] E.R. Hunt, Phys. Rev. Lett., **67**, 1953 (1991).

[33] Z. Gills, C.Iwata, R. Roy, I. Schwartz, and I. Triandaf, Phys. Rev. Lett., **69**, 3169 (1992).

[34] C. Reyl, L. Flepp, R. Badii, and E. Brun, Phys. Rev. E. **47**, 267 (1993).

[35] V. Petrov, V. Gáspár, J. Masere, and K. Showalter, Nature, **361**, 240 (1993).

[36] S. Schiff, K. Jerger, D.G. Duong, T. Chang, M.L. Spano, and W. Ditto, Nature, **370**, 615 (1994).

[37] O. Bohigas, M. -J. Giannoni, *Mathematical and Computational Methods in Nuclear Physics*, Lecture Notes in Physics, **209**, ed. J. S. Edhesa, J. M. G. Gomez and A. Polls (Springer-Verlag, Berlin, 1984).

[38] F. Haake, *Quantum Signatures of Chaos*, (Springer-Verlag, Berlin, 1991).

[39] H. -J. Stockmann and J. Stein, *Phys. Rev. Lett.* **64**, 2215 (1990).

[40] S. Sridhar, *Phys. Rev. Lett.* **67**, 785 (1991).

[41] H. -D. Graf *et al.*, *Phys. Rev. Lett.* **69**, 1296 (1992).

[42] J. Main *et al.*, *Phys. Rev. Lett.* **57**, 2789 (1986).

[43] P. So, S. M. Anlage, E. Ott, and R. Oerter, *Phys. Rev. Lett.* **74**, ??? (1995).

[44] A. Kudrolli, S. Sridhar, A. Pandey, and R. Ramaswamy, *Phys. Rev. E* **49**, R11-R14 (1994).

[45] M. Sieber, *J. Phys. A.* **26**, 6217 (1993).

[46] O. Bohigas *et al.*, (unpublished).

[47] A. Pandey and M. L. Mehta, *Comm. Math. Phys.* **87**, 499 (1983).

[48] G. Lenz and K. Haake, *Phys. Rev. Lett.* **67**, 1 (1991).

[49] M. L. Mehta and A. Pandey, *J. Phys.* **16 A**, 2655 and L601 (1983).

[50] M. V. Berry and M. Robnik, *J. Phys.* **19 A**, 649 (1986).

[51] Trans-Tech, Inc., Adamstown, Maryland.

[52] H. P. Baltes and E. R. Hilf, *Spectra of Finite Systems* (Wissenschaftsverlag, Mannheim, 1976).

[53] R. B. Balian and C. Bloch, *Ann. Phys.* **60**, 401 (1970) and *ibid.* **63**, 592 (1971).

[54] F. Dyson and M. Mehta, *J. Math. Phys.* **4** 701-712 (1963).

[55] M. Mehta, *Random Matrices* (Academic Press, New York, 1990), 2nd ed.

[56] C. A. Brebbia, *The Boundary Element Method for Engineers*, New York (1978).